ACTIVATED REACTIVE EVAPORATION OF HYDROGENATED AMORPHOUS SILICON

by

Sukanta Biswas

A Thesis submitted in partial fulfilment of the requirements for the degree of Doctor of Philosophy of the University of London, and the Diploma of Imperial College

Department of Electrical Engineering
Imperial College of Science and Technology
(University of London)

July 1985

To Didima

ABSTRACT

In activated reactive evaporation (ARE) thermionically emitted electrons from an electron-beam melted pool in a silicon ingot are collected by an electrode, positioned above the pool, carrying a positive potential of a few hundred volts. These electrons ionise hydrogen admitted to the vacuum chamber and a plasma is created in which a gas-phase reaction between silicon and hydrogen can occur. In this way amorphous silicon-hydrogen alloy films are deposited. It is found that the quality of the deposited film is improved by applying an r.f. bias of ~-2000 volts to the substrate during deposition. The above technique has been optimised by synthesising plasma conditions similar to those present in the conventional glow discharge (G.D.) decomposition of silane. The new method allows hydrogenated amorphous silicon to be deposited at high rates (up to 0.5 μm/min has been achieved compared with 1 μm/hr for the G.D. process). Intrinsic films with electrical and optical properties closely similar to those produced by G.D. deposition have been obtained.

The films have been doped by mixing B_2H_6, for p-type, and PH_3, for n-type with the hydrogen gas stream. Doping has been achieved over the whole range, from p^+ to n^+.

By replacing the silicon ingot with a silicon/ antimony alloy, n-doped films have been produced. Silicon/ boron ingots can be used similarly to prepare p-type films. This method would eliminate the use of toxic gasses.

Conductivity, photoconductivity, infrared and optical absorption measurements, scanning electron microscopy and secondary ion mass spectrometry (SIMS) have been used to characterise the film properties.

Electrical and optical properties have been correlated with the hydrogen concentration in the films. The results are discussed and compared with those for materials prepared by standard G.D. and sputtering of silicon in hydrogen/argon mixture deposition methods and the advantages of this new process are given.

ACKNOWLEDGEMENTS

I am deeply indebted to Professor J.C. Anderson for his keen interest, guidance and most valuable advice throughout this work; and for providing me with the opportunity to undertake this project.

I would like to thank Mr. R. Chater for providing the SIMS facilities; Dr. J Drazin for writing the initial software for the data collection using the microcomputer; Mr. K White for all his help in the Workshop; Mr Z. Hussain for introducing me to the optical spectrometer and Dr A Kwabwe for helping me with the R D.F.

My thanks are also due to Miss Cynthia Collins for typing the text and Miss Elaine Gascoyne for typing the figure captions.

I wish to acknowledge the financial support of the Science and Engineering Research Council and the British Technology Group.

I would like to thank all my friends of the Materials Section for many rewarding discussions and assistance at various stages of this study.

I am grateful to my friends Sankar da, Siddeshwar da, Dilip, Avijit, Paminder and Fereshteh for making my stay at Imperial College a happier one.

Finally, I would like to express my gratitude to my parents, my family and Philippa for their unfailing patience and encouragement throughout.

CONTENTS

CHAPTER 1

INTRODUCTION

The control of electronic properties in crystalline semiconductors by substitutional doping has been one of the most significant steps in the development of semiconductor devices and of solid state electronics technology. Similar control of the electronic properties of amorphous semiconductor materials is potentially of equal importance.

In 1975 W.E. Spear and P.G. LeComber [1] reported that they succeeded for the first time in doping hydrogenated amorphous silicon (a-Si:H), both n-type and p-type, thereby changing its conductivity by many orders of magnitude in each case. They prepared their a-Si:H films by radio frequency glow discharge (R.F.G.D.) of silane (SiH_4) [1].

Since this development, a-Si:H has been studied in great depth by many research groups all over the world. This has enabled its application in a wide variety of fields, including low cost solar cells [2,3] and xerographic layers [4,5]. Other noteworthy applications involve the fabrication of matrix addressable thin film transistors [6] and colour image sensors [7]. A review of progress in device fabrication is given by Hamakawa [8].

Crystalline silicon has a well defined structure. It is a face-centred-cubic solid in which each atom is tetrahedrally bonded to four others. This basic structure

is repeated in all three dimensions giving rise to long range order. The resulting periodic structure gives rise to a band structure in which the energies of electrons localised in bonding states are separated from 'free' electrons in the crystal by an energy gap in which there are no allowed electronic states.

Amorphous silicon, in contrast, exhibits no long range order and the structure can have an infinite number of arrangements. However, at a local level each atom in amorphous silicon can have tetrahedral co-ordination, although with varying, rather than fixed, bond angles and lengths being possible; some may be unable to form four bonds so that one or more bond is unfilled - referred to as dangling bonds. Due to the above possibilities long range order is totally lost. This disorder results in localisation of electrons [9] creating a drastic reduction in their mobility, compared with the electron mobility in extended states. The resulting mobility gap is analogous and close in energy to the energy gap between conduction and valence bands in the crystalline silicon, C-Si. When hydrogen is incorporated in the amorphous silicon it takes up the dangling bonds, thereby reducing the density of trapping states for electrons.

The existence of disorder in the structure of the amorphous state gives rise to a distribution of localised states, N(E), situated in the mobility gap, and this N(E) determines the transport and recombination processes in amorphous silicon. For example, the electron and hole

drift mobilities in a-Si:H are approximately 10^{-1} and 10^{-4} cm^2 s^{-1} V^{-1} respectively and are very small compared to those of crystalline silicon (electrons 1600, holes 400 cm^2 s^{-1} V^{-1}) and the recombination lifetime for free carriers being in the range 10^{-11} to 10^{-5} sec compard with $\sim 10^{-3}$ sec for C-Si. The incorporation of hydrogen reduces N(E) to a level such that substantial free carrier densities can be achieved by doping the material with group V (for electrons) or group III (for holes) impurity atoms. Intrinsic material is also able to exhibit significant photoconductivity.

The high optical absorption coefficient at visible wavelengths, its doping capability and the ability to be grown or deposited over a large area cheaply makes hydrogenated amorphous silicon a potentially important material for practical applications.

Over the past twenty years there have evolved various techniques for deposition of a-Si:H films. Notable among them are the following:

(1) Dissociation of silane in a low power glow-discharge (G.D.) decomposition. This method was developed at STL Laboratories by Chittick et al [10] in the late sixties, and subsequently by Spear et al [1,11,12] and by Knights [13]. This method is probably the most widely used today.

(2) Sputtering of a silicon target in an argon and hydrogen mixture. The silicon target may be in

the polycrystalline form, compressed powder or single crystal wafer [14]. This process has been described extensively by Anderson et al [15,16,17] and Moustakas et al [18]. In this technique high energy (several electron volts) ions are directed by an electric field towards the target to dissociate groups of atoms from the target material and subsequently deposited onto a substrate.

(3) Chemical vapour deposition (C.V.D.) provides a widely used method [19,20] for the deposition of a-Si:H. The method employs a furnace to pyrolyse silane at temperatures greater than 500°C. The substrate temperature is lower than the gas temperature and a-SiH_x film condenses on the substrate. However, the substrate being at a relatively high temperature, not all the dangling bonds are taken up by hydrogen and hence the material develop a relatively high density of defects [21] and are usually post-hydrogenated by annealing in hydrogen [22].

The principal objectives of these techniques have been:

(i) To deposit film with a low N(E) in the mobility gap and hence a good room temperature

photoconductivity.

(ii) The ability to dope the film either n-type or p-type efficiently.

(iii) The deposition to be carried out over a large area.

(iv) To achieve as high a growth rate as possible, this being a commercially important factor.

With the above in mind the work in this laboratory was carried out. Two different techniques were adopted for the purpose. They are as follows:

(a) Amorphous silicon prepared by r.f. sputtering in argon and silane mixtures using undoped, n-type and p-type targets.

(b) Activated reactive evaporation (ARE) of silicon in hydrogen for the production of intrinsic hydrogenated amorphous silicon films (a-Si:H) and the production of doped films by the introduction of the dopant gases, phosphine and diborane or by pre-doping of the silicon evaporation source.

The first method was reported by Anderson in 1980 [14]. Intrinsic a-Si:H films were successfully produced and doped films were prepared using n-type and p-type targets. However, the doping efficiency proved to be extremely low (10^{-5} - 10^{-6}). It was concluded that the majority of dopant

atoms failed to achieve tetrahedral co-ordination and were, therefore, electrically inactive. The writer worked on development of this process (1980-81) with a view to improving doping efficiency, including the introduction of interstitial dopants. However, only very limited success was achieved. The work has been summarised in the publication mentioned above which is included in Appendix 1. References will be drawn in this thesis whenever necessary to this paper but no detailed report of the work is presented here.

Doping from gaseous hydrides proved to be successful both in glow discharge deposition (Spear and LeComber [1]) and in sputter deposition in argon-hydrogen mixtures (Anderson et al [17], Moustakas et al [18]). It was argued from this that, in order to achieve tetrahedral co-ordination, the dopant atom must carry a hydrogen atom with it into the film. In order for this to occur when the dopant is present as isolated atoms, a gas phase reaction is required involving a three body collision of Si, H and the dopant atom. The probability of this occurring in the sputtering system is low due to the high energies of the sputtered atoms and the relatively low gas pressures used (5-10 millitorr). An alternative process was therefore sought in which the necessary gas-phase reaction could be enhanced.

The second process investigated was the Activated Reactive Evaporation (ARE) [23] in combination with ion-plating [24]. ARE is a high rate deposition process in which a gas phase reaction is promoted between the

evaporating species and a gas admitted to the vacuum. The gas is ionised by thermionic electrons emitted from the molten pool of the evaporant being collected by a low voltage probe. The substrate was biased during deposition and thereby ion bombardment of the growing film was promoted as in the conventional ion-plating process. Negative (d.c.),positive (d.c.), self bias and r.f. biasing were used. This thesis reports the extensive investigation of this process and of the properties of a-Si:H films produced using it.

A systematic study of the various parameters involved in the deposition process, including substrate temperature, gas pressure, input power to the electron beam, probe power for collecting the thermionic electrons, and substrate bias was carried out. The resulting films were characterised using optical measurements, both visible and infrared, and electrical measurements including dark conductivity and photoconductivity as a function of reciprocal temperature. Annealing properties of the films were investigated. This investigation was devoted to the production of intrinsic a-Si:H films.

Once the investigation for the preparation of an adequate intrinsic film was complete, doped silicon ingots were used to try to deposit doped films of both p-type and n-type. Doping was successful, but again with a low doping efficiency. Alloys of silicon and antimony were used in some crude experiments, and it was observed that the conductivity of the films could be increased by several orders of magnitude. This supports the view that doped films could be obtained

starting from a doped source, provided there are enough species of the dopant atoms available for a three body collision.

A set of experiments was also carried out for the investigation of gas phase doping of the ARE films using phosphine and diborane. Optical and electrical measurements on these films were the same as in those used for the undoped films. The results were compared to those obtained by other workers using glow discharge techniques. A remarkable similarity in the optical and electrical properties (both intrinsic and doped) between glow discharge and ARE films was observed but with the advantages that the deposition rate in the ARE process is up to 30 times faster and that no silane is used [25].

CHAPTER 2

ELECTRONIC PROPERTIES

2.1 INTRODUCTION

This chapter summarises some aspects of the electronic processes which occur in amorphous Si:H, and which are relevant to work described in this thesis.

The difference between the band structures of crystalline and amorphous semiconductors is indicated and various models of density of state distribution, available for the description of electronic processes in amorphous materials, are discussed. The passivating of the dangling bonds in amorphous silicon using hydrogen is discussed in detail in chapters 4 and 5 and is not included here.

The d.c. conductivity mechanisms,which are believed to occur in amorphous semiconductors,are discussed in sections 2.3.1 to 2.3.4.

Finally the photo-carrier generation and recombination processes are considered.

2.2 BAND STRUCTURES IN AMORPHOUS SILICON

In the introductory chapter the distinction between crystalline and amorphous semiconductors was briefly outlined.

In a perfect crystal there exists three primitive basis vectors $\underset{\sim}{x}$, $\underset{\sim}{y}$, $\underset{\sim}{z}$ and a translation $\underset{\sim}{T}$ between two lattice points is described by

$$\underset{\sim}{T} = m\underset{\sim}{x} + n\underset{\sim}{y} + p\underset{\sim}{z} \qquad (2.1)$$

where m, n and p are integers. The crystal structure remains invariant under any translation. The band structure (Energy Momentum relationship) of such a crystalline solid is obtained by the solution of the Schrödinger equation with a suitable potential energy function which describes the periodicity of the lattice. Solutions are of the Bloch form in which the wavefunction of an electron is given by

$$\psi_k(\underset{\sim}{r}) = U_k(\underset{\sim}{r}) \exp(i\underset{\sim}{k}.\underset{\sim}{r}) \qquad (2.2)$$

where $U_k(\underset{\sim}{r})$ is periodic in $\underset{\sim}{r}$, which is the periodicity of the direct lattice of the crystal. There are regions of energy for which no Bloch function solutions of the Schrödinger equation exist. The overall result is that of bands of allowed states separated by energy gaps. A band which is unoccupied by electrons at absolute zero provides "extended states" for electrons excited into it at finite temperature since, due to there being a small number of electrons near the bottom of the band, they behave as free electrons, moving throughout the crystal lattice. The highest filled band of states in a semiconductor, the valence band represents electrons in states in the bonding system; these are also extended throughout the crystal. The band above this is the conduction band.

In amorphous materials the electron wavefunctions will not generally have the periodic Bloch form but solutions of the Schrödinger equation must exist [1]. These will

each be described by a density of states N(E), (the number of eigen states per unit energy dE) forming bands of extended states.

Using Anderson's theory [2], Mott [3] showed that fluctuations in the potential caused by the disorder in amorphous materials lead to the formation of localised states which occupy energy levels adjoining those of the extended states in the bands. These form "tail states" below the conduction band and above the valence band. Further he proposed that there should be a distinct boundary between the extended and localised states at which the carrier mobility will drop suddenly from the extended state value to a much lower value for localised states.

Different models have been proposed for the energy distribution of density of localised states in amorphous semiconductors. They are all similar in the sense that they use the concept of localised states in the band tails. The variations between models concern the "shape" of this tail as a function of energy. Fig. 2.1 shows, schematically, the main features of two of the models proposed and a third obtained experimentally by Spear et al [4,5] for amorphous silicon (see Fig. 2.1c). The full lines are the total density of states determined from field effect experiments and the arrow on each curve shows the position of the Fermi level. Curve 1 represents glow discharge specimen deposited at ~520K and Curve 2 represents data for evaporated silicon specimen.

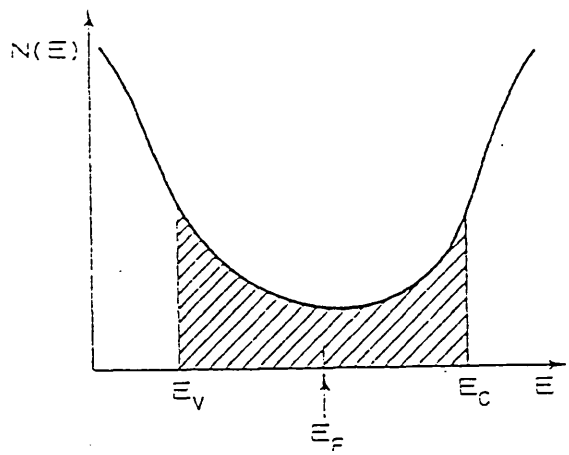

a) The Cohen-Fritzsche-Ovshinsky model.

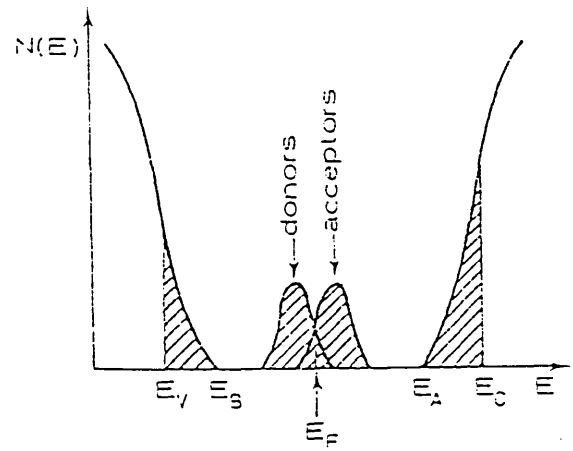

b) The modified Mott-Davis model.

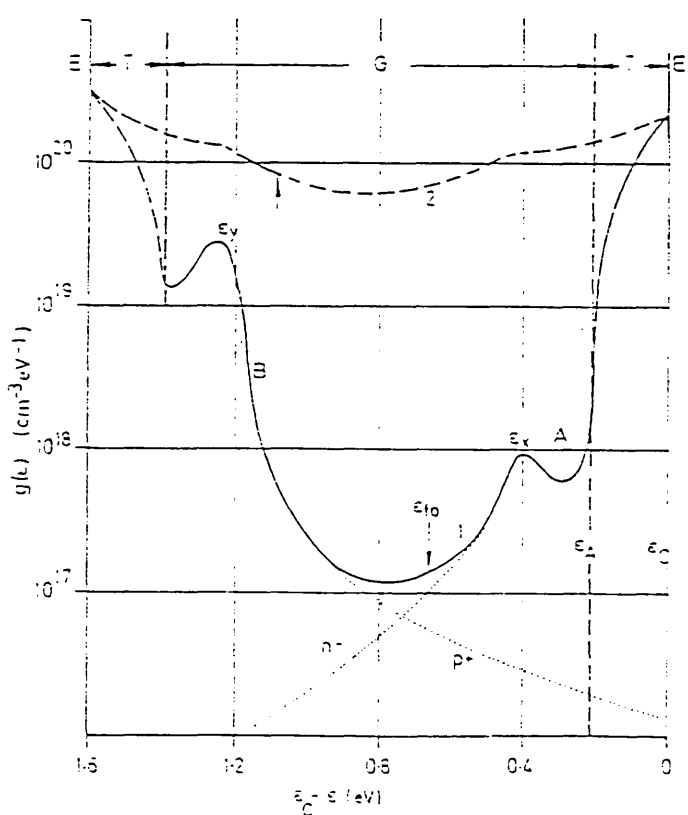

c) Experimentally obtained density of states. (After P.G. Lecomber and W.E. Spear, ref. 4,5).

Density of states distributions for a-Si specimens. The full lines are the total density of states determined from field-effect experiments and the arrow on each curve shows the position of the Fermi level. Curve *1*: glow discharge specimen. $T_d \simeq 520$ K. *A* and *B* are the assumed division of this data into acceptor-like and donor-like states respectively. Curve *2*: evaporated specimen. *E*, extended states; *T*, tail states; *G*, gap states.

Fig. 2.1 Schematic representation of density of states.

Fig. 2.1a shows the Cohen-Fritzsche-Ovshinsky (CFO) model [6]. The main features are the extension of the tail states right across the mobility gap. The positions of E_v and E_c are the mobility edges [5] as defined by Mott. Electronic wavefunctions between E_v and E_c are localised.

Fig. 2.1b shows the modified Mott and Davis [7] model proposed on the basis of the results from the spin density measurements by electron spin resonance (ESR). The tails of the localised states are narrow and extend a few tenths of an electron volt into the mobility gap. The states in the midgap are due to dangling bonds which may either act as acceptors or donors.

The interpretation of electrical transport data is closely linked to the energy distribution of the density of states. According to Mott and Davis, based on their model, there can be three different conduction mechanisms in amorphous semiconductors. The contribution made by each mechanism to the total conductivity is different in different temperature regions. At very low temperatures the conduction occurs by thermally assisted tunnelling between (hopping) states at the Fermi level. At higher temperatures conduction is by hopping in the localised tail states. At still higher temperatures carriers are excited across the mobility edge into the extended states, where the mobility is much higher.

2.3 Conduction Mechanisms

2.3.1 D.C. Electrical Conductivity

As explained in the last section the Mott and Davis model for the density of state distribution leads to three different conduction processes:

(a) extended state conduction,

(b) conduction in band tails,

(c) conduction in localised states at the Fermi energy.

These three mechanisms are considered in the following three sections.

2.3.2 Extended State Conduction

The conductivity in any semiconductor may be written as [15]

$$\sigma = q\int N(E)\ \mu(E)\ f(E)\ (1-f(E))dE \qquad (2.3)$$

where

N(E) is the density of states

$\mu(E)$ is the mobility

f(E) is the Fermi-Dirac distribution function for an electron and describes the probability that an energy state E is occupied by an electron when the lattice is in thermal equilibrium.

$$f(E) = \frac{1}{1 + \exp(\frac{E-E_F}{kT})} \qquad (2.4)$$

where

E_F is the Fermi energy

T is the absolute lattice temperature

k is Boltzmann's constant

Similarly, (1-f(E)) is the probability that a hole occupies a state at an energy, E.

$$(1-f(E)) = \frac{1}{1 + \exp(\frac{E_F-E}{kT})} \qquad (2.5)$$

In the Mott and Davis model (Fig. 2.1b) E_F is in the middle of the mobility gap so that for $E \geq E_c$ Boltzmann statistics apply and eqn. (2.4) may be approximated to

$$f[E] = \exp(-(\frac{E-E_F}{kT})) \qquad (2.6)$$

and eqn. (2.5) gives $1-f(E) \simeq 1$

Assuming constant density of states and constant average mobility, μ_c for electrons in the extended states, and using eqn. (2.6), eqn. (2.3) can be written as

$$\sigma = qN(E_c)\ \mu_c \int_{E_c}^{\infty} \exp(-(\frac{E-E_F}{kT}))dE \qquad (2.7)$$

$$\sigma = qN(E_c)\ \mu_c\ kT \quad \exp(-(\frac{E_c-E_F}{kT})) \qquad (2.8)$$

The number of electrons n is given by

$$n = \int_{E_c}^{\infty} N(E_c)\ \exp(-(\frac{E-E_F}{kT})dE \qquad (2.9)$$

$$n = N(E_c)\ kT \quad \exp(-(\frac{E_c-E_F)}{kT})) \qquad (2.10)$$

For diffusive transport [8] $\mu_c \propto \frac{1}{T}$ and therefore the conductivity can be written as

$$\sigma = \sigma_o \exp(-(\frac{E_c-E_F}{kT})) \qquad (2.11)$$

where σ_o is temperature independent for constant $N(E_c)$.

A plot of $\ell n\,\sigma$ against 1/T yields a straight line of slope $-(E_c-E_F)/k$ provided that (E_c-E_F) is constant. In fact (E_c-E_F) has been shown to be temperature dependent. Tsang and Street (1979) [9] have shown that the mobility gap decreases with increasing temperature. It has also been shown by Beyer et al (1977) [10] that the Fermi level position is temperature dependent from the interpretation of thermoelectric power data.

If (E_c-E_F) is assumed to vary linearly with temperature then,

$$(E_c-E_F)_T = (E_c-E_F)_o - \delta T \qquad (2.12)$$

The above coefficient δ is a function of energy. Jones et al [11] have suggested that it is composed of two parts. In the first instance, for $\delta < 0$, the "statistical shift" becomes important in the more heavily doped specimens when E_F approaches the rapidly rising tail state distribution near E_A (see Fig. 2.1c). Spear and Le Comber [12] suggest that this arises from the "statistical overflow" of carriers to energies above E_F, which results in the movement of E_F away from E_c with increasing temperature. The above implies a change with temperature in the occupation statistics when $dN(E_F)/dE$ is positive.

Secondly, for $\delta > 0$, more important in undoped or lightly doped specimens when E_F is near the central density of state minimum, the variation in (E_c-E_F) arises from the

fact that (E_c-E_v) decreases with increasing temperature.

Substituting for $(E_c-E_F)_T$ from eqn. (2.12) eqn. (2.8) becomes

$$\sigma = qN(E_c)\ \mu_c\ kT\ \exp(\frac{\delta}{k})\ \exp[-\frac{(E_c-E_F)_o}{kT}\ ] \qquad (2.13)$$

The term $(E_c-E_F)_o$ is the mobility gap at temperature T = 0.

Therefore the expression for the σ_o term in eqn. (2.11) becomes

$$\sigma_o = q\ \mu_c\ N(E_c)\ kT\ \exp(\frac{\delta}{k}) \qquad (2.14)$$

For diffusion μ_c is inversely proportional to temperature and thus σ_o, the pre-exponential factor, is temperature independent. The value of δ has been estimated by Griffith (1977) [13] to be ~2.4 x 10^{-4} eV k^{-1} from theoretical calculations. Tsang and Street (1979) [9] found values of 4.3 x 10^{-4} eV k^{-1} from optical absorption measurements on glow discharge silicon. Jones et al [11] calculated a value of 2.5 x 10^{-4} eV k^{-1}.

Mott [3] made an estimate of the pre-exponential σ_o to be 350 Ω^{-1} cm^{-1}. Anderson and Paul (1982) [14] reported values from 5 x 10^3 Ω^{-1} cm^{-1} in undoped amorphous silicon to 10 Ω^{-1} cm^{-1} in PH_3 doped silicon. In general the values of σ_o lie between 10 and 1000 Ω^{-1} cm^{-1}[15].

Recently Mott [16] has proposed a correction for multiple scattering of carriers in a disordered system from which he calculates the value of σ_o to be in the range 15-25.

Transport in the extended states is the dominant form of conductivity mechansim above approximately 250K and below approximately 400K (Le Comber et al 1977 [17], Anderson and Paul (1981) [14], in a-Si:H). Mott and Davis [1] (page 215) assume that the presence of short range order rather than of point defects gives rise to the mobility edges. This view arises from the fact that deposition temperature (Spear et al 1972, 1973) [18,19] does not affect the position of the mobility edge and defect concentration would be a function of deposition temperature. Since the hydrogen content is dependent on the deposition temperature it also follows that incorporation of hydrogen does not affect the position of the mobility edges (Brodsky et al 1977) [20].

2.3.3 Conduction in Band Tails

With reference to Fig. 2.1b, band tail conduction occurs by thermally activated hopping of electrons and holes between localised states in the respective band edges. Assuming conduction by electrons,

$$\sigma_{hop} = \sigma_1 \exp[-(\frac{E_A - E_F + W_1}{kT})] \qquad (2.15)$$

where W_1 is the hopping activation energy. A plot of σ_{hop} vs. 1/T gives a straight line. This mechanism is predominant at lower temperatures (see Mott and Davis book, pp.220-227) [1]. The term σ_1 is much smaller than σ_o due to the lower mobility of electrons in the localised states and also the value of N(E) at E_A (see Fig. 2.1b) being much smaller than at E_c.

2.3.4 Hopping at the Fermi Energy

With reference to Fig. 2.1b and Mott and Davis [1], conduction at the Fermi level occurs between states by thermally assisted hopping. If nearest neighbour hopping takes place, i.e. when only a very narrow band width b of states exists at E_F, then

$$\sigma_{hop} = \sigma_2 \exp\left(-\frac{W_2}{kT}\right) \qquad (2.16)$$

where W_2 is the hopping activation energy.

When N(E) varies as in Fig. 2.1b, hopping is not necessarily between nearest neighbours and variable range hopping takes place [1]. The conductivity is then given by,

$$\sigma_{hop} = \sigma'_2 \exp\left(-\frac{B}{T^{\frac{1}{4}}}\right) \qquad (2.17)$$

where

$$B = \left\{\frac{2\alpha^3}{kN(E_F)}\right\}^{\frac{1}{4}} \qquad (2.18)$$

where the electronic wavefunctions decay at a rate $\exp(-\alpha r)$ with distance r from their centres. α is called the wave-function decay constant.

On a plot of $\ell n\sigma$ vs. $1/T$, hopping conductivity at the Fermi level appears as a curve. The activation energy is small and becomes smaller at lower temperatures. The existence of hopping at the Fermi level is shown up as a straight line when $\ell n\sigma$ vs. $T^{-\frac{1}{4}}$ is plotted.

If the density of states at the Fermi level is very high then the conduction at the band tails may never

dominate in any temperature range and a direct transition from extended state conduction to hopping at Fermi level takes place (Mott and Davis, page 221) [1]. This would be the case in non-hydrogenated amorphous silicon film where there was no hydrogen to take up dangling bonds.

2.4 PHOTO-GENERATION AND RECOMBINATION

Shockley-Read [21] statistics were successful in describing non-equilibrium steady-state processes in crystalline semiconductors. The work described four generation-recombination processes occurring through a single trapping level. Simmons and Taylor [22,23,24] considered an extension to the Shockley-Read approach for semiconductors with an arbitrary distribution of traps in the energy gap to obtain the recombination statistics in such a system. A summary of their work is described below in the following sections.

The four kinetic processes for a particular trapping level are illustrated in Fig. 2.2. G represents the rate of generation of electron-hole pairs which is assumed to be directly proportional to the light intensity.

The process "a" is the capture rate of free electrons at empty traps given by

$$r_a = v\sigma_n n N_t (1-f) \qquad (2.19)$$

where v is the thermal velocity, σ_n is the trap capture cross-section for electrons, n is the free electron density, N_t is the trap density of the level, and f is the

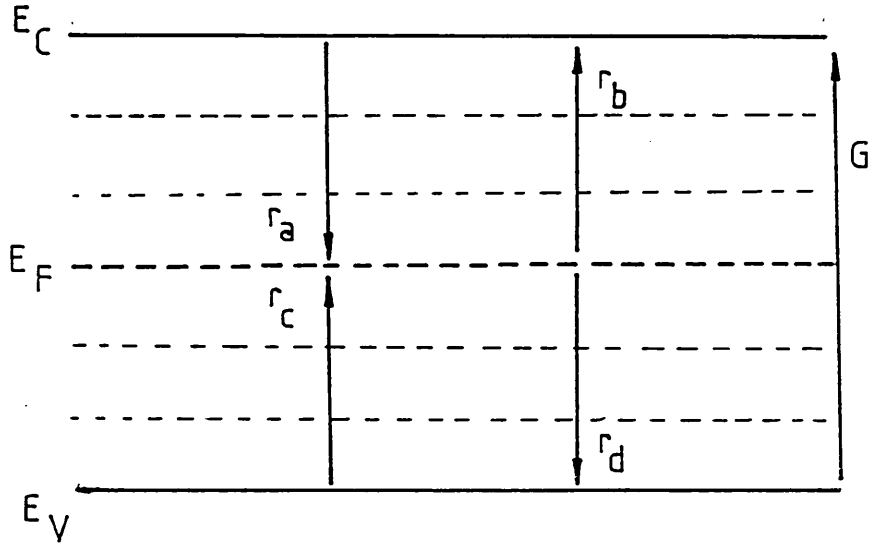

Fig. 2.2 Kinetic processes associated with a particular trapping level of a distribution of trapping levels.
(After G.W. Taylor and J.G. Simmons, ref. 22)

non-equilibrium occupancy function. The term $N_t(1-f)$ is the number of empty states in the trapping level.

In process "b", the rate of emission of electrons excited from filled traps to the conduction band, is given by

$$r_b = e_n N_t f \tag{2.20}$$

where $N_t f$ is the number of filled traps and e_n is the emission rate from the trap.

Similarly, for hole capture and emission rate at E_t

$$r_c = v\sigma_p \, p \, N_t f \tag{2.21}$$

$$r_d = e_p N_t (1-f) \tag{2.22}$$

In thermal equilibrium $r_a = r_b$ and $r_c = r_d$ and e_n and e_p can be shown to be [21],

$$e_n = v \, \sigma_n \, N_c \exp\left[\frac{(E_t - E_c)}{kT}\right] \tag{2.23}$$

$$e_p = v \, \sigma_p \, N_v \exp\left[\frac{(E_v - E_t)}{kT}\right] \tag{2.24}$$

where E_t is the energy of the trap level and N_c and N_v are the effective density of states in the conduction and valence bands respectively.

The free hole (p) and free electron (n) concentrations for constant capture cross-sections in the case of slowly-varying trap distributions are given by

(Simmons and Taylor) [24]

$$n = \frac{G}{v\sigma_n \int_{E_{Fo}}^{E_{tn}} N(E)dE} \tag{2.25}$$

and

$$p = \frac{G}{v\sigma_p \int_{E_{tp}}^{E_{Fo}} N(E)dE} \tag{2.26}$$

where E_{tn} and E_{tp} are defined to be the quasi-Fermi levels for trapped electrons and holes respectively (see Fig. 2.3). The important feature of the above equations is that the free electrons and holes recombine via states between the quasi-Fermi levels E_{tn} and E_{tp} and therefore it would be important for a photoconductor to have a low density of states between the quasi-Fermi levels (see Fig. 2.3).

These quasi-Fermi levels (for trapped electrons and for trapped holes) are defined by

$$E_{tn} = E_{Fo} + kT \ln \left(\frac{\sigma_p p + \sigma_n n}{\sigma_p n_o}\right) \tag{2.27}$$

$$E_{tp} = E_{Fo} - kT \ln \left(\frac{\sigma_p p + \sigma_n n}{\sigma_p p_o}\right) \tag{2.28}$$

A change in the electrical conductivity of a material when it is exposed to light is known as photoconductivity, and in such a process the excess carrier densities Δn and Δp are of interest, and are defined by

$$\Delta p = p - p_o \tag{2.29}$$

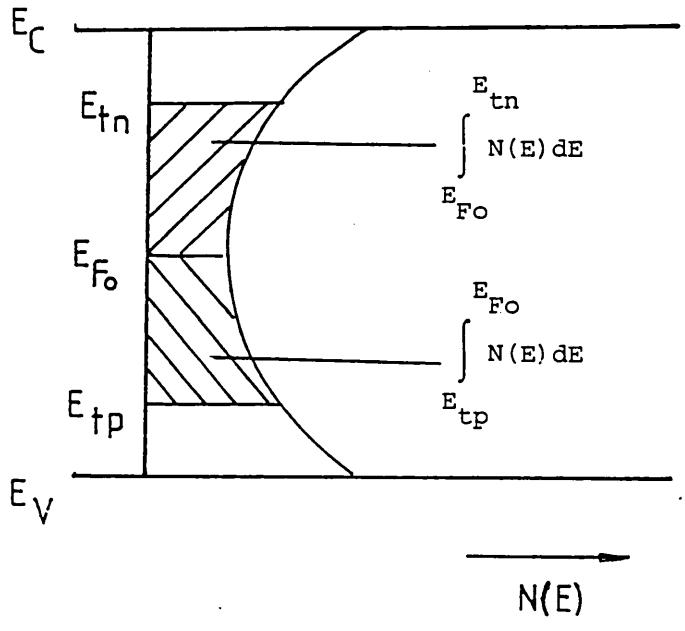

Fig. 2.3 States between E_{tn} and E_{tp} are only effective in the recombination process.
(After G.W. Taylor and J.G. Simmons, ref. 22)

and

$$\Delta n = n - n_o \tag{2.30}$$

where p_o and n_o are the equilibrium concentrations of free holes and free electrons respectively and are given by

$$p_o = N_v \exp(-\varphi/kT) \tag{2.31}$$

and

$$n_o = N_c \exp([(\varphi - E_g)/kT] \tag{2.32}$$

where N_v and N_c are the effective densities of states at the valence and conduction mobility edges, E_g is the energy of the mobility gap, and $\varphi = E_{Fo} - E_v$ is the activation energy of the dark conductivity of the photoconductor.

Viewing eqn. (2.30) for n-type semiconductors, two situations can arise,

(I) $\Delta n << n_o$

or

(II) $\Delta n >> n_o$

In the first instance (low light and high temperature) the excess carrier density is much smaller than the equilibrium carrier density; it has been shown that [15]

$$\Delta n = \frac{G}{2\sigma_n n_o} \tag{2.33}$$

In this region the photo-currentvaries linearly with the excitation intensity and is sensitive to the states between the electron and hole quasi-Fermi levels as mentioned earlier, and is commonly known as a monomolecular recombination.

In the second case when the excess carrier density is much greater than the equilibrium carrier density it has been shown that, [15], high illumination and low temperature,

$$n = \left(\frac{G}{\sigma_n}\right)^{\frac{1}{2}} \qquad (2.34)$$

and the photo-current is proportional to the square root of the light intensity. In such a process electrons and holes recombine directly across the mobility gap, a process normally referred to as a bimolecular recombination. In such cases the recombination process is no longer dependent upon the distribution of states between the quasi-Fermi levels, E_{tn} and E_{tp}.

In this case the recombination rate of the electrons is proportional to the number of holes (trapped or otherwise). In such a case the plot of photo-current against 1/T is as shown in Fig. 2.4 (after Mott and Davis, page 259) [1]. This behaviour was observed in the intrinsic A.R.E. deposited samples at high light intensities.

Most of the measurements carried out were in the region II (Fig. 2.4). In this region $i_p >> i_d$ where i_p is the photo-current and i_d is the dark current. In such conditions i_p is expected to be proportional to $G^{\frac{1}{2}}$ (Mott and Davis, page 259), [1].

For a high density of gap states, monomolecular recombination takes over [25]. Spear [25] has confirmed bimolecular recombination to occur only in glow discharge

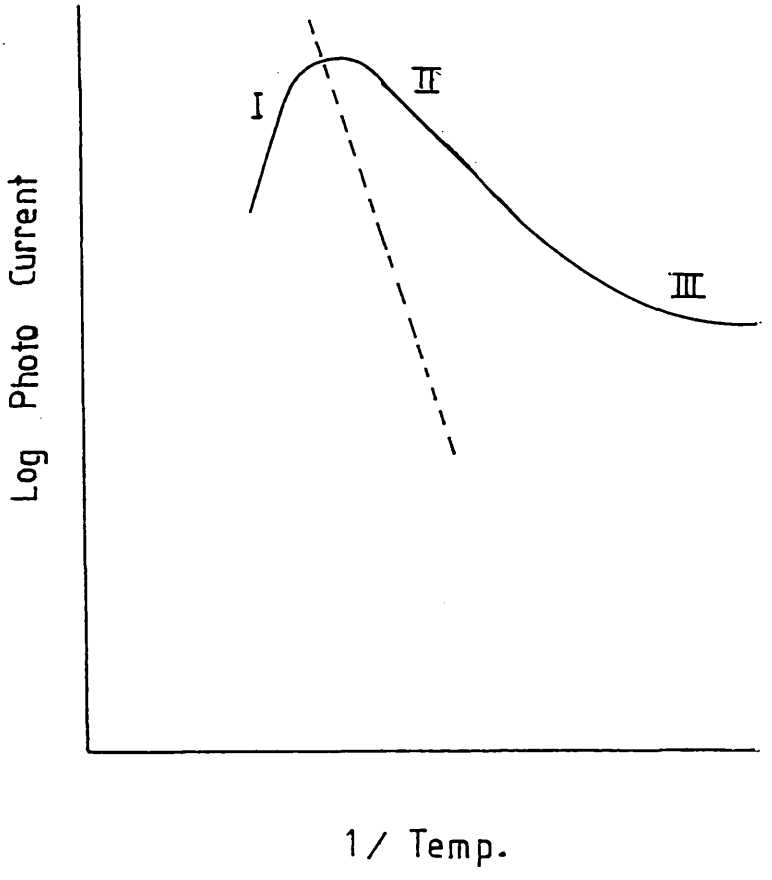

Fig. 2.4 The schematic representation of the temperature dependence of photo current. The broken line is the dark current. (After N.F. Mott and E.A. Davis, ref. 1)

silicon deposited at high substrate temperature (low density of state material).

However, from our results for a typical intrinsic film (Fig. 2.5) using Green light (546 nm) a relationship of the following form was observed for the high illumination range

$$J_{ph} \propto F^{\gamma} \tag{2.35}$$

where J_{ph} is the photo-current, F is the illumination intensity and γ was found to have a value of about 0.7.

Carles et al [26] observed values of 0.75 for γ in amorphous selenium. Following Rose [27], they interpreted their results in terms of an exponential distribution of hole traps N_t, lying in the band-gap above the valence band-edge E_v

$$N_t = A \exp -\left(\frac{E-E_v}{kT_c}\right) \tag{2.36}$$

where A and T_c are constants which characterize the distribution; T_c is given by

$$\gamma = \frac{T_c}{(T+T_c)} \tag{2.37}$$

They also observed values of $\gamma > 1$, for low illumination. This transition was explained in terms of the passage of the hole quasi-Fermi level from an exponential to a uniform trap distribution.

Vanier et al [28,29] and Drazin [30] have observed transition from supralinearity ($\gamma > 1$) at low illumination to

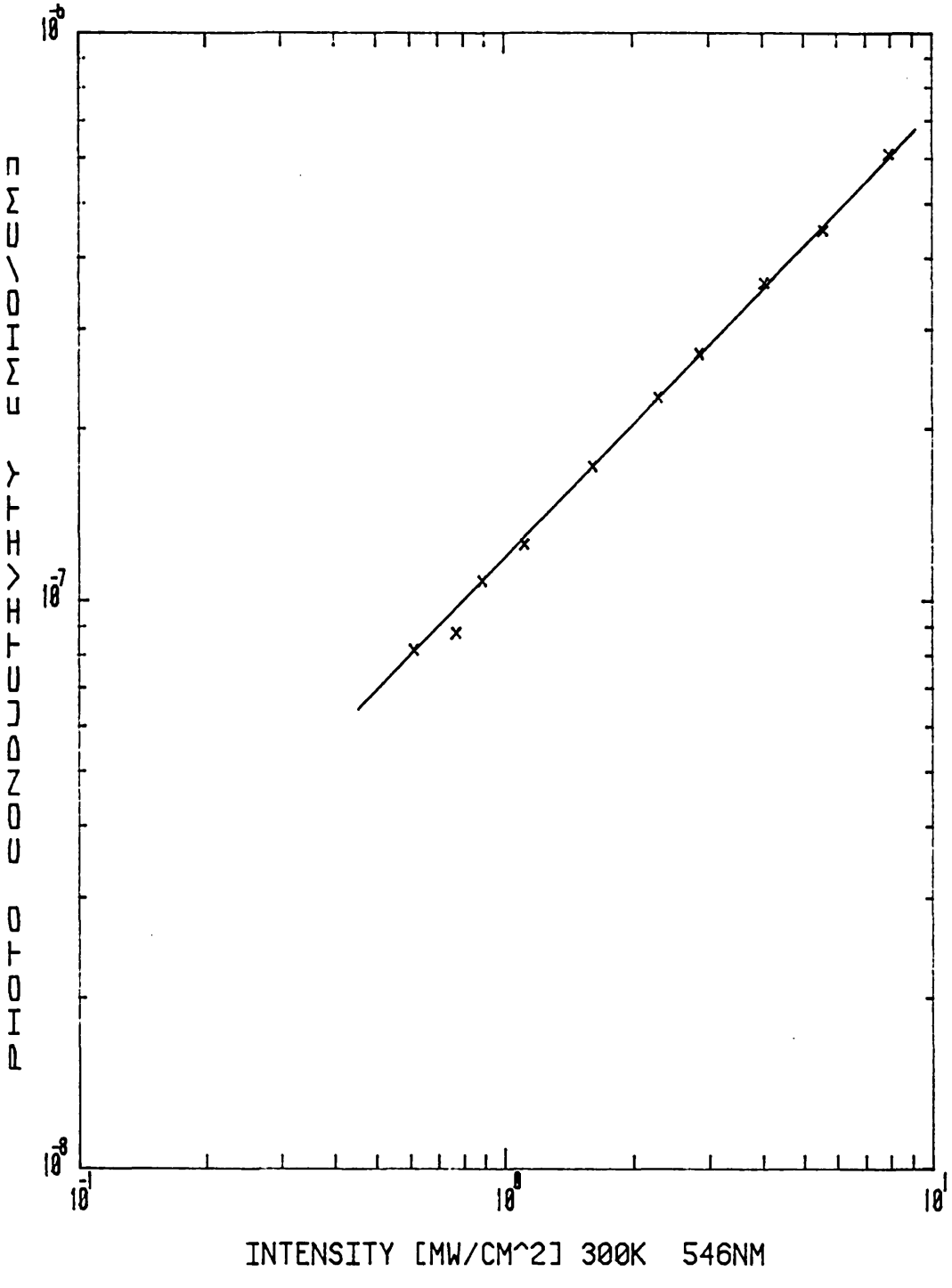

Fig.2.5 A plot of photoconductivity vs. intensity using a 546nm. wavelength light source.

sublinearity ($0.5 < \gamma < 1$) at high illumination. They both explain their results in terms of a two level model proposed by Rose [27]. Two classes of recombination centres exist in the gap. Class 1 consists of a species of traps, at energy E_1, whose electron capture cross-sections σ_n is smaller than that for holes (σ_p). These are near the valence band edge. Class 2 traps at an energy E_2 near the middle of the band gap and have an equal capture cross-section for electrons and holes. In amorphous materials these states are of a broad distribution rather than distinct.

At low levels of illumination, the lifetime of photogenerated electrons is limited by recombination states at E_2. At room temperature, the quasi-Fermi level for free carrier holes φ_p lies between E_1 and E_2,so most of the holes go to the more efficient electron recombination states at E_2. This situation leads to a relatively low photo-current.

At higher illumination intensities φ_p moves down to states in E_1, populating these states with holes; holes move down from E_2 to E_1. Since the capture cross-section for electrons is less at E_1 than at E_2, this transfer leads to longer electron lifetimes and a higher photoconductivity.

In view of the above argument and the experimental result of $\gamma \simeq 0.7$, it is considered that A.R.E. prepared amorphous silicon has a similar distribution of traps to those prepared by glow discharge silicon.

CHAPTER 3

SAMPLE PREPARATION

3.1 THE BASIC EXPERIMENTAL PROCESS

As stated earlier, the activated reactive evaporation process creates a plasma in which a gas phase reaction between the evaporating atoms and an ionised gas can occur. A schematic diagram of the process is shown in Fig. 3.1. A primary electron beam of typical power 1.5-2.0 kW is used to melt a pool on the surface of the silicon ingot which is situated in a water cooled copper crucible. This molten pool is a source of thermionic electrons. A few centimetres above the pool a stainless steel circular electrode is situated. By applying a potential of approximately 300 V to this electrode the thermionic electrons are collected from the surface of the molten pool. Hydrogen is admitted to the chamber (for intrinsic film preparation) at a flow rate of about 50-60 SCCM and a pressure of about $\sim 10^{-2}$ torr is allowed to be built up in the reaction chamber. The relatively slow, thermionic electrons are a highly active ionising agent in that the cross-section for ionisation of the gas atoms is large at their energy of ~300 eV. Thus a hydrogen plasma is formed between the molten silicon pool and the circular electrode. The hydrogen plasma is chemically highly reactive and is able to react with the evaporating silicon atoms to form ions of the type SiH_x, where x will be between 1 and 4. These species are of the same type as those present in the plasma created by an r.f. glow discharge

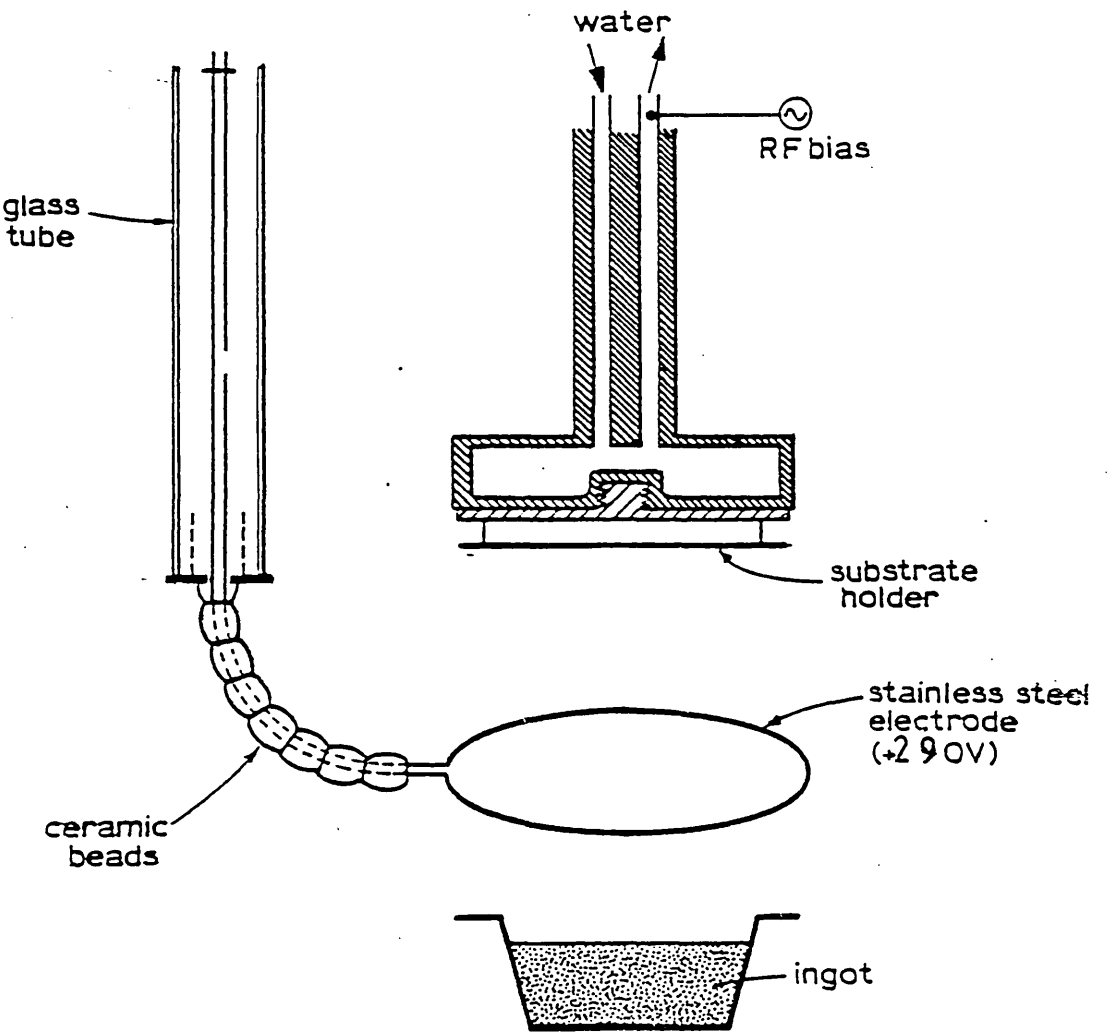

Fig. 3.1 A schematic diagram of the ARE process.

in silane. By adjusting the silicon evaporation rate or altering the hydrogen pressure and adjusting the electrode voltage one may vary the degree of hydrogenation of the deposited film.

From infrared absorption measurements (Chapter 4) it was found that the deposited films were hydrogenated. However, their electrical properties were relatively poor (Chapter 5) and there was evidence of a high density of microvoids in the films (Chapter 5).

To remove these defects and improve the electrical quality of the films a negative r.f. bias is applied to the substrate during deposition. This technique is known as ion-plating and has been industrially developed for the deposition of hard coatings [1,2]. In the present process the bias has two important effects. The first is that the plasma is extended to fill the whole volume between the molten pool and the substrate, thereby increasing the efficiency of the gas-phase reaction. The second is that the film is subject to bombardment by positive ions from the plasma during growth. This has the effect of densifying the film and eliminating microvoids. The physical mechanism is that the additional energy input to the film during growth increases the mobility of the deposited atoms. They are, therefore, more able to find fully-bonded, low-energy positions during growth of the film and there is less likelihood of void formation [3].

3.2 THE DEPOSITION CHAMBER

A schematic diagram of the deposition chamber is shown in Fig. 3.2 (not to scale). Some details in the figure have been omitted for simplicity but are described in the text.

The basic chamber is an Electrotech electron beam evaporation unit. It is a front loading, swing door type, stainless steel "chamber jacket" system. The "chamber jacket" is water cooled. The chamber is pumped via two Edwards F 603 diffusion pumps and backed by an Alcatel rotary pump. The chamber is divided into two sections by means of a heavy, stainless steel plate forming an upper chamber and a lower chamber. Under normal pumping down both the chambers are pumped by the two diffusion pumps. The two pumps are interconnected above the throttle valves and can be isolated during deposition using a valve V_1. The stainless steel plate was designed such that the front diffusion pump (diffusion pump 1) can pump the upper chamber and the crucible can be accessed from the top (see Fig.3.2).

The rear diffusion pump is used for pumping the lower chamber only during a deposition. This chamber houses the electron gun unit and has to be kept below a pressure of 10^{-3} torr in order to avoid arc discharges from the beam accelerating electrode. An ion gauge head is also housed in this section.

The upper section contains the substrate holder (see Fig. 3.3) which screws into the water cooled target body with height adjustable relative to the pool (see Fig. 3.1),

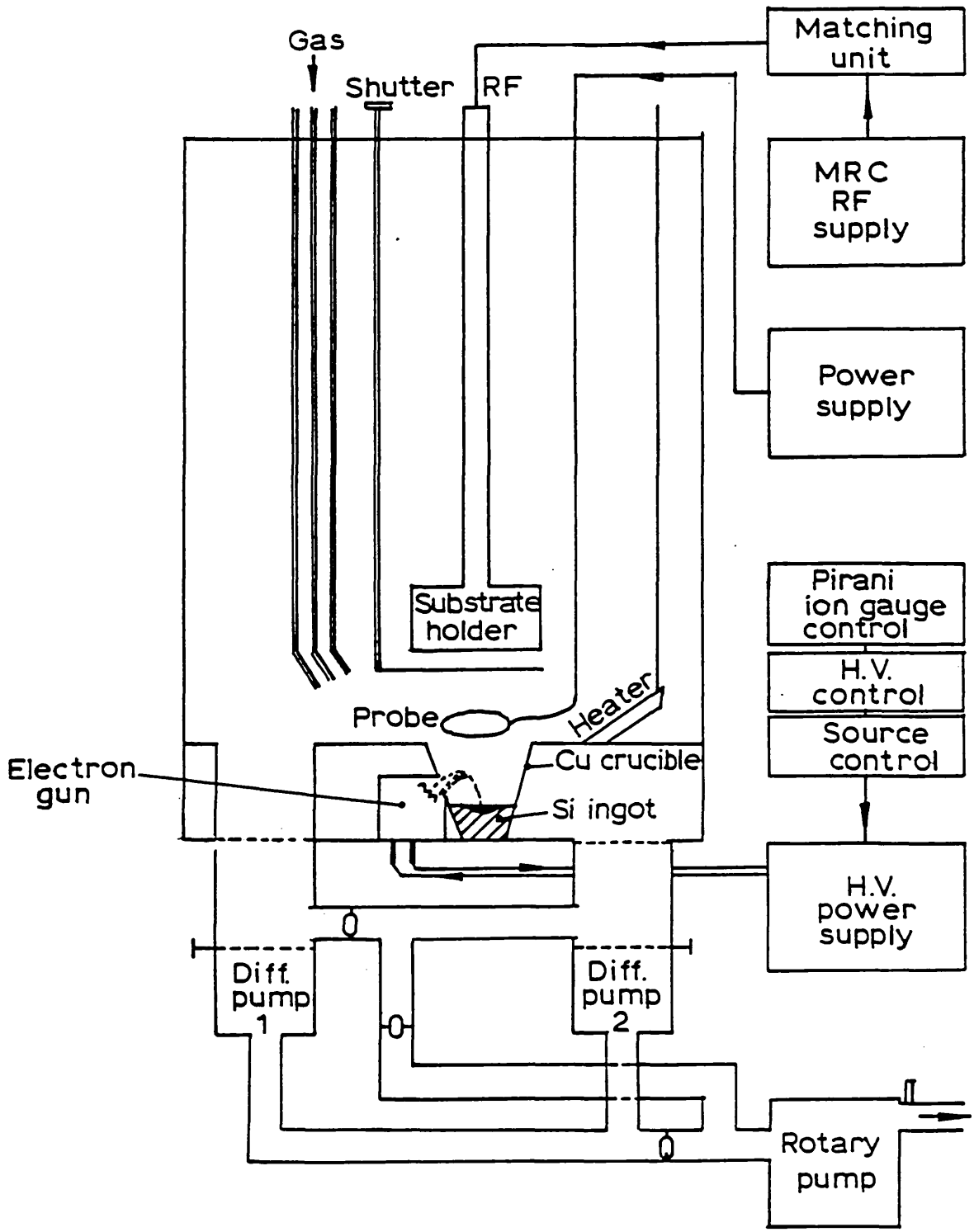

Fig. 3.2 DEPOSITION CHAMBER

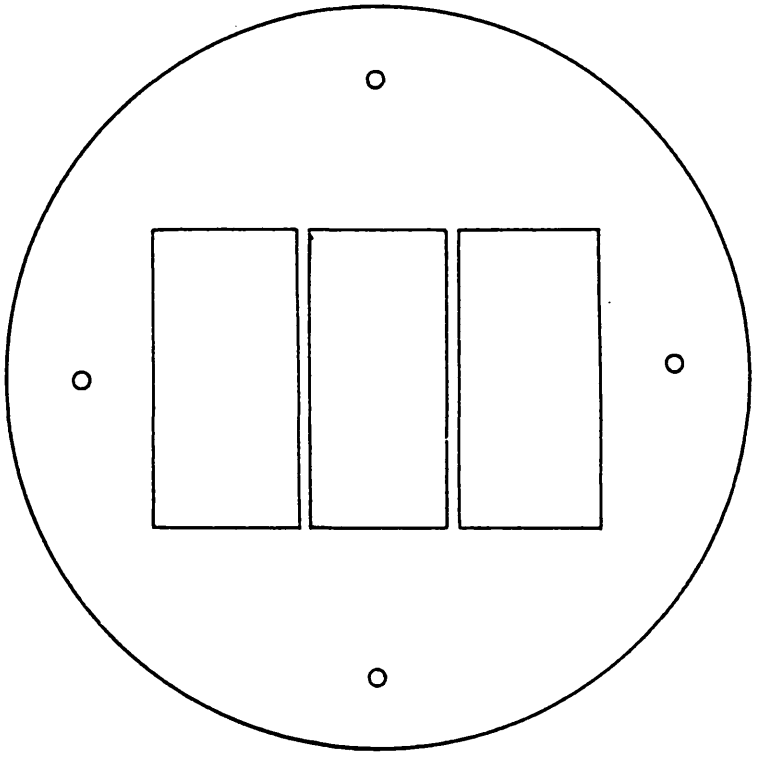

PLAN

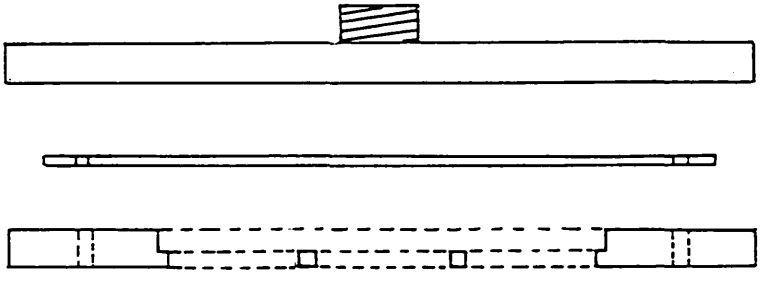

FRONT VIEW
(Exploded)

Fig. 3.3 The substrate holder

conventionally used in sputtering systems. A special substrate holder was constructed using a 5" diameter aluminium plate. This was sectioned into two halves and the bottom half had windows cut into it, each of the size of a Corning 7059 glass (2" x 1") slide. The glass slides are secured using a thin stainless steel backing plate screwing onto the body of the bottom plate. This lower section along with the substrates could now be securely screwed using two stainless steel screws onto the top section. The unit was designed so as to have a gap of about 1 mm between the top half and the bottom half of the substrate holder. This was done so that the substrates could be heated and at the same time the target head could be water cooled to dissipate the r.f. power. This enabled the substrates to be heated up to 400°C without damaging the target head. An earthed dark space shield was used to enclose the target head and the substrate holder. The water pipe and the r.f. lead-through to the target head were also enclosed with an earthed copper pipe.

A rotating shutter in between the copper crucible and the substrate holder was incorporated. The gas inlet pipes were stainless steel $\frac{1}{4}$" diameter tubes and were extended into the reaction zone. Tungsten filament radiant lamps housed in a stainless steel reflector (400 W quartz infrared tubes) were used for heating the substrates. Temperatures of up to 300°C could be maintained during deposition (see Section 3.3). The circular stainless steel probe electrode was situated 6 cm above the molten pool. The probe was secured into a long stainless studding with an

Allen screw; the height of the probe above the ingot thus could be altered. All the feed-throughs were led through the top plate (detachable) of the vacuum chamber. Upper chamber pressure was monitored during deposition using a Pirani gauge head (Pirani 25-S).

A series of experimental depositions revealed a number of equipment weaknesses which were duly corrected. In particular it was found that all non-earthed metal surfaces had to be carefully insulated, to prevent spontaneous, localised discharges to earth, which short out the desired plasma between the low voltage probe and the molten pool. The probe was insulated using ceramic beads at the lower end and the upper end was enclosed in a pyrex tube (see Fig. 3.1). The heater lead was also insulated using ceramic beads.

The chamber door had a pyrex window through which the conditions inside the chamber could be observed. A stainless steel reflector placed conveniently, enabled the position of the electron beam and also the size of the molten pool to be seen clearly and thus could be visually used for adjustment when required.

The r.f. power was supplied from the Materials Research Corporation's 13.59 MHz 1 kW generator. A home-built matching unit was used for matching the generator's 50 ohm output impedance to the target. The matching unit had a built-in voltmeter which enabled the substrate bias to be measured. The matching of the power to the chamber could be done using the forward and reflected power meters

to adjust for 0W reflected power.

The probe voltage was supplied using a 400 V, 3-phase, 10 A current limited power unit. The input voltage to the unit was varied using a 3-phase variac so that the output d.c. voltage could be adjusted. The probe current (i.e. the plasma current) was monitored using an ammeter connected in series with it. A series resistor of 35 Ω between the power supply and the probe helped to stabilize the discharge current and served to limit the current in the event of a catastrophic discharge.

The electron gun was controlled using an Electrotech high voltage and source control unit connected via a 3-phase high voltage power supply unit. The control units are interlocked to various parts of the system for safety reasons. These include the pressure in the chamber, water flow through the copper crucible, the electron gun filament and open and short circuits. The position of the electron beam could be controlled using the source control unit.

The pressure in three parts of the chamber was monitored. A Pirani ion gauge control unit (V.G. Pirani-ion gauge control) was used for monitoring the lower chamber pressure using an ion gauge head. This unit also enabled the backing pressure to be monitored connected to an Edwards PR 10-S Pirani gauge head in the backing line. The upper chamber pressure was monitored using a dual range Pirani 14 control box connected to a PR 25-S gauge head.

The heater voltage was varied using a 10 A variac connected to the heater lamps via an ammeter. The temperature of the substrate was monitored using a Comark 3501 digital thermometer with a chromel-Alumel thermocouple (see section 3.3).

3.3 SUBSTRATE TEMPERATURE

The heater is made up of 3 x 400 W quartz infrared tubes in a parabolic reflector which focus their radiation onto the substrate. They are supplied from a variac and are normally operated in parallel at about 50 V a.c. with a total current of 10 A.

The substrate temperature has been calibrated against heater power and at 500 W the substrate temperature is ~200°C. Once the shutter is opened, radiation from the ingot increases the substrate temperature as shown in Fig. 3.4. It has been found that variation of the substrate temperature between 200°C and 300°C does not significantly alter the quality of the deposited films when substrate bias is used.

3.4 THE PLASMA AND DEPOSITION RATE

The objective is to produce a hydrogen plasma between the probe and the ingot. The plasma density is dependent upon the number and velocity of thermionic electrons emitted from the molten pool and the gas pressure. The number of electrons is determined by the input energy to the ingot which is adjusted to give a particular rate of deposition. For a given rate setting, the efficiency of ionisation is a function of the electron velocity determined by the probe field.

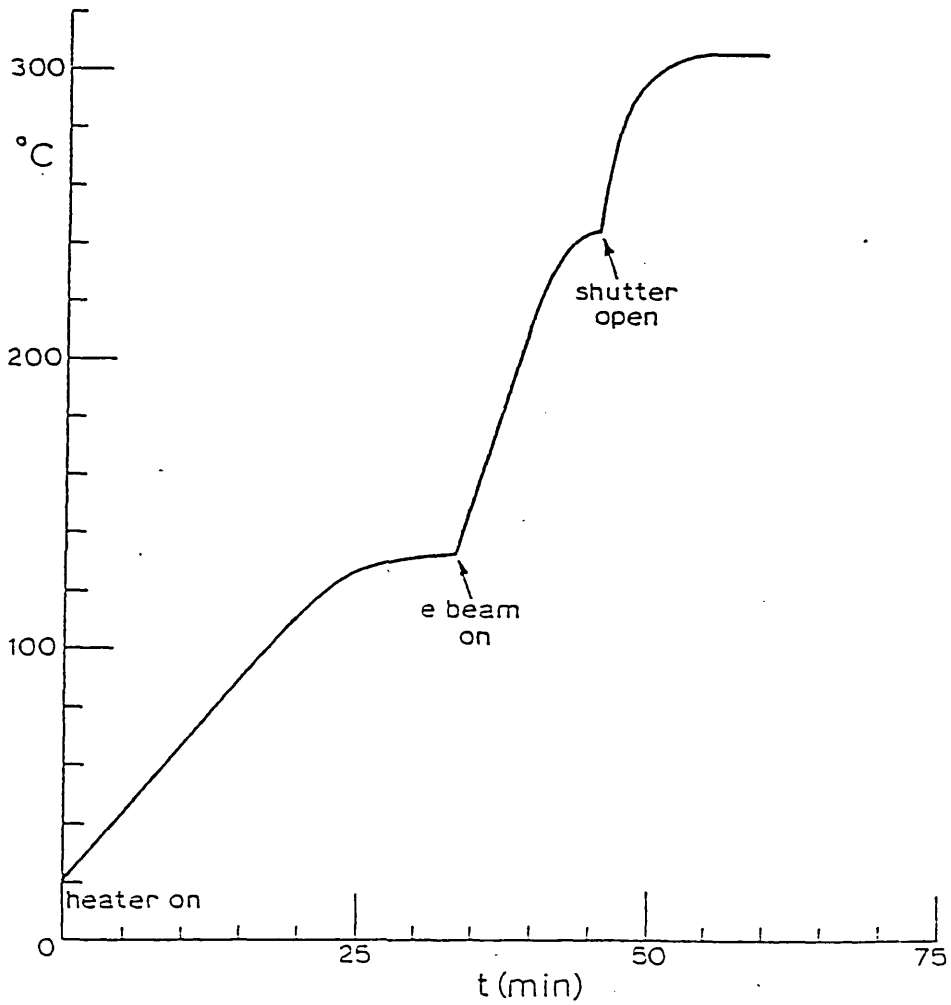

Fig. 3.4 Temperature of substrate against time for 500 W heater

The deposition rate is primarily a function of the electron beam current as determined by the setting of the e-beam power supply. It also depends on the conductivity of the ingot, the height and the area of contact of the ingot with the copper crucible. The gas pressure and the substrate bias also influence the deposition rate.

All the above conditions were investigated during the course of the work for the purpose of optimising the deposition condition and are discussed in Chapter 5.

3.5 THE GAS HANDLING SYSTEM .

A schematic diagram of the gas handling system is shown in Fig. 3.5. Arrows indicate the direction of flow. All the gas pipe work was $\frac{1}{4}$" stainless tubing using connectors, junctions etc. Whitely needle valves (N.V.) and toggle valves (T.V.) were used in the positions shown in the diagram. The system was designed so that hydrogen with phosphine or diborane or argon could be used along with a third gas (e.g. oxygen) if required. A Vacuum General mass flow sensor (FM-361) was used on the hydrogen line and a Vacuum General combined control valve and mass flow sensor (FV6-21) units were used on the dopant gas and oxygen lines. These units were connected in turn to flow/ ratio control units 80-5 and 80-4 (made by Vacuum General) respectively as shown in Fig. 3.5. This system enabled the ratio of dopant gas to be controlled very accurately

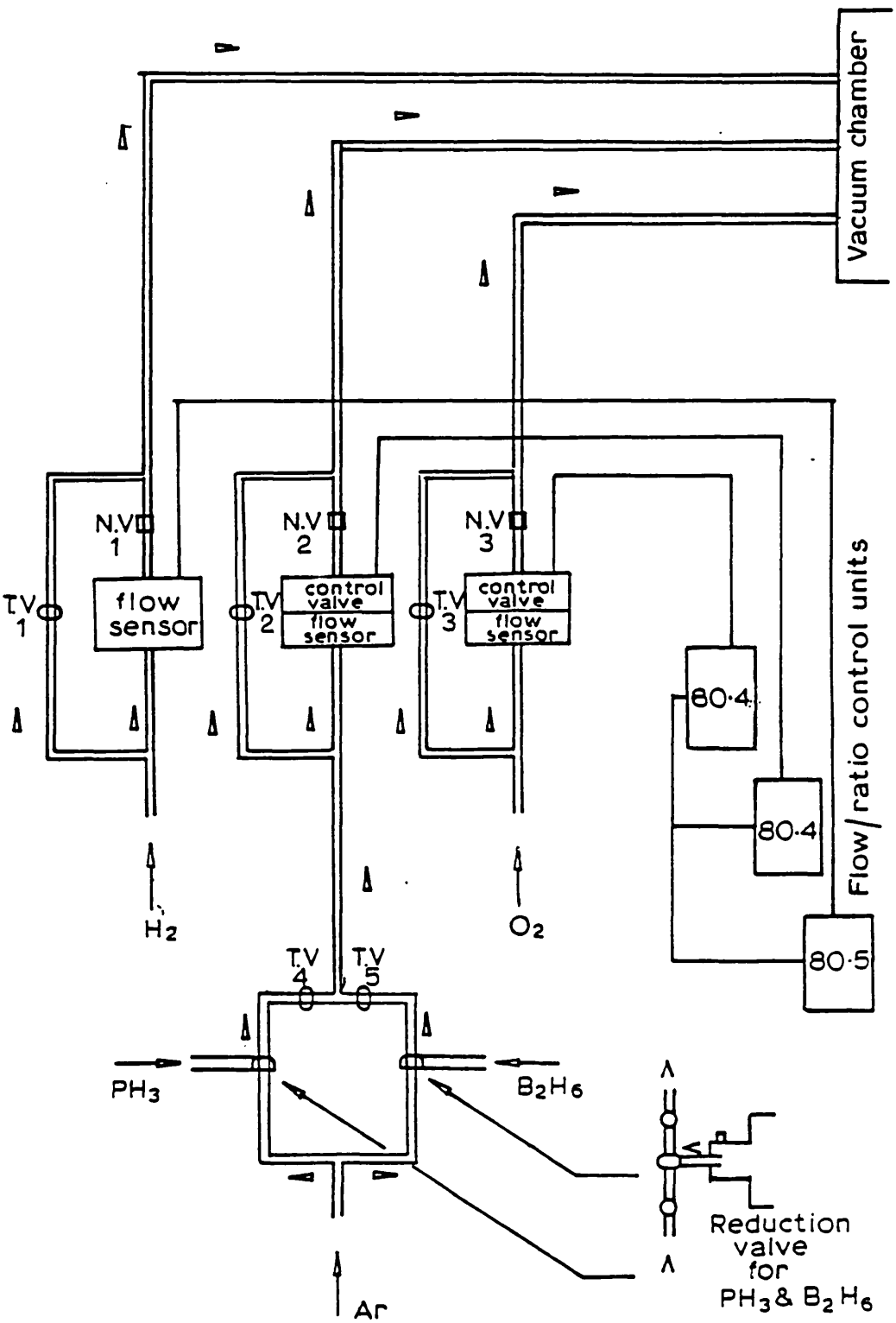

Fig. 3.5 GAS HANDLING SYSTEM

with respect to the hydrogen using the automatic ratio control facilities built into the 80-4 units (the third gas flow could also be auto-ratioed). These units (in particular the 80-4 and 80-5) enabled the handling of any gas simply by adjusting the gas calibration potentiometer; the correction factors were supplied by Vacuum General. All displays are digital and flow is measured in s.c.c.m. The above facility enabled either phosphine or diborane to be used with the same control units. The valves T.V.4 or T.V. 5 could be used to switch to the required gas. Both phosphine and diborane lines could be purged by argon using the circuit shown in the diagram. The positions of T.V.1, T.V.2 and T.V.3 in Fig. 3.5 are parallel to the needle valves (N.V.) N.V.1, N.V.2 and N.V.3,provided by-pass paths around the micrometer and control valves. These allow easy pumping down of the lines right up to the gas cylinder heads and the facility to pump out the system in the event of blockage of a control valve.

When using phosphine or diborane the exhaust from the rotary pump was diluted with dry nitrogen at a pressure of 15 lb/in^2. This mixture was further diluted and streamed away from the building using a stream of compressed air contained in an outer tube, concentric with the gas exhaust tube. It was essential to have a leak-free system starting from the gas bottles to the end of the exhaust outlet for a safe operation in view of the hazardous and toxic nature of the gases used.

3.6 PREPARATION OF SUBSTRATES

All a-Si:H films for electrical and optical measurements (visible spectrum), were deposited on Corning 7059 glass slides (5 cm x 2.5 cm x 0.1 cm). Initially aluminium coated 7059 slides were also used for infrared measurements (specular reflection), but on comparing measurements carried out on aluminium coated microscope glass slides no apparent differences were found and henceforth the less expensive microscope glass slides coated with aluminium were used. The 7059 glass slides are high resistivity and are sodium free; these features are essential for electrical measurements.

The cleanliness of the glass slides was found to be of great importance with regard to adhesion of the film to the glass, the mechanical properties of the film, freedom from pinholes and from contamination.

To ensure the cleanliness of the glass substrates, the following procedures were adhered to:

(1) The glass was put in a pyrex beaker containing 10% teepol and 90% distilled water. This was transferred to an ultrasonic bath for 10 mins.

(2) The glass was then transferred to another beaker containing distilled water and put in the ultrasonic bath for 5 mins.

(3) The next step was to clean the slides in a mild etchant solution comprising 35% nitric acid,

60% distilled water, 2% hydrofluoric acid and 3% teepol. The slide was dipped in this solution contained in a polythene beaker using a pair of polythene tweezers for 5 secs only, and was then transferred to a fourth beaker containing distilled water.

(4) This fourth beaker was then put in the ultrasonic bath for a further 5 mins.

(5) Next stage was to clean the slide ultrasonically in isopropyl alcohol for a further 5 mins.

(6) Finally the slide was transferred to a "Soxlet" and refluxed in isopropyl alcohol vapour for 30 mins and allowed to dry in the Soxlet.

(7) The slide was then transferred to a new petri dish and stored in a dessicator.

All the above operations were carried out in a lamina-flow cabinet. In most cases the glass slides were mounted in the substrate holder and transferred to the vacuum chamber on the same day or the following day. If and when required the slide was coated with aluminium to a thickness of about 0.2 micron to ensure ~100% reflectance from it for infrared absorption measurements.

3.7 DEPOSITION PROCEDURE (Refer to Figs. 3.2 and 3.5)

3.7.1 Deposition of an Intrinsic a-Si:H Film

The following steps are typical of an intrinsic film deposition:

(1) The substrates are mounted in the substrate holder and transferred to the vacuum chamber in a glass petri dish. They are mounted onto a target head, the dark space shield is put in position and the viewing reflector is placed in the correct position.

(2) The chamber is pumped overnight to a background pressure of ~4 x 10^{-6} torr, as far as the hydrogen cylinder, with T.V.1, N.V.1, T.V.2, N.V.2, T.V.3 and N.V.3 open. All other valves and reduction valves are closed.

(3) The flowmeters are switched on and allowed to stabilize for half an hour. All valves are then closed. The hydrogen valve is opened and N.V.1 is adjusted to allow about 30 s.c.c.m. of hydrogen to flow through the system. Water cooling for the target head is turned on, the heater is set to the required heating current (10 A) and is left on for half an hour before deposition is started. The hydrogen at this stage is used for purging the system and also to provide a reducing atmosphere to prevent oxidation of the ingot as it is heated up.

(4) The water supply to copper crucible is turned on and the throttle valve connecting diffusion pump 1 and diffusion pump 2 is closed. The electron gun power supply is energised and the ingot is slowly heated up to the required level with the shutter remaining closed. When the full power required is reached, the hydrogen flow is increased to about 60 s.c.c.m., keeping note of the pressures shown by the three vacuum gauges. Typical electron beam settings are accelerating voltage 7.2 kV, filament current .22 A (corresponding to the dial on the filament current control being set at 250).

(5) Using a baffle valve on diffusion pump 1 the pressure in the upper chamber is increased to about 2.2 mb. The lower chamber pressure should be less than 1.5×10^{-3} torr with the backing pressure less than 0.2 torr.

(6) The probe voltage is switched on and adjusted to the required value of about 290 V. At this point plasma ignites and a plasma current is recorded.

(7) The r.f. bias is switched on and set to ~300 W r.f. power; the matching unit tuning is adjusted for zero reflected power. (After first setting this does not usually require readjustment in successive deposition runs.)

(8) Conditions are allowed to stabilize for about 1 min. and the shutter is then opened, the r.f. bias being readjusted at the same time to the target value of bias voltage. Deposition is usually continued for 5 mins.

(9) At the end of the deposition time the shutter is closed. Probe voltage, r.f. bias, heater and electron beam power are all switched off. Water cooling on the copper crucible and hydrogen flow are kept running for half an hour, with hydrogen flow reduced to 30 s.c.c.m. The baffle valve on the diffusion pump is fully opened and the throttle valve connecting the two diffusion pumps is also opened.

(10) When the chamber is cool, water cooling and gas are turned off, and the chamber may be opened for removal of the substrates.

3.7.2 Preparation of n-type a-Si:H

Steps (1) to (7) inclusive are the same as above

(8) The r.f. power and the probe voltage are switched off. The hydrogen flow is reduced to the desired value. Nitrogen flow into the exhaust side of the rotary pump is introduced at a pressure of 15 lb/in^2.

(9) The phosphine cylinder valve is opened and closed immediately. This gives ample gas supply for the 5 min. deposition.

(10) The valves T.V.4 and N.V.2 and the outgoing valve of the reduction valve unit on the phosphine cylinder is opened. Using the reduction valve, the gas pressure going into the vacuum chamber is increased to 15 lb/in^2. This brings the phosphine flow up to the combined control valve and flow sensor unit.

(11) Using the flow control dial, the required phosphine flow is introduced into the vacuum chamber.

(12) The pressure in the vacuum chamber is readjusted to give an upper chamber pressure of $\sim 2.2 \times 10^{-2}$ mb.

Steps (13) to (15) inclusive are the same as steps (6) to (8) in section 3.7.1.

(16) At the end of the deposition time the shutter is closed. Probe voltage, r.f. bias, heater and electron beam power are all switched off. Water cooling on the copper crucible is kept running for half an hour. The hydrogen flow is cut off using N.V.1. The diffusion pump 1 baffle valve is opened fully and the throttle valve connecting diffusion pump 1 and diffusion pump 2 is opened.

(17) The phosphine flow is increased to ~60 s.c.c.m. for rapid evacuation of the excess gas in the system.

(18) When the flow indicated is zero, the toggle valve T.V.2 is opened and the gas line is pumped down right up to the phosphine cylinder to a pressure ~8 x 10^{-6} torr.

(19) The nitrogen flow is switched off. All the valves on the gas lines are closed.

(20) Hydrogen flow is introduced at a flow rate of 30 s.c.c.m. for half an hour.

(21) When the chamber is cool, the phosphine line and the vacuum chamber is purged with argon for fifteen mins.

(22) The chamber is opened for the removal of the substrates.

3.7.3 Preparation of p-type a-Si:H

The procedure is exactly the same as in the case for n-type a-Si:H deposition. The phosphine is substituted by diborane (see Fig. 3.5). The valve T.V.4 is kept closed and T.V.5 is opened during deposition.

3.7.4 Solid-State Doping Using Antimony

The required amount of antimony (few grams) is placed around the edge of the cold silicon ingot and this is melted into the silicon on heating up with the electron beam.

The procedure for deposition is exactly the same as for intrinsic a-Si:H.

CHAPTER 4

OPTICAL MEASUREMENTS

4.1 INFRARED SPECTRA OF ARE FILMS

4.1.1 Introduction

Pure elemental amorphous silicon is impregnated with dangling bonds which can be detected using electron spin resonance (ESR) [1]. These dangling bonds have a profound effect on the physical properties of semiconductors, since they give rise to high density of localised gap states, as seen in Chapter 2. These states influence the optical absorption process as well as the electrical conduction mechanism. ESR measurements have shown [2] that elemental amorphous silicon prepared for example by evaporation has a dangling bond density of about 10^{20} per cm^3. The density of dangling bonds deduced from study of hopping conductivity in evaporated amorphous silicon is of the same order of magnitude [3]. These dangling bonds are associated with multi-vacancies. In the basic disordered tetrahedral network each silicon atom can have up to four unpaired bonds. It is now believed that in glow discharge of silane [4] and sputtered silicon in a hydrogen atmosphere [5], these unpaired or dangling bonds are passivated by hydrogen to a considerable extent. This view is confirmed by ESR measurements on such materials in which values of less than 10^{16} unpaired spins per cm^3 are observed [6]. Hydrogen bonding lowers the electrically active states associated with the dangling bonds to the valence band [7]. In fact

hydrogen concentration in g.d. a-Si:H is much higher than the number of available dangling bonds. Also glow discharge specimens may contain up to 25 atomic percent of hydrogen which is about 10^3 to 10^4 times the density of the dangling bonds. Moustakas et al [8], in their work on the photoconductivity of sputtered a-Si:H, have reported a sharp rise in the photoconductivity of their material with the initial addition of hydrogen. This they attributed to the saturation of the dangling bonds. They further reported that the photoconductivity dropped sharply after the addition of more than about six atomic percent of hydrogen. They suggested that the additional hydrogen cause an increase of 'tail' states near E_c.

Spear and LeComber [9] take the view that hydrogen concentrations of ~1 atomic percent should be ideal for glow discharge a-Si:H. This concentration would be enough to reduce the density of the "hard" states. The plasma conditions and deposition control need to be improved for the minimum hydrogen incorporation and for lowering of the "soft" state densities (see Appendix 2 for "hard" and "soft" state definitions).

Infrared (IR) absorption measurements on a-Si:H films provide a means of studying the vibrational spectra of the silicon and hydrogen bonds. They can also provide an estimate of the atomic percentage of hydrogen incorporated in the film, although the accuracy claimed for this estimate is not better than a factor of about 2 to 3. These spectra have been taken as a matter of routine for the ARE films as a means of studying their structure, hydrogen and oxygen content.

4.1.2 Infrared Absorption

Each deposition included a film deposited on Aℓ-coated glass, which was used as a specimen for infrared absorption measurements. These were carried out by reflection at 45° in Perkin-Elmer 580B Grating Infrared Spectrometer with Data Station.

The absorption coefficient was calculated in the following way, with reference to Fig. 4.1.

I_{Si}/I_o is the fractional transmitted intensity compared to that of an aluminium coated slide placed in the reference beam.

The absorption coefficient for silicon of thickness d is given by

$$\frac{I_{Si}}{I_o} = \exp(-\alpha_{Si}d) \tag{4.1}$$

For a silicon hydrogen bond

$$\frac{I_{Si+SiH}}{I_o} = \exp(-\alpha_{Si}d)\ \exp(-\alpha_{SiH}d) \tag{4.2}$$

$$\frac{I_{Si}}{I_o} - \frac{I_{Si+SiH}}{I_o} = \Delta\left(\frac{I}{I_o}\right) \tag{4.3}$$

From equations (4.1), (4.2) and (4.3)

$$\Delta\left(\frac{I}{I_o}\right) = \exp(-\alpha_{Si}d)\ (1-\exp(-\alpha_{SiH}d)) \tag{4.4}$$

Rearranging (4.4) we get

$$\exp(-\alpha_{SiH}d) = 1 - \frac{\Delta\left(\frac{I}{I_o}\right)}{\exp(-\alpha_{Si}d)} \tag{4.5}$$

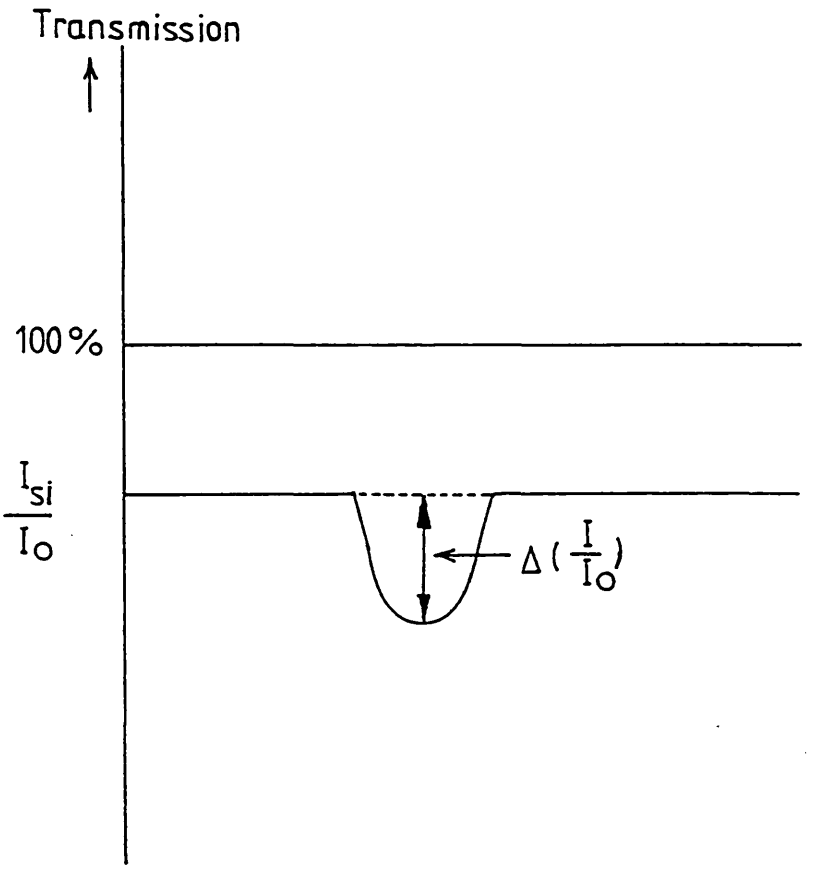

Fig. 4.1

Group	Mode	Frequency (cm^{-1})	A(10^{19} cm^{-1})	Ref.
Si-H	Stretch	2000 2085	2.2 17	(a)
$Si-H_2$	Symmetric stretch Asymmetric stretch	2100 2090	9.1 9.1	(a)
$Si-H_3$	Symmetric stretch) Asymmetric stretch)	2140	-	(a)
$Si-H_2$	Symmetric bend	875	2.0	(a)
$(Si-H_2)_n$	Symmetric bend	840, 890	2.0*	(a)
$Si-H_3$	Symmetric bend	860	2.0	(a)
$Si-H_3$	Asymmetric bend	910	2.0	(a)
SiH	Wag	640	1.6	(a)
SiH_2	Roll, wag	640	1.6	(a)
HSi_3O		2100	-	(b)
HSi_2O_2		2190	-	(b)
$HSiO_3$		2240	-	(b)
Si-O-Si	Stretch	980	-	(c)
	Orthogonal vibrations	500, 660	-	(c)
Si-H, .) Si-O-Si)	Coupled modes	630, 780	-	(c)
SiO_2		1000 - 1250	-	

*For samples with the 890 peak twice as strong as the 840 one.

A decrease if the relative strength of the 840 peak increases.

Table.4.1

From (4.1) and (4.5)

$$-\alpha_{SiH}d = \ln\left(1 - \frac{\Delta(\frac{I}{I_o})}{(\frac{I_{Si}}{I_o})}\right) \qquad (4.6)$$

The path length for the beam at 45° angle of incidence, approximated to 2d from Snell's law with the refractive index of amorphous silicon taken to be $\sqrt{11}$.

The peaks in the IR spectrum were interpreted by reference to Cardona [10(a)], J. Knights et al [11(b)] and Lucovsky et al [12(c)] whose results are summarised in Table 4.1 in which the superscripts (a), (b) and (c) indicate the above references. The number of hydrogen atoms per unit volume, N_H, was estimated from

$$N_H = A \int_{peak} \frac{\alpha}{\omega} \, d\omega \qquad (4.7)$$

where α is the absorption coefficient in cm^{-1}, ω is the wavenumber in cm^{-1} and A is a constant determined by the oscillator strength of the bond being considered. A is inversely proportional to the oscillator strength and is given in Table 4.1.

It should be emphasised that the values for the oscillator strengths given in Table 4.1 have been derived from the study of glow discharge films and the accuracy as mentioned earlier is no more than a factor of 2 to 3. In addition to the peaks associated with silicon hydrogen bonds, there are peaks associated with oxygen and these are also included in Table 4.1.

As discussed earlier, infrared analysis of a-Si:H is an important tool in the characterisation of these films;

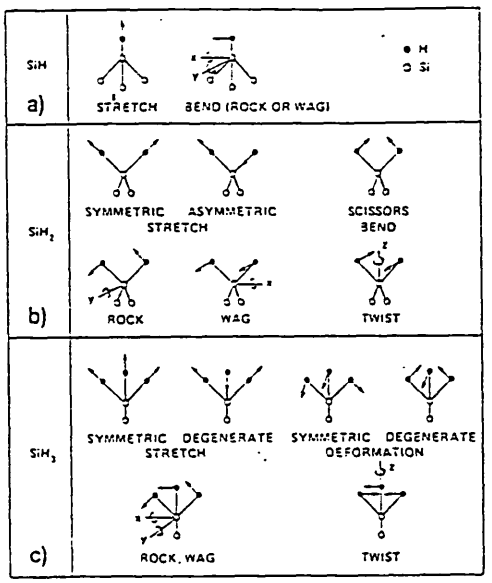

Fig. 4.2.1

a–c. Atomic displacements of H atoms in local and resonance mode vibrations in (a) SiH groups (b) SiH_2 groups and (c) SiH_3 groups

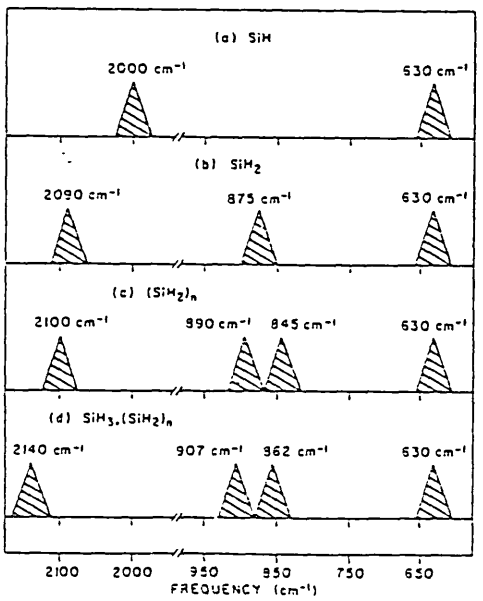

Fig. 4.2.2

a–d. Schematic representation of ir data for a-Si:H alloys. The absorptions are organized into groups that have been assigned to different local bonding configurations. The most recent interpretations favor (d) being attributed to polysilane. rather than SiH_3

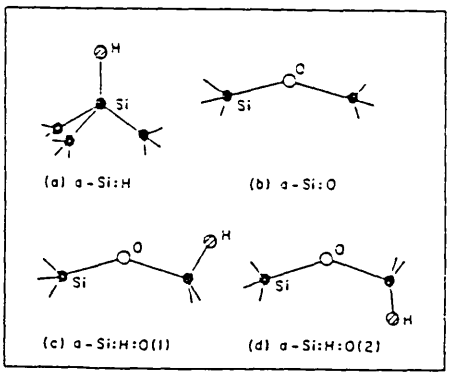

Fig. 4.2.3

a–d. Local bonding geometries: (a) isolated SiH site in a-Si:H; (b) isolated Si–O–Si group in a-Si:O; (c, d) two bonding arrangements in which H and O atoms are bonded to a common site as in a-Si:H:O. The SiH bond lies in the plane of the Si–O–Si triad in each arrangement; in (c) the O and H atoms are in CIS conformation and in (d) they are in a TRANS conformation

Fig. 4.2.1,2,3 shows the schematic representation of the various modes of oscillations observed for silicon, hydrogen and oxygen bonds.
(After G. Lucovsky and W.B. Pollard, ref. 18, ch. 7)

not only can it be used to make an estimate of the hydrogen content in the film, but it can also be used in the identification and detection of monohydride, multi-hydride and oxide bonding sites. This can be particularly useful in trying to relate the properties of the deposited film to the deposition conditions. However, it must be borne in mind that IR properties alone do not characterise the quality of the film; electrical and optical measurements are also necessary.

In the following sections the IR spectra of films prepared by ARE are discussed in relation to their preparation conditions.

4.1.3 Zero Bias

In Fig. 4.3 is shown the spectrum for a film prepared at a deposition rate of 0.095 μm/min at zero substrate bias. The spectrum shows a large peak at 2100 cm^{-1} corrsponding to $(Si-H_2)_n$ symmetric stretch combined with doublet peaks at 840 cm^{-1} and 890 cm^{-1}, the symmetric bend modes. The peak at 780 cm^{-1} corresponds to the Si-O-Si and Si:H coupled modes, a component of which can be found at 630 cm^{-1}. There is a broad but small peak at 2000 cm^{-1} corresponding to the Si-H stretch mode. The peak at (630-640) cm^{-1} is due to the combined contribution of the wag modes of Si:H, the coupled modes of Si-O-Si and Si-H and to the wag modes of the individual $Si-H_2$ units in the $(Si-H_2)_n$ chain. The peak at 500 cm^{-1} is attributed to the Si-Si bonds. The hydrogen density calculated from the (630-640) cm^{-1} peak was 2.35×10^{21} cm^{-1}, corresponding to an estimated value for the percentage incorporation of hydrogen of 5.23%.

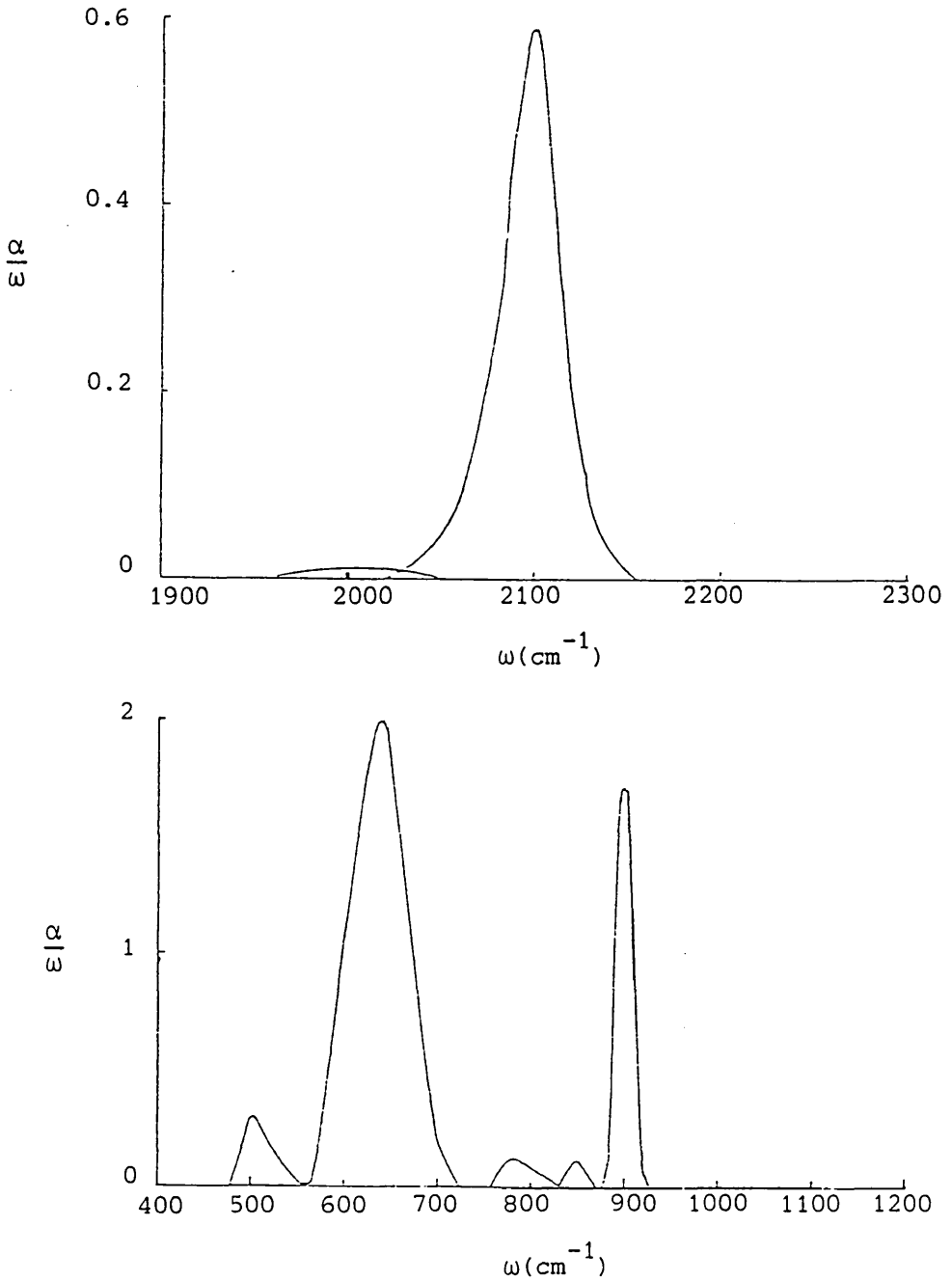

Fig. 4.3 IR absorption spectrum for a film prepared with zero substrate bias.

This type of film showed very poor electrical qualities including very poor photoconductivity. This is expected for amorphous silicon films containing polysilane chains. The electrical and photoconductivity properties are discussed in Chapter 5.

4.1.4 Positive D.C. Bias

Since the probe electrode is held at a positive potential, when the substrate is earthed, there will be an accelerating field for positive ions towards the substrate, which is therefore still subject to ion bombardment and charging even in the absence of an applied bias.

To investigate the effect of eliminating this process the substrate was self-biassed to a positive potential by connecting it to earth through a high resistance (a digital voltmeter). Under typical deposition conditions, with probe electrode at +400V, the bias developed was +350V. This corresponds to a current of 10 μA through the substrate and the digital voltmeter whose resistance was 10^7 Ω.

In Fig. 4.4 is shown the spectrum for a film with a d.c. self bias of +350V. The film thickness was 0.24 μm. The spectrum shows most strikingly a relatively large peak at 2100 cm^{-1} attributed to the stretch mode of $Si-H_2$ species with a suppressed wag mode at 640 cm^{-1}, and a totally inhibited bend mode. These phenomena have been observed in some sputtered amorphous silicon films (Shanks et al [13], Paul [14]). This is ascribed to the formation of $Si-H_2$ bonds on the surfaces of internal voids and on the external film surface. It is assumed that all the bonds on the internal

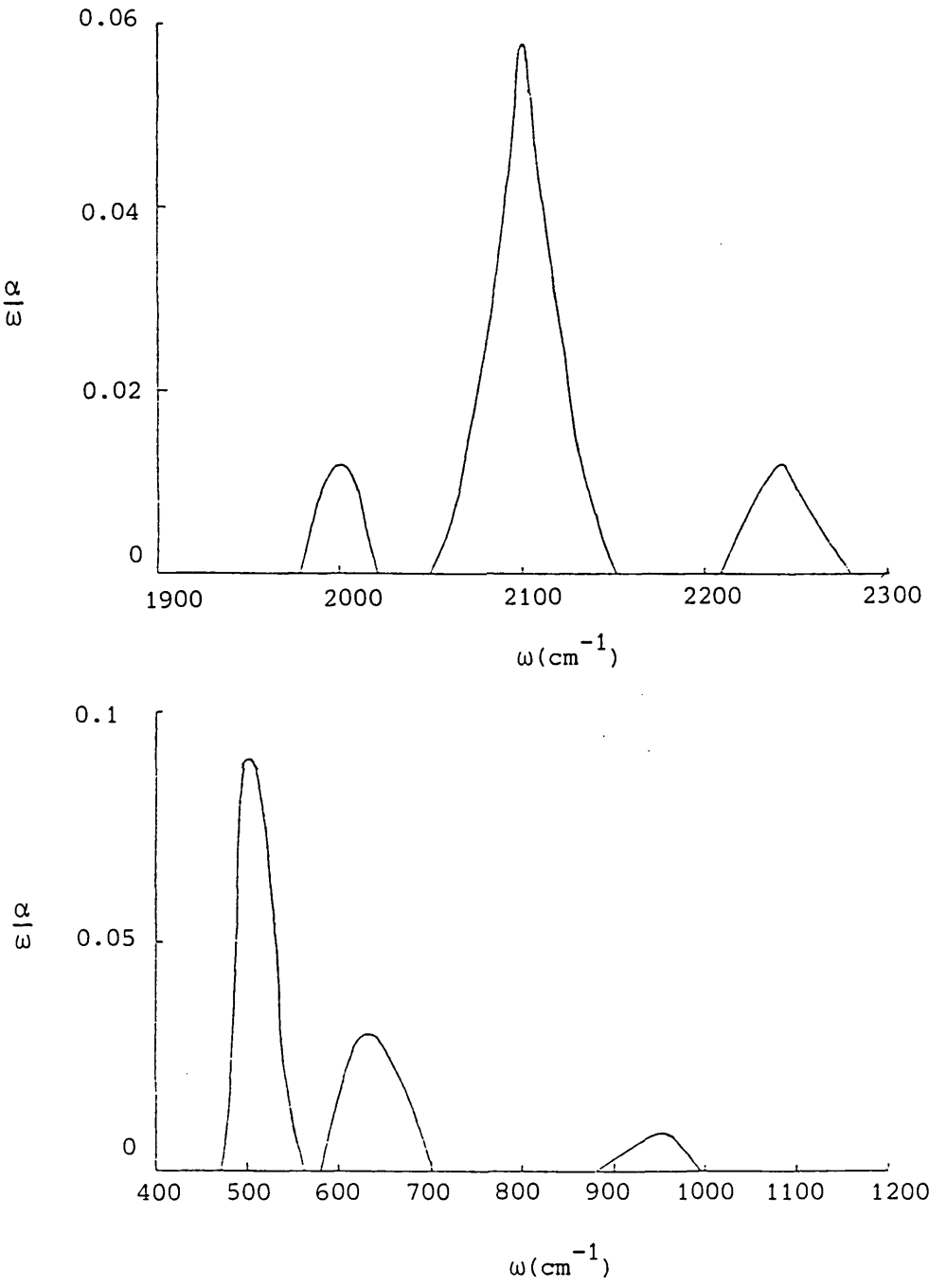

Fig. 4.4 IR absorption spectrum for a film prepared with D.C. self bias of +350 volts.

surfaces are saturated with hydrogen atoms which are, therefore, packed closely enough for individual bending of the bonds to be suppressed by nearest neighbour interaction.

The hydrogen incorporation is 3.52×10^{19} atoms/cm^3 corresponding to a percentage estimation of 0.078 percent from the wag mode whilst the stretch mode gives a hydrogen content of 0.46%,which is considerably lower than was the case with the earthed substrate. The peak at 2250 cm^{-1} is due to $HSiO_3$. In the presence of a peak at ~980 cm^{-1} (stretch mode of Si-O-Si), it can be deduced that the oxidation is not only at the surface but includes Si-O-Si bridging structures in internal voids. However, the quantity of oxygen atoms present in the film is evidently small in view of the low intensity of these peaks compared to the $Si-H_2$ peaks. There is a small peak at 2000 cm^{-1} due to the stretch mode of the Si-H bonds and quite a sharp Si-Si peak at 500 cm^{-1}. The photoconductivity in these films (< 0.3 μ) was better than the zero bias films but did not show much promise for device applications.

4.1.5 Negative D.C. Bias

To investigate further the effects of ion bombardment of the growing film, a negative d.c. bias was applied to the substrate.

In Fig. 4.5 is shown the spectrum for a film prepared at a deposition rate of 0.075 μm/min with a d.c. bias of -2000V. The film was of thickness 0.75 μm. This type of film showed stretch modes at 2000 cm^{-1} and 2100 cm^{-1} associated with a wag mode at 640 cm^{-1}. The peak at

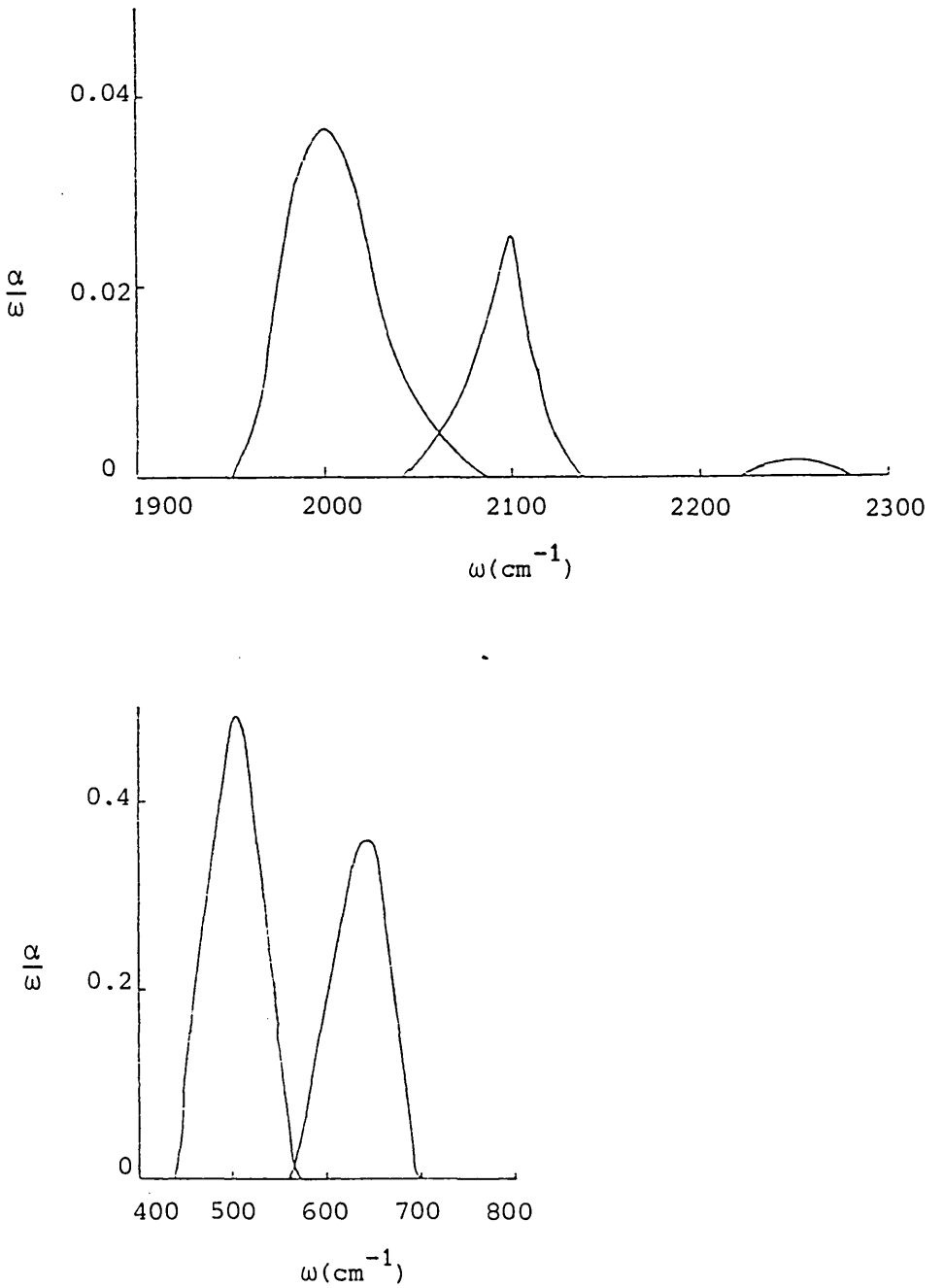

Fig. 4.5 IR absorption spectrum for a film prepared with a bias of -200 volts D.C.

2240 cm^{-1} is due to $HSiO_3$. There is a large peak due to Si-Si bends at 500 cm^{-1}.

As in the case of the positively biassed films, the SiH_2 peak at 2100 has no associated bend mode at 875 cm^{-1}. The hydrogen concentration estimated was 4.24 x 10^{20} cm^{-3} from the wag mode correspond to 0.94% hydrogen. The photoconductivity was very low and the conductivity versus 1/temperature plot showed $T^{-\frac{1}{4}}$ behaviour, indicating hopping transport and implying a very large density of gap states. It is expected that the film will have a non-uniform hydrogen content and structure since, for the initial deposition, the negative bias will attract positive ions from the plasma. As the film builds up and becomes an insulating layer the positive charge due to the positive ions cannot leak away through the film. Thus the film surface will gradually increase in potential from -2000V towards zero and the deposition conditions on the substrate will change.

4.1.6 Negative RF Bias

The RF power is fed to the substrate holder via a series capacitor. This will hold charge collected from the plasma as the applied RF voltage varies between positive and negative values. When the substrate swings positive it will collect electrons from the plasma and the capacitor will charge up negatively. On the negative half cycle positive ions are collected and the capacitor will charge positively. However, because the mass of an ion is many thousand times the mass of the electron, its drift velocity in the RF field is much lower than the electron velocity. As a result the acquired positive charge during the negative RF half cycle is much smaller than the acquired negative charge during the positive half cycle. The net

effect is a negative mean potential on the substrate. An insulating film merely acts like a series capacitor in the system and so the negative bias is maintained as the film grows.

It is deduced that poor electrical and photoconductive properties can arise from non-uniformity of structure and hydrogen content through the film thickness. These poor properties may also be associated with the presence of microvoids saturated on their internal surfaces with $Si-H_2$ bonds.

To eliminate the charging up effect and hence produce a uniform film, RF negative biassing was adopted.

The effects of applied negative RF bias were investigated together with annealing studies on the films. In general the annealing treatment was to heat the film in a vacuum of 10^{-5} torr to 200°C and maintain it at that temperature for 3 hours. Exceptions to this treatment are noted below.

In Fig. 4.6 is shown the spectrum for a film prepared at a deposition rate of 0.05 μm/min with a bias of -200V. In the as-prepared film (solid line) the most striking feature is again the large peak at 2100 cm^{-1}, whose area corresponds to 2×10^{21} H atoms/cm^3. This is associated with only a small peak at 640 cm^{-1}, the area of which corresponds to 1.2×10^{20} H atoms/cm^3, and no peak at 875 cm^{-1}. This is exactly as was found for the d.c. bias films (both positive and negative), in which the bend mode is totally suppressed. As explained in section 4.1.4, this is caused by saturation of all the bonds on the internal

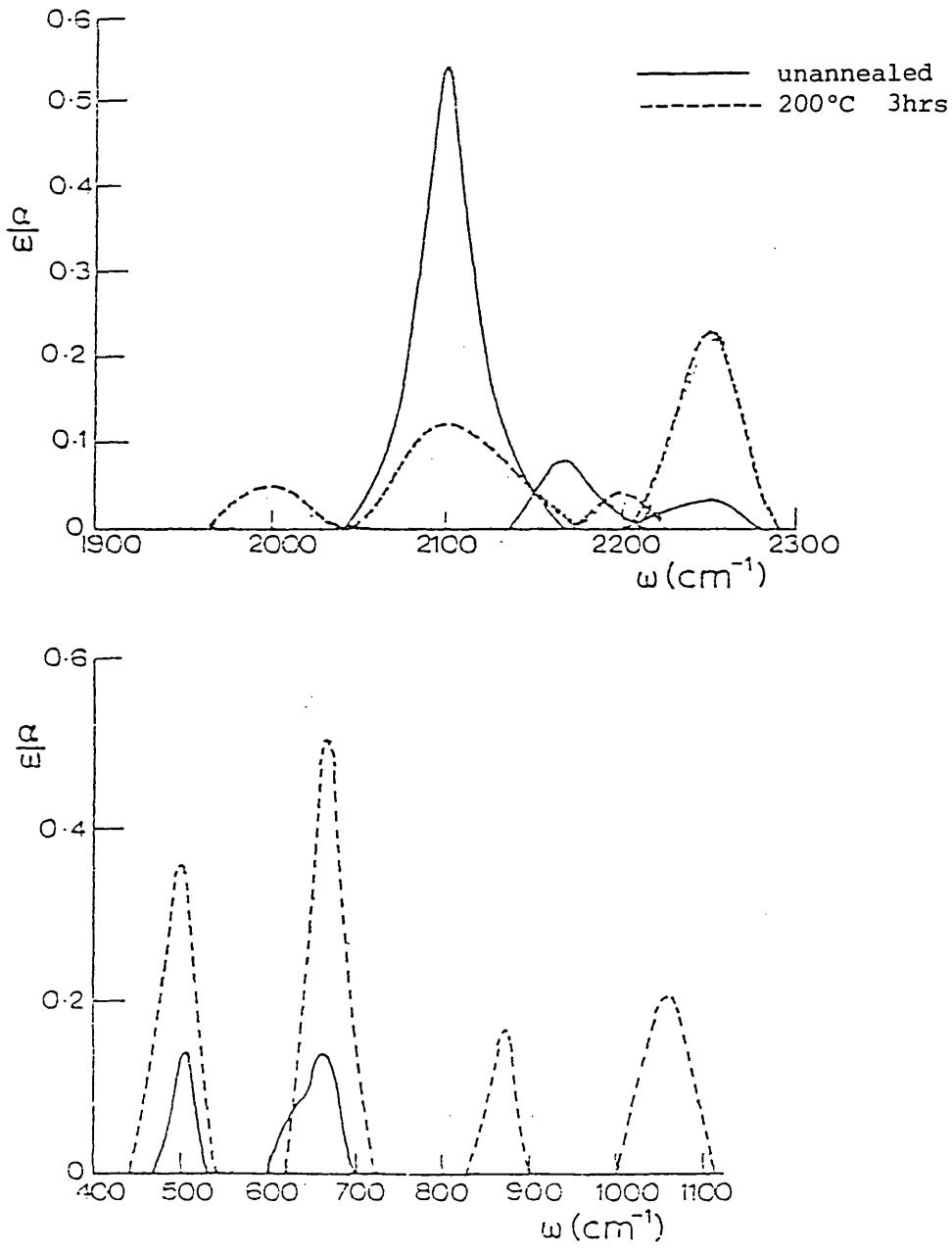

Fig. 4.6 IR absorption spectrum for a film prepared with a bias of -200 volts.

surface and the formation of $Si-H_2$ bonds on the film surface. The closely packed hydrogen atoms suppress the bending modes. It is also suggested that, since due to the bias the film surface is being continually bombarded with protons, the surface of the film at the end of deposition is also saturated with hydrogen.

The peaks at 2180 and 2250 cm^{-1} are interpreted as being due to HSi_2O_2 and $HSiO_3$ respectively and it is likely that the 2100 peak includes a proportion of HSi_3O. The absence of peaks at 780 and 980 show that oxygen is not present as a bridging atom to any extent and so the oxygen is assumed to be mainly on the film surface. The peak at 500 cm^{-1} is attributed to Si-Si bonds.

After annealing at 200°C the spectrum changes considerably with peaks appearing at 2000, 875 and 1050. The 2100 peak is reduced whilst the peaks at 500, 640 and 2250 are increased. These changes are consistent with further oxidation of the film. The increase in the hydrogen wag mode at 640 and the emergence of the SiH_2 bend mode at 875 suggest that the void surfaces are no longer saturated with hydrogen and the appearance of the 2000 cm^{-1} mode indicates that some hydrogen groups have been reduced to Si:H from $Si:H_2$. The increase in the 2750 peak implies an increase in $HSiO_3$ whilst the reduction of the 2180 peak suggests a decrease in HSi_2O_2. These changes are consistent with the substitution of oxygen for some surface hydrogen. The continued absence of the 780 and 980 peaks indicates that no bridging Si-O-Si groups have been formed. It appears probable that the oxidation has occurred mainly on the film

surface. The increase in the 500 cm^{-1} peak would be consistent with an increased amount of tetrahedral co-ordination amongst the silicon atoms. The combined areas of the 2000 and 2100 peaks gives a hydrogen content of 6.5×10^{20} atoms/cm^3, whilst the 640 cm^{-1} wag mode peak gives 4.7×10^{20} atoms/cm^3. Apparently, therefore, the majority of the void surfaces are no longer saturated with hydrogen and the wag mode is able to develop together with the bend mode.

In Fig. 4.7 is shown the spectrum for a film deposited at the higher rate of 0.18 μ/cm^2 with an increased bias of -300V. The as-deposited spectrum shows a single stretch mode peak at 2125 cm^{-1}, which may be due to admixture of SiH_3, the usual wag mode 640 cm^{-1} peak, but also peaks at 780 cm^{-1} and 900 cm^{-1}. The hydrogen density from the 2125 peak is 1.9×10^{21}, whilst from the 640 peak it is 7.1×10^{20}. The peak at 900 is near enough to 875 to be identified as the SiH_2 bend mode, or may be a mixture of SiH_2 and SiH_3 bend modes. Thus, in this case we assume that the void surfaces are not completely saturated with hydrogen. The appearance of the 780 peak indicates the presence of Si-O-Si:H groups of Fig. 4.2.3(c,d), which may be due to some of the internal surface hydrogen atoms. The stretching mode of Si-O-Si is not observed.

On annealing at 200°C the stretch mode peak moves to 2110 cm^{-1} and is reduced and a 2000 peak appears, as in the previous case. The total hydrogen estimated from these two peaks is 5.6×10^{20} atoms/cc. On the other hand, the

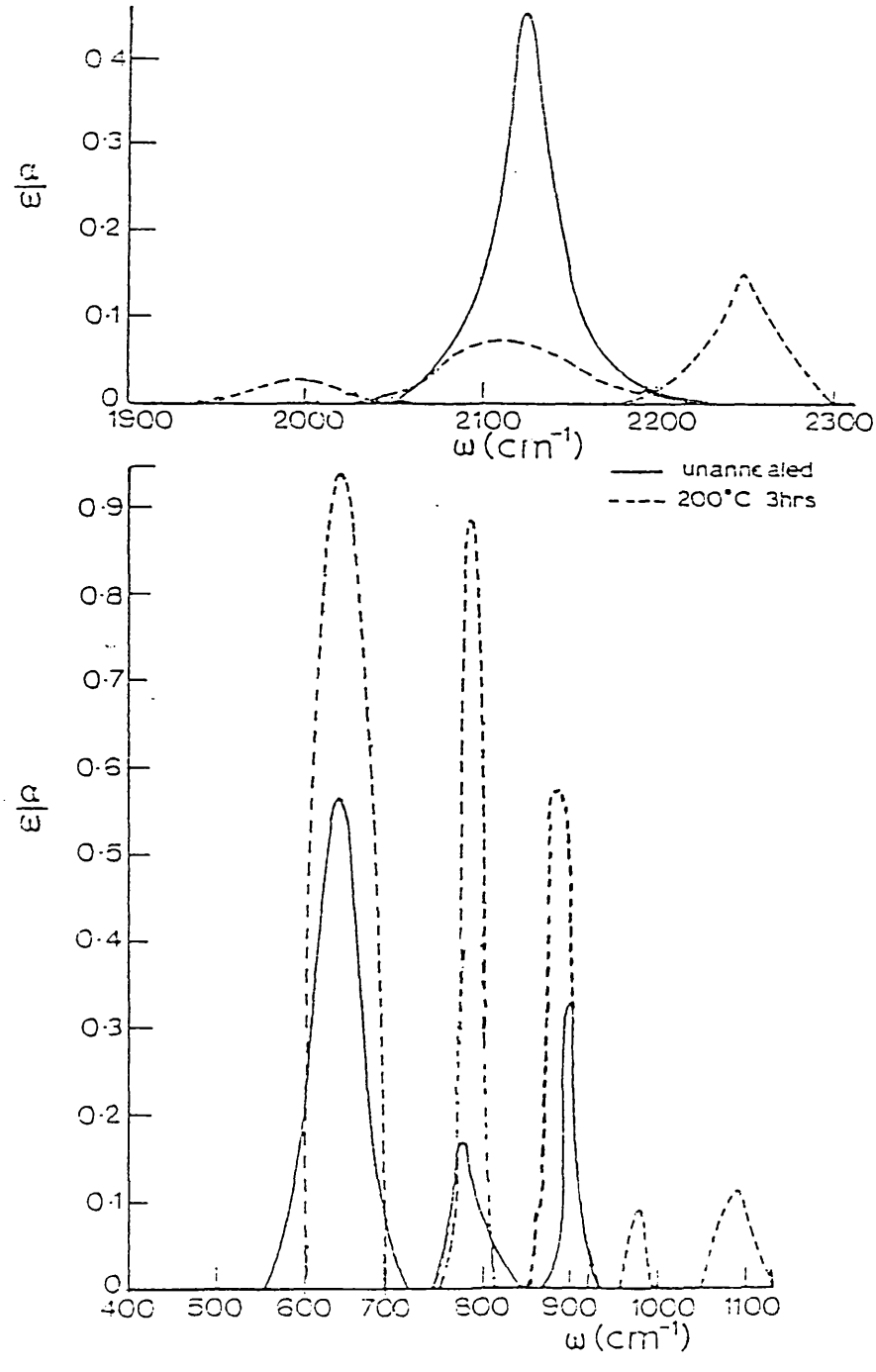

Fig. 4.7 IR absorption spectrum for a film prepared with a bias of -300 volts.

640 wag mode is increased and, if it were due only to hydrogen, it would correspond to 1.1×10^{21} atoms/cc. At the same time an $HSiO_3$ peak at 2250 has appeared. The 780 peak is increased and a 980 peak has appeared, indicating an increase in the number of oxygen bridging atoms present. Since there are peaks at 630 and 660 associated with these, at least part of the increase in the 640 peak may be ascribed to increased internal oxidation, which may account for the discrepancy in the apparent hydrogen content referred to above. It should be noted, however, that the 2100 peak may include a contribution from HSi_3O which cannot be separated out. The results would be consistent with a net loss of hydrogen due to annealing.

A tentative model for a suitable void is given in Fig. 4.8(a). The replacement of two hydrogens by oxygen bridging atoms in two types of position is shown in Fig. 4.8(b) and this would reduce the 2100 peak and introduce a 2000 Si-H peak, whilst reducing the total amount of hydrogen. When an oxygen atom forms a bridge in the position marked A, the configuration of Fig. 4.2.3 (c) is produced. Thus the peaks at 780 cm^{-1} and 980 cm^{-1} can also be accounted for. It is believed that this model can also be used to explain the void configurations observed in the d.c. bias ARE film explained earlier.

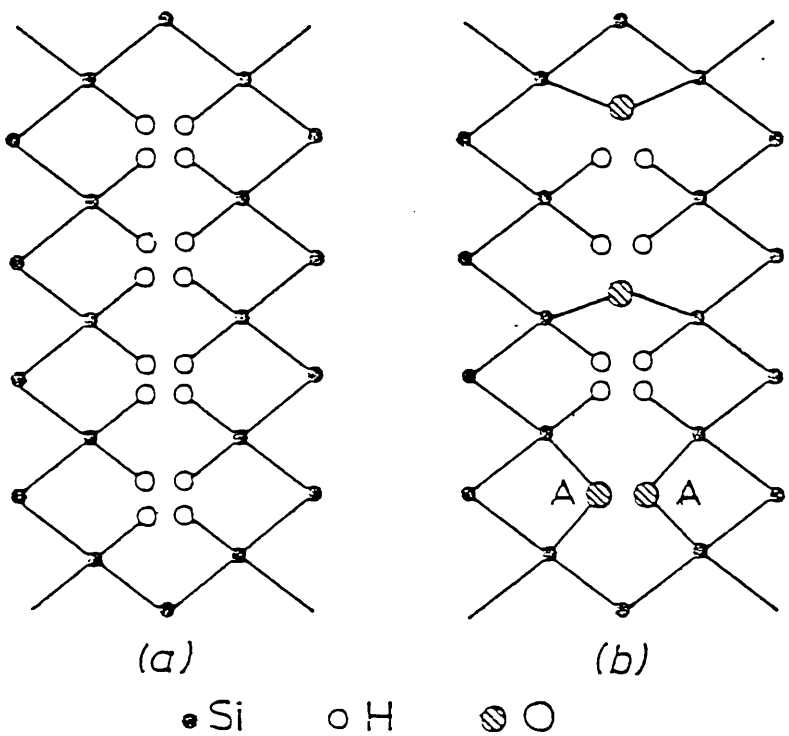

Fig. 4.8 Proposed model for a void (a) saturated with hydrogen, (b) with bridging oxygen atoms.

In Fig. 4.9 the spectrum for a film prepared at 0.14 μ/min and a bias of -1500V is shown. In the pre-anneal state the stretch modes corresponding to Si:H and $Si:H_2$ give a total content of 3.3×10^{21} H atoms/cc whilst the wag mode at 640 gives 1.85×10^{20}. There is a broad peak at 950 cm^{-1}. On annealing, the $HSiO_3$ peak at 2250 appears as also does the $Si:H_2$ bend mode at 875 cm^{-1}. The broad peak at 950 disappears and a peak at 780 appears, together with a broad peak around 1050. The stretch mode content is 2×10^{21} after 200°C anneal and 1.6×10^{21} after 300°C anneal. The comparable wag mode figures are 2×10^{20} and 1.2×10^{20}. It appears that the higher bias makes the voids less accessible to oxygen, so fewer hydrogen atoms are replaced by bridging oxygen atoms. The increased bombardment during growth is expected to produce a denser film [15].

Fig. 4.10 gives the spectrum for a film prepared from a 2 Ω-cm p-type ingot at 0.1 μ/min with a bias of -2200V. The hydrogen content is very low-giving, in the as-deposited state, a density of 6.75×10^{19} H atoms/cc from the stretch mode and 8.3×10^{19} from the wag mode, within experimental error those figures are in agreement. On annealing, the 2100 peak increases but the 2000 and 640 peaks remain much the same. The 2250 peak also increases whilst the 875 ($Si:H_2$ bend) peak disappears, which is expected to occur for oxygen concentrations greater than hydrogen concentration. This suggests surface oxidation at the expense of the SiH_2 groups. A feature of this film is a strong SiO_2 peak covering 1000-1200 cm^{-1}, seen in both cases.

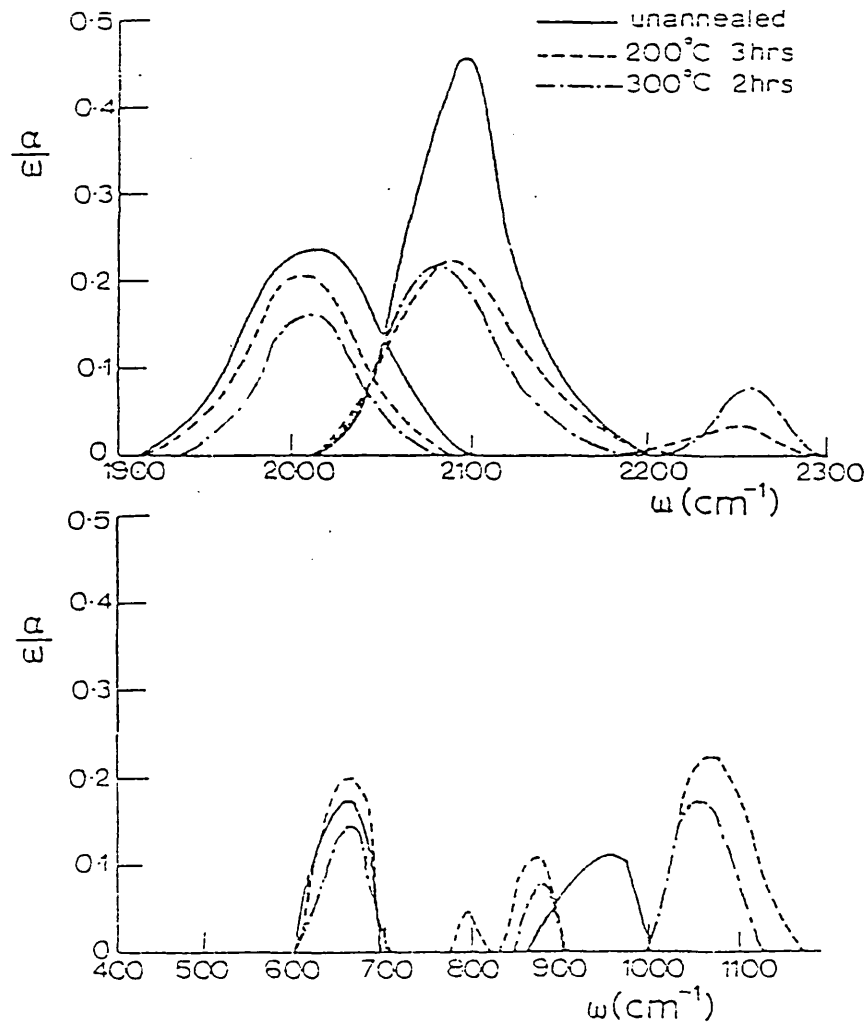

Fig. 4.9 IR absorption spectrum for a film prepared with a bias of -1500 volts.

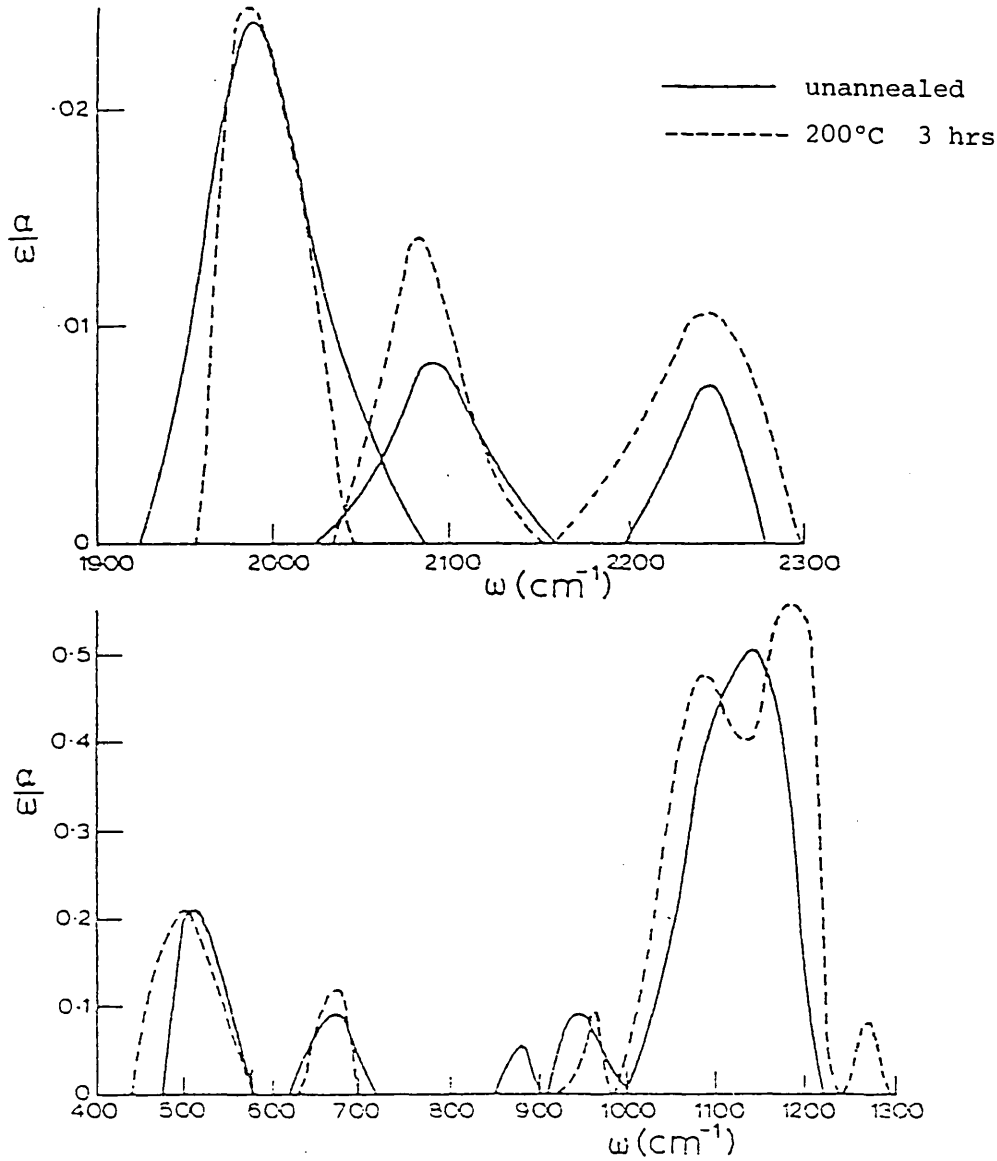

Fig. 4.10 IR absorption spectrum for a film prepared with a bias of -2200 volts.

4.1.7 I.R. Spectra of Optimised Intrinsic ARE Films

Figs. 4.11 to 4.16 show the IR transmission spectra for six coplanar samples. The corresponding α/ω versus ω plots are shown in Figs. 4.17 to 4.22. These samples were deposited under optimised conditions (see Table 4.2). They all have very good electrical properties with a photoconductive ratio (p.c.r.) (see Chapter 5, section 2.2) more than 10^4. The p.c.r. is defined as

$$\text{p.c.r.} = \frac{\text{conductivity in AM1 light}}{\text{conductivity in dark}}$$

at room temperature. With the exception of samples RE 195 and RE 213 they all have low hydrogen concentration compared to glow discharge material (not all the intrinsic sample spectrums are included in the text, nor are they tabulated in Table 4.2).

RE 195 has a hydrogen concentration of about 5.16% calculated from the wag mode compared with 1.52% calculated from the stretch mode. RE 213 has a hydrogen concentration of 19.6% calculated from the wag mode and 2.28% from the stretch mode. Although the hydrogen concentration has been quoted for the stretch modes, the estimate from the wag mode at 640 cm^{-1} is more accurate [13]. There was no apparent reason for the unusually large hydrogen concentration for the above two samples compared to the other intrinsic samples. The preparation conditions were almost identical for all the samples. There was no unusual peak in the IR spectrums (see Table 4.3) which could not be accounted for in either of the two samples.

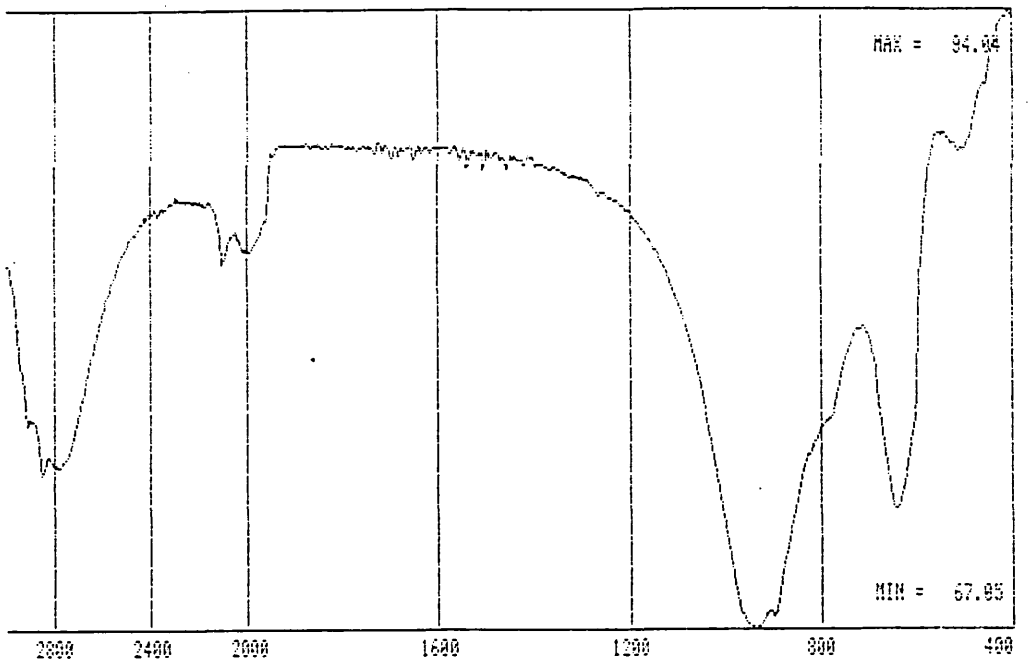

Fig. 4.11 IR Transmission RE 195

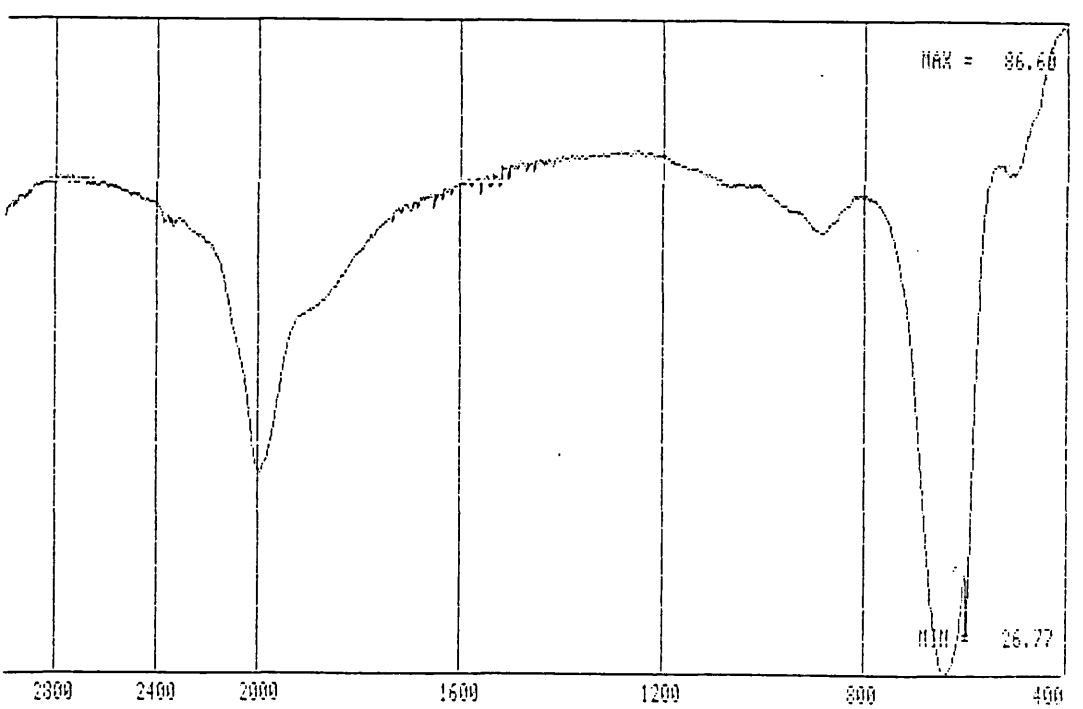

Fig. 4.12 IR Transmission RE 213

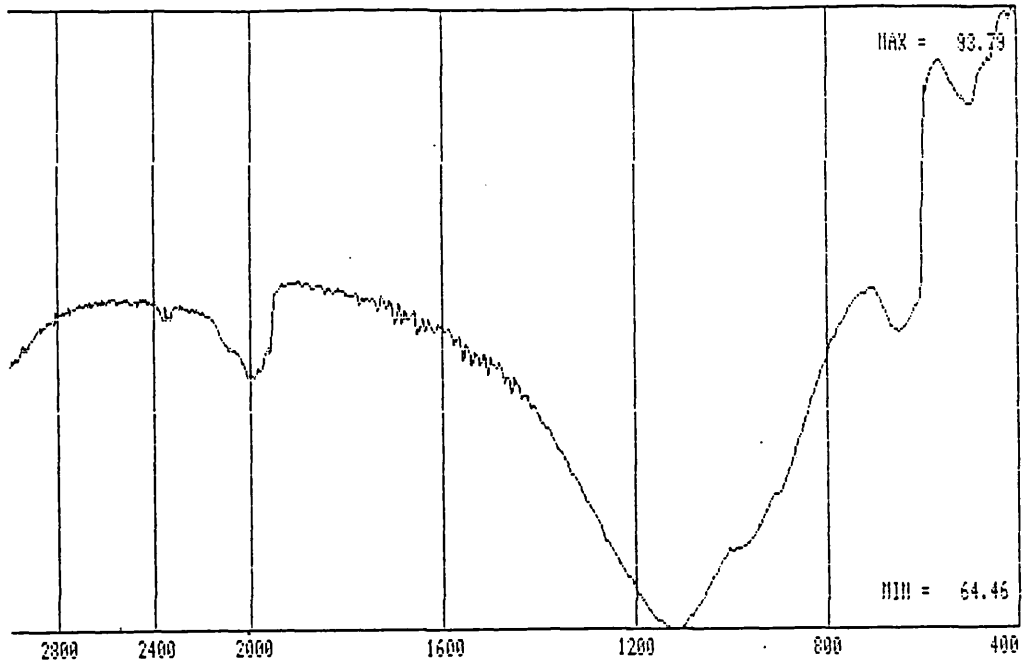

Fig. 4.13 IR Transmission RE 209

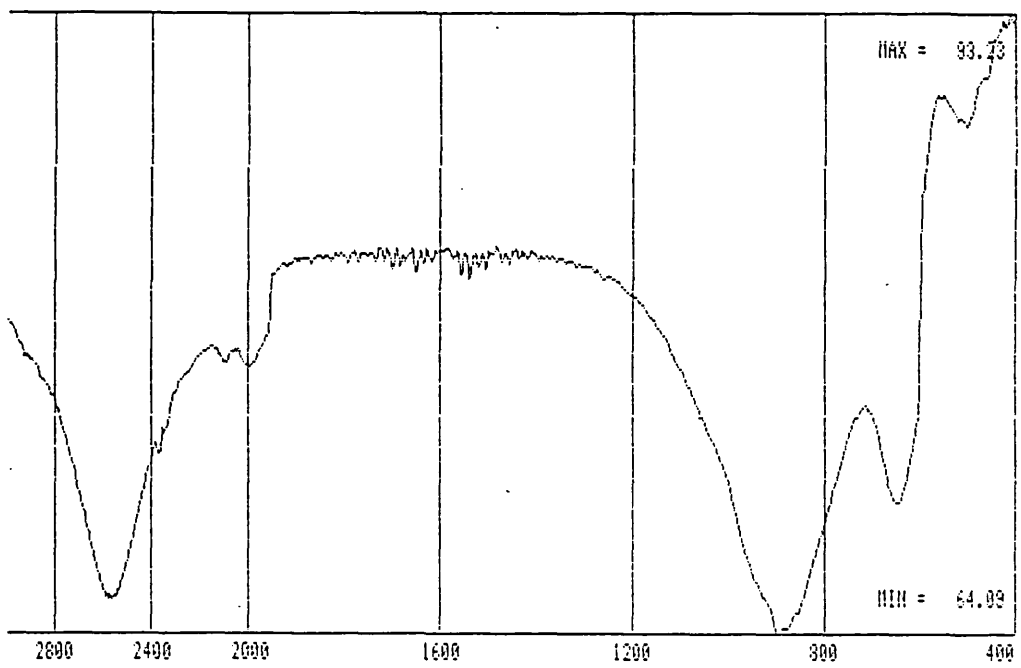

Fig. 4.14 IR Transmission RE 211

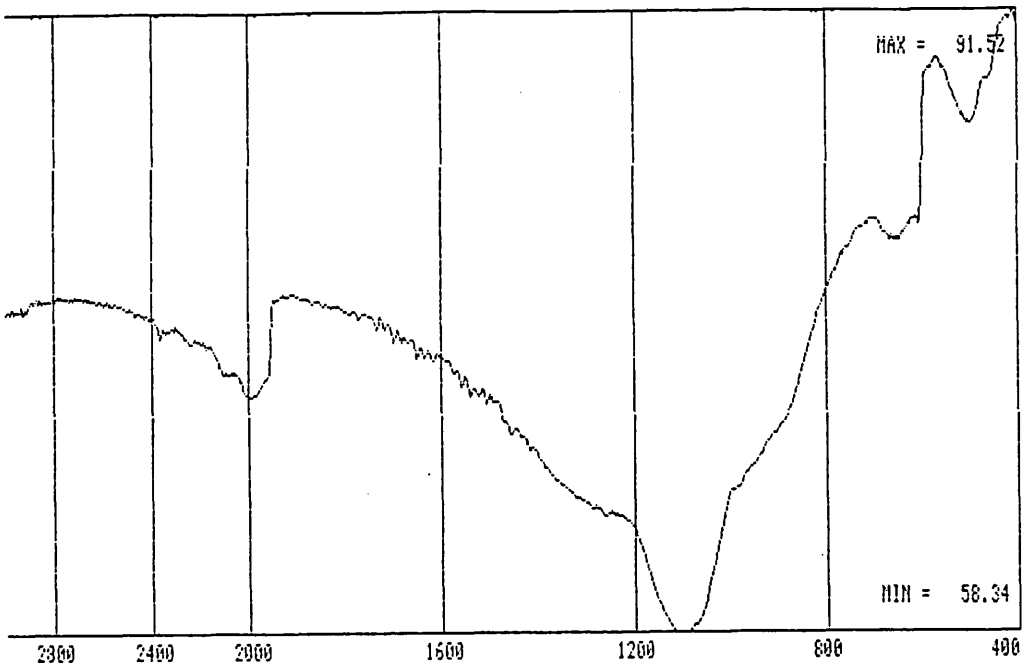

Fig. 4.15 IR Transmission RE 240

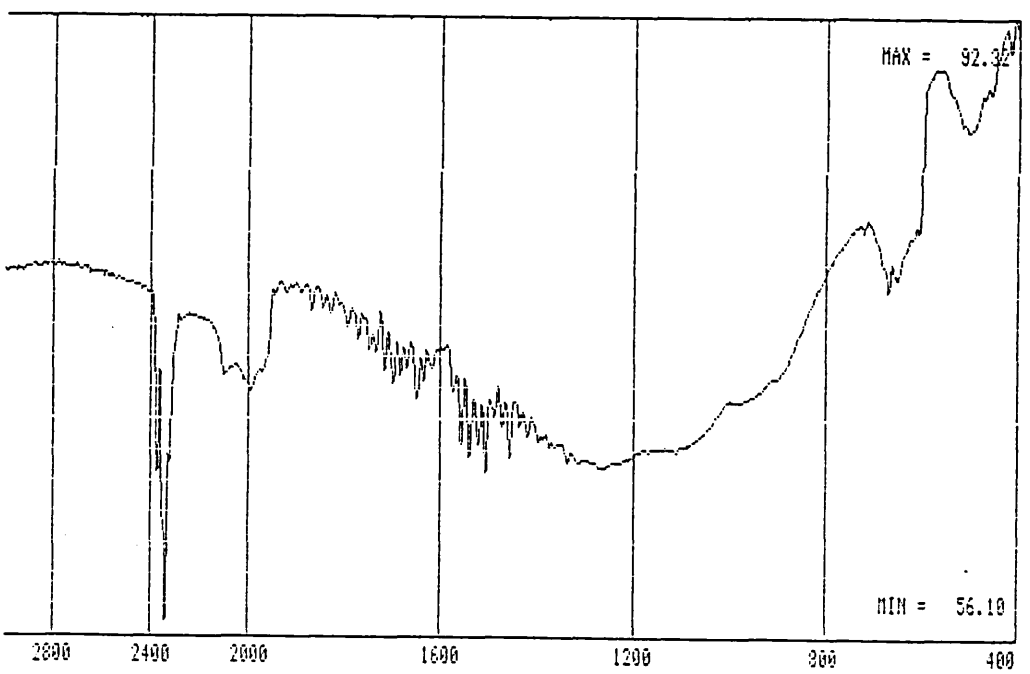

Fig. 4.16 IR Transmission RE 241

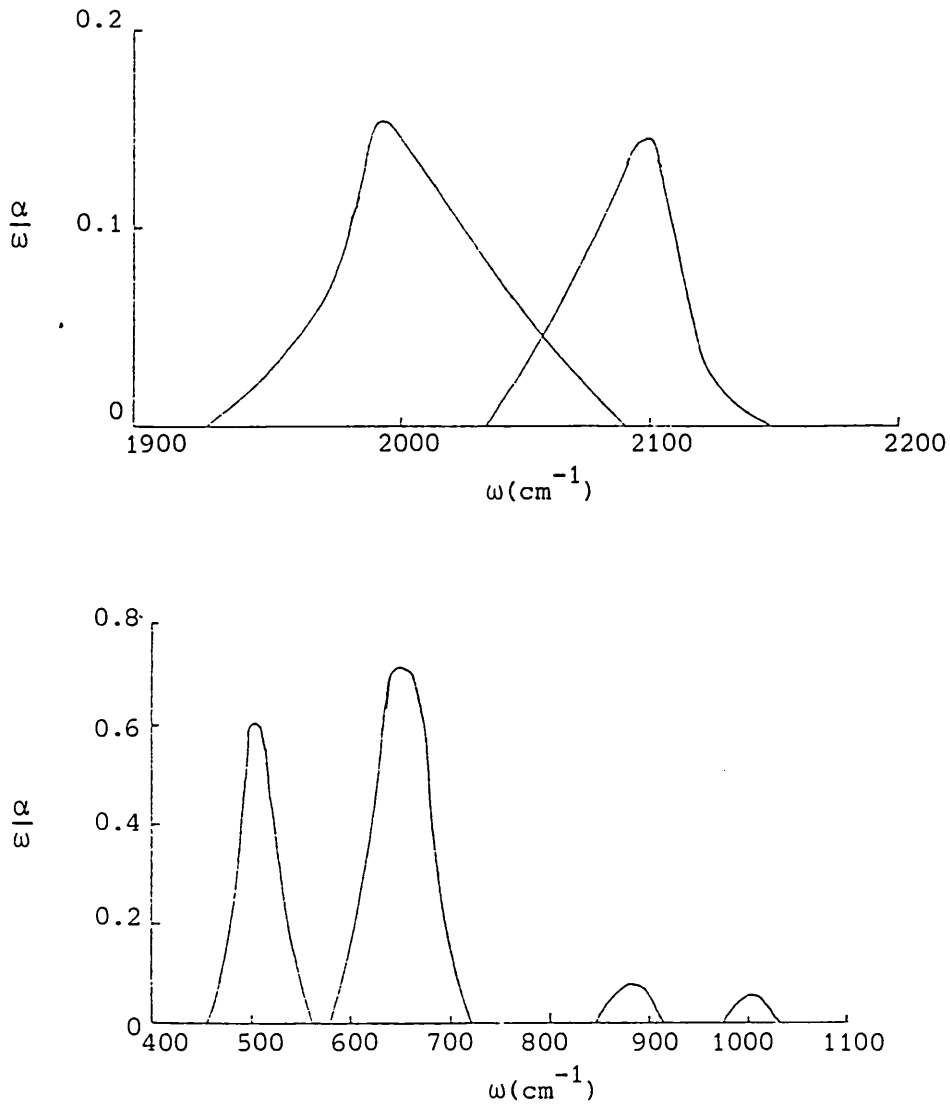

Fig. 4.17 Infra-red absorption spectrum of RE 195.

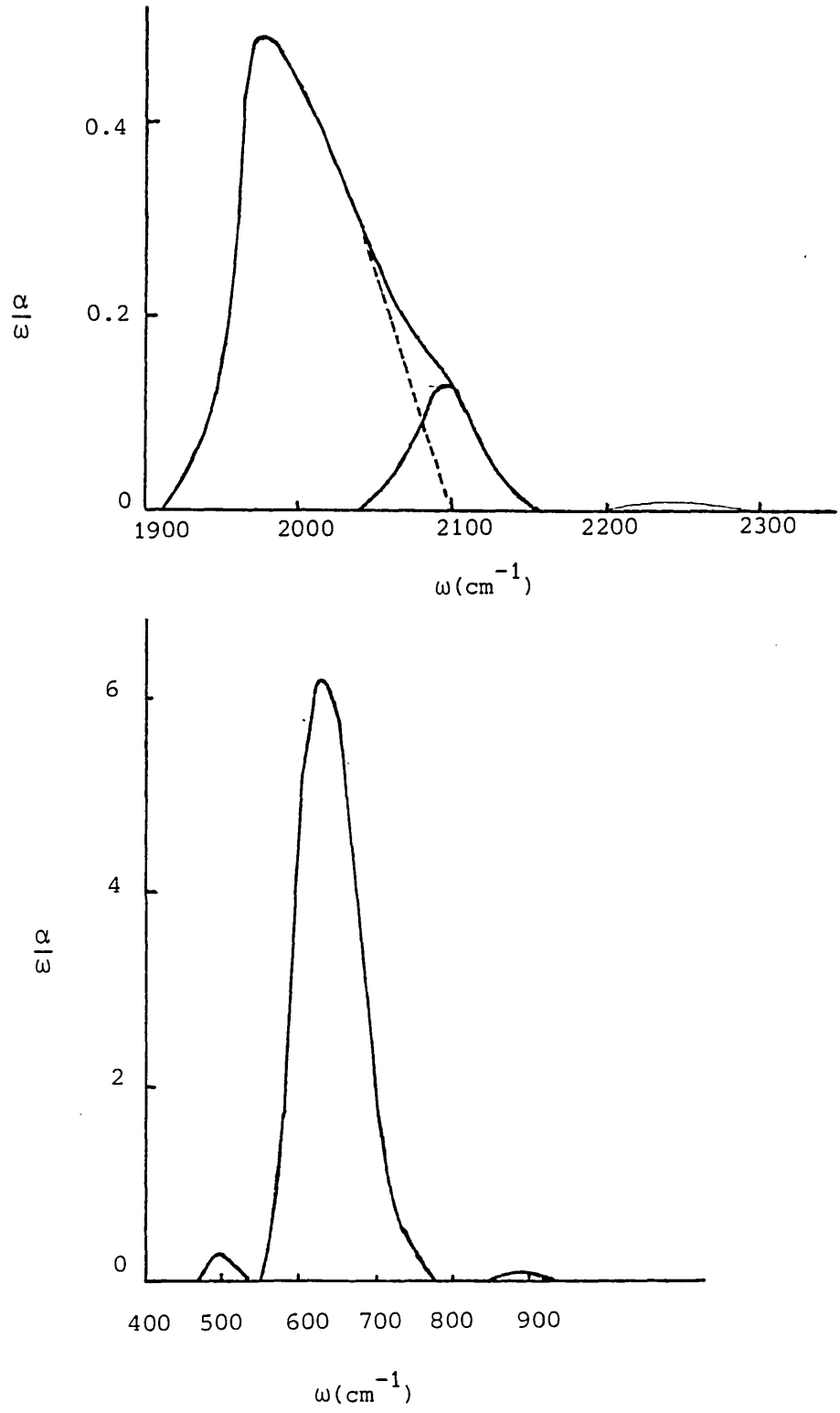

Fig. 4.18 Infra-red absorption spectra of RE 213.

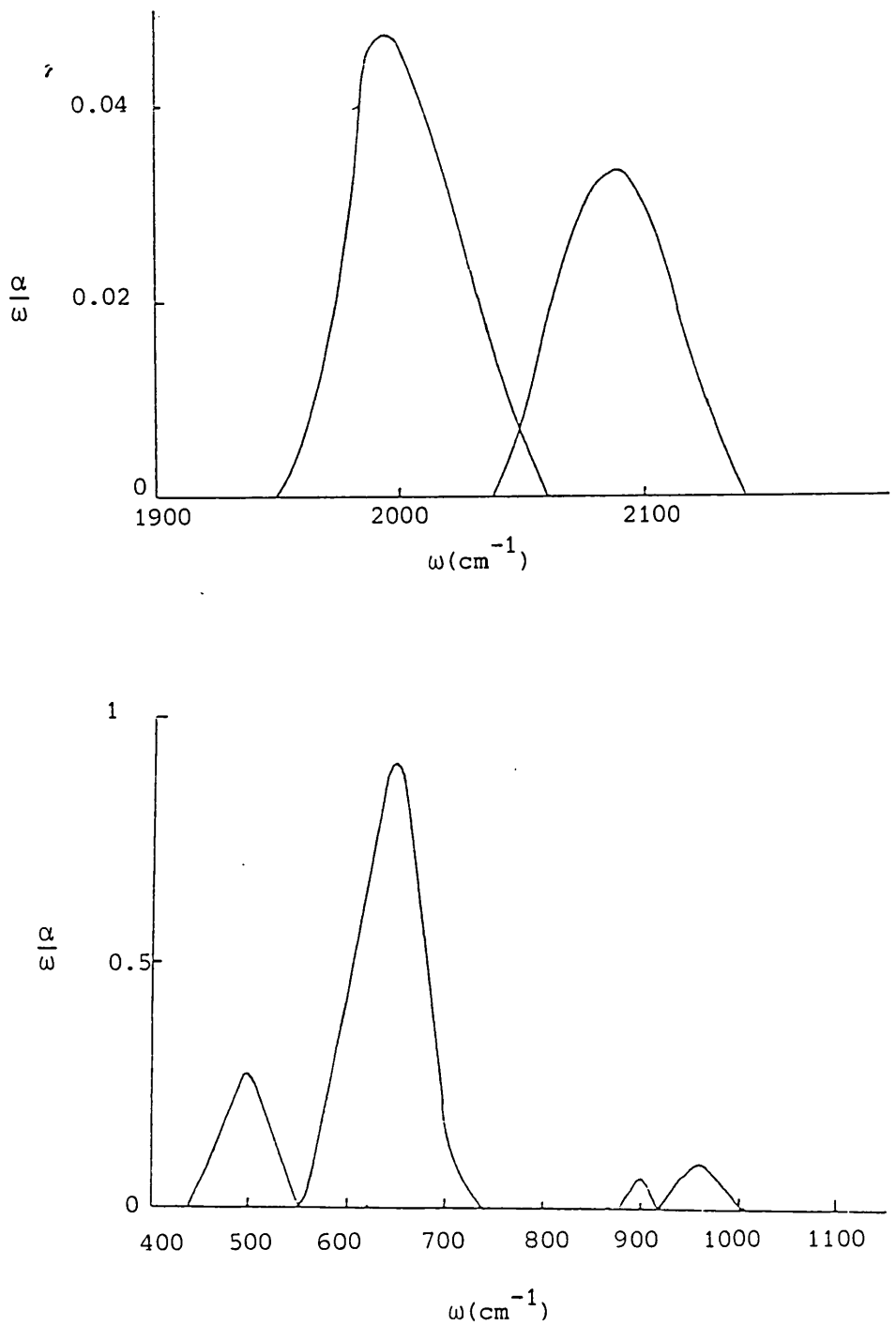

Fig. 4.19 Infra-red absorption spectra of RE 211.

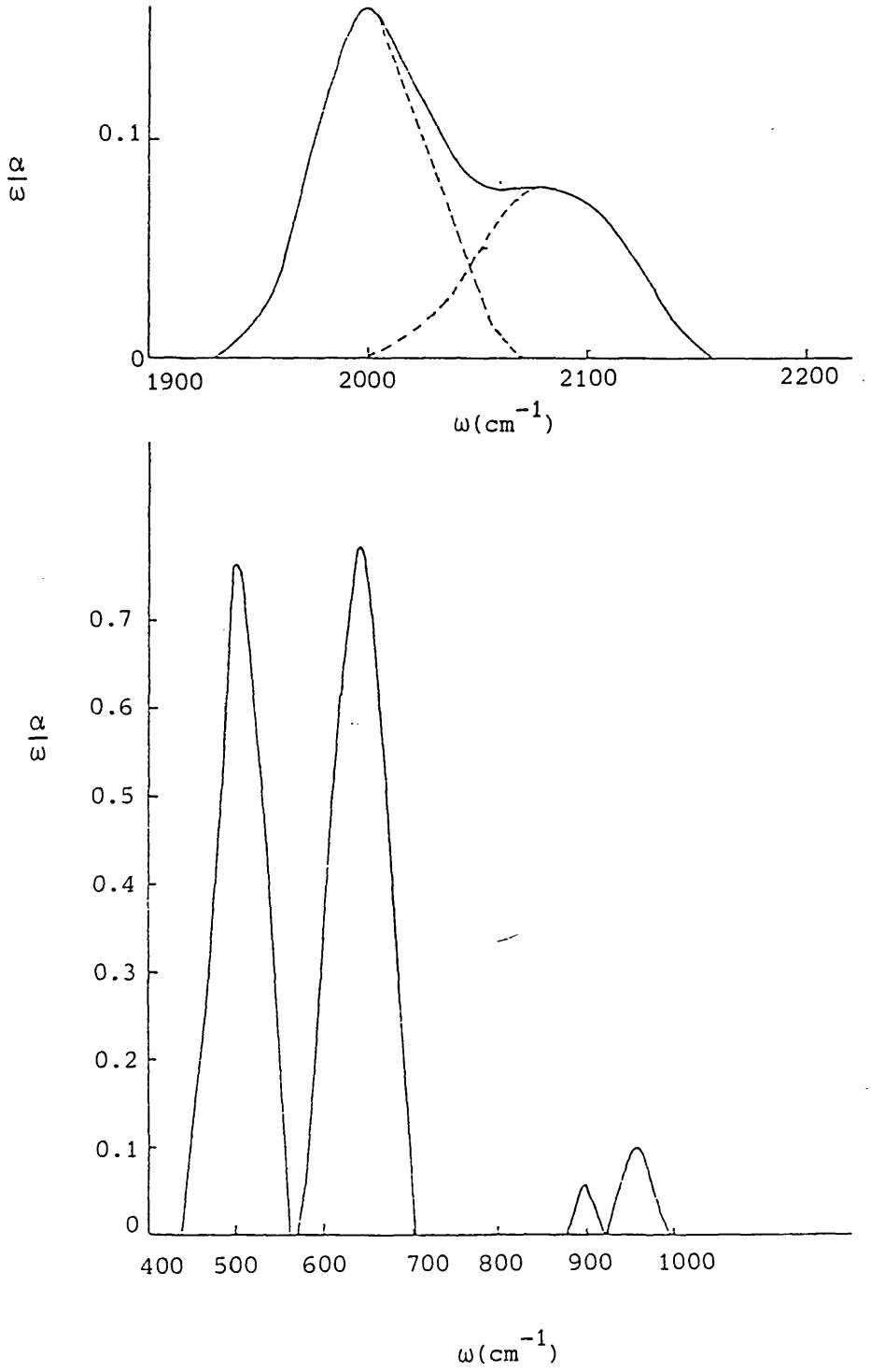

Fig. 4.20 Infra-red absorption spectra of RE 209.

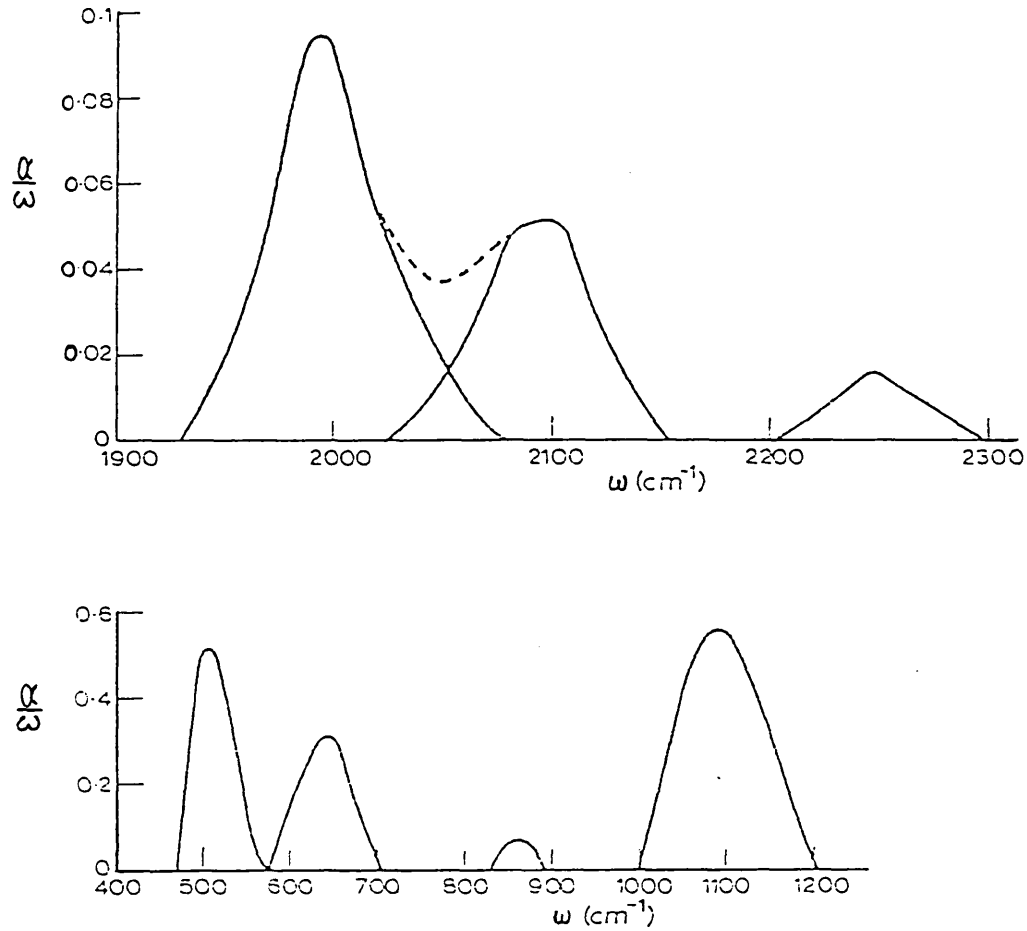

Fig. 4.21 Infra-red absorption spectra of RE 240.

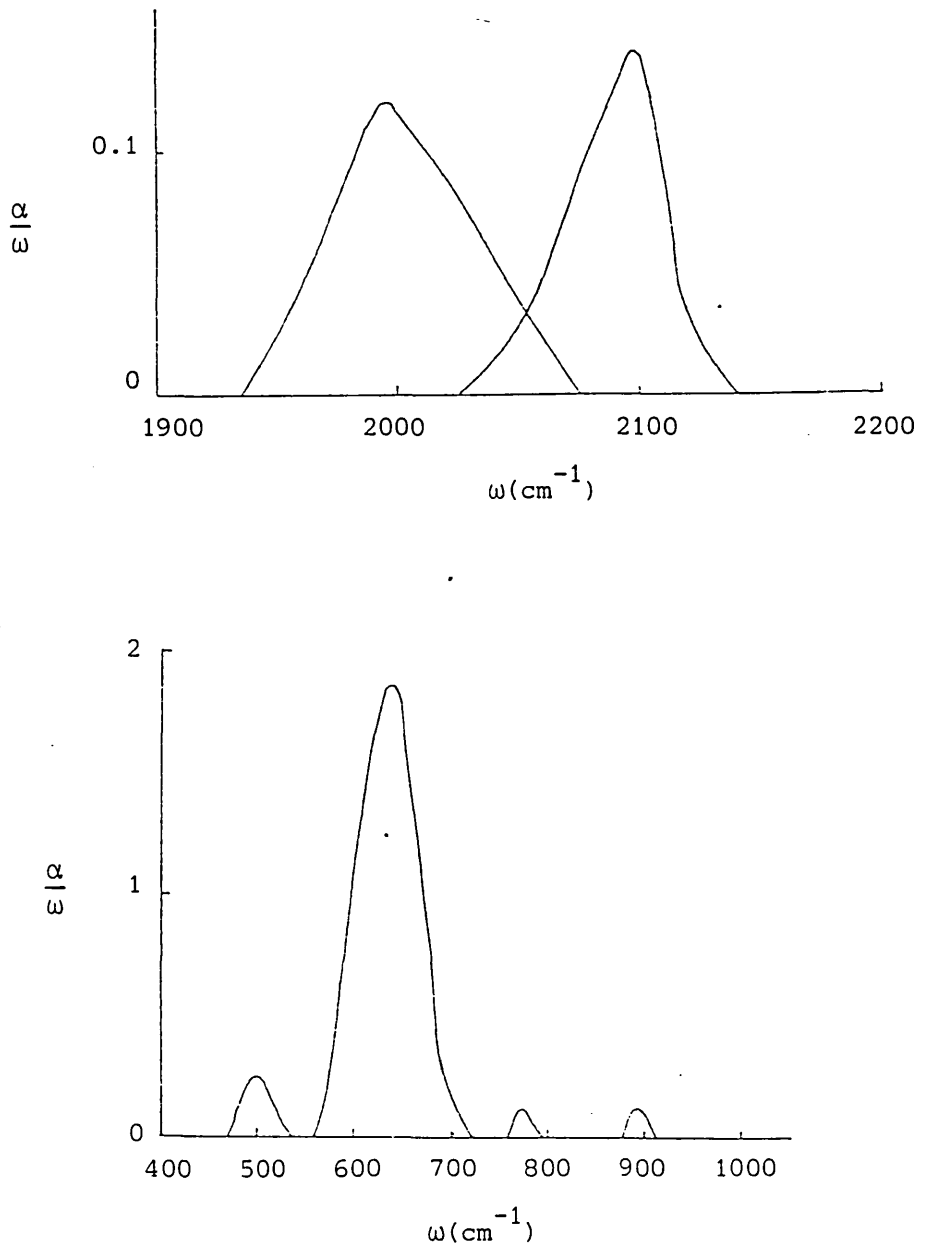

Fig. 4.22 Infra-red absorption spectra of RE 241.

Sample No.	Ingot Type	Rate um/min	Thickness um	H Flow sccm	Pressure mb	Bias volts	r.f.Power watt	Probe Volt	H(W) %	H(S) %	Room Temp. Cond. $(\Omega cm)^{-1}$	E_σ eV	P.C.R.
195	0.002n	.115	.525	45	1.8×10^{-2}	-2400	350	290	5.16	1.52	1×10^{-10}	.84	1×10^{4}
209	12p	.16	.8	50	1.2×10^{-2}	-2577	380	310	2.08	1.87	3×10^{-11}	.77	2.7×10^{4}
211	12p	.16	.82	52	1.5×10^{-2}	-2500	350	320	2.4	0.4	3.7×10^{-11}	.79	7.8×10^{4}
213	12p	.24	1.2	52	1.3×10^{-2}	-2500	350	310	19.6	2.28	7×10^{-12}	.87	3×10^{4}
240	Int	.14	.7	60	2.0×10^{-2}	-2420	365	300	0.72	0.72	9×10^{-11}	.77	1.33×10^{4}
241	12p	.10	.6	60	2.0×10^{-2}	-2514	380	290	1.72	1.3	3.5×10^{-10}	.73	2.86×10^{4}

Table 4.2

Sample No.	2000	2090	2100	2240	500	640	780	875	890	950	1100
RE 195	yes	no	yes	no	yes	yes	yes	yes	no	no	no
RE 213	yes	no	yes	yes	yes	yes	no	yes	no	no	no
RE 211	yes	yes	no	no	yes	yes	no	no	yes	yes	no
RE 209	yes	yes	no	no	yes	yes	no	no	yes	yes	no
RE 240	yes	no	yes	yes	yes	yes	no	yes	no	no	yes
RE 241	yes	no	yes	no	yes	yes	no	yes	no	no	no

Table 4.3

A set of experiments was carried out to investigate the effects of the presence of oxygen and self bias (on the substrate). The self-biassing was done as discussed earlier by connecting the substrate to earth through a high impedance (10^7 Ω) digital voltmeter. This produced a positive self-bias potential on the substrate with net current to it of ~10 μA and the volt meter recorded the value of the positive self-bias potential. The samples thus prepared gave larger hydrogen concentrations. This suggested that the hydrogen incorporation was not a surface effect, brought about by bombardment of the film with hydrogen ions, but via a gas phase reaction. From the work on solid phase doping using a silicon and antimony alloy (see Chapter 5, section 3.2) it was found that these samples also contained larger amounts of hydrogen (see Table 4.4). In this case the substrates were negatively biassed. These ten samples were the only ones with higher hydrogen concentrations; those produced under-optimised conditions, with negative r.f. bias had invariably low concentrations (~0-1.5%).

It is suggested that in the case of the argon and nitrogen mixtures (RE 185-RE 194), the overall degree of ionisation of the hydrogen is increased by the presence of the heavier, more easily ionised atoms. This results in an increased formation of $Si:H_x$ fragments in the plasma and increased hydrogen content in the film. A similar mechanism will occur in the presence of a significant density of antimony atoms in the plasma. The exceptional samples RE 195 and RE 213 were both deposited immediately

Sample No.	%H (Wag)	Bias	Gas Mixture
RE 185	3.57	r.f	Ar+H
RE 189	3.63	self	N+H
RE 191	5.67	self	Ar+H
RE 193	13.7	self	Ar+H
RE 194	11	self	Ar+H
RE 195	5.16	r.f	H
RE 213	19.6	r.f	H
RE 214	6.8	r.f	Sb+H
RE 215	21.2	r.f	Sb+H
RE 216	9.5	r.f	Sb+H

Table 4.4

after a run in which argon had been used. It may be that sufficient argon remained in the pipework and chamber to cause increased ionisation.

In Table 4.3 it can be seen that RE 209 and RE 211 both exhibit peaks at 890 cm^{-1} and 950 cm^{-1}. It seems that the symmetric bend mode of $Si-H_2$ has shifted from 875 cm^{-1} to 890 cm^{-1}. It cannot be part of the doublet 840 and 890 cm^{-1} corresponding to the bend mode of $(Si-H_2)_n$ as neither the 840 cm^{-1} peak nor the stretch mode peak at 2100 cm^{-1} of $(Si-H_2)_n$ exist. The stretch mode of Si-O-Si has also shifted from 980 cm^{-1} to 950 cm^{-1}. This peak is observed at 950 cm^{-1} for oxygen concentration below about 0.03% and progressively moves towards 1050 cm^{-1} for higher concentrations, (11(b), 12(c)). Some inclusion of oxygen into the film is unavoidable. This is either caused by water molecules which effuse out of the chamber walls or can be accounted for by very minute leaks. All the above films, although of good quality, do show traces of oxygen in one form or another.

Indeed, it has been shown that the incorporation of oxygen into sputtered films of a-Si:H improves the quality of the films and approaches those of the glow discharge films [16] (M.A. Paesler et al, 1978).Paesler et al suggested that oxygen may alter the properties of a-Si:H films in several ways. The bridging oxygen can serve as a network softener. The twofold coordinated O atoms decrease the number of defects and thus increase the recombination lifetime. In sputtered a-Si:H films the room temperature dark conductivity is lowered and the corresponding activation energy is increased[16, 17]. The transport is also singly activated

over the temperature range of 300 to 480K. The change in d.c. photoconductivity is also about three orders of magnitude in the presence of traces of oxygen. The addition of oxygen reduces the number of recombination centres and thus the change in the photoconductivity is seen. Paesler et al suggest that the change is due to a change in $\mu\tau$ product with the mobility, μ, remaining relatively constant.

It has not been possible to prepare oxygen free ARE a-Si:H films; this would require an ultra-high vacuum system for such experiments. It is, however, believed that oxygen plays a vital role in the electrical and optical properties of the ARE films. It must be emphasised that the oxygen concentrations are less than 0.03%. Much higher levels of oxidation are detrimental to the electrical properties.

An interesting feature is that for all the good intrinsic films there is a substantial and relatively sharp Si-Si peak at 500 cm^{-1}, indicating that most of the silicon atoms are in tetrahedral coordination and there are relatively few dangling bonds to be taken up by hydrogen.

In films prepared under optimum conditions the hydrogen bonding is predominantly in the Si-H configuration although $Si-H_2$ bonds are also observed.

In summary, the use of bias evidently reduces the number of dangling bonds in the amorphous silicon and eliminates microvoids so that there is less hydrogen uptake.

4.1.8 Doped ARE Films (IR Spectra)

There were three different categories of infrared spectra:

Sample No.	%PH / Si Rate (um/min)	%Hydrogen (Wag)
RE 239	0.769	0.74
RE 238	1.9	0.48
RE 237	3.57	0.16
RE 232	6.25	0.27
RE 236	6.82	0.17
RE 235	7.14	0.3

Table 4.5

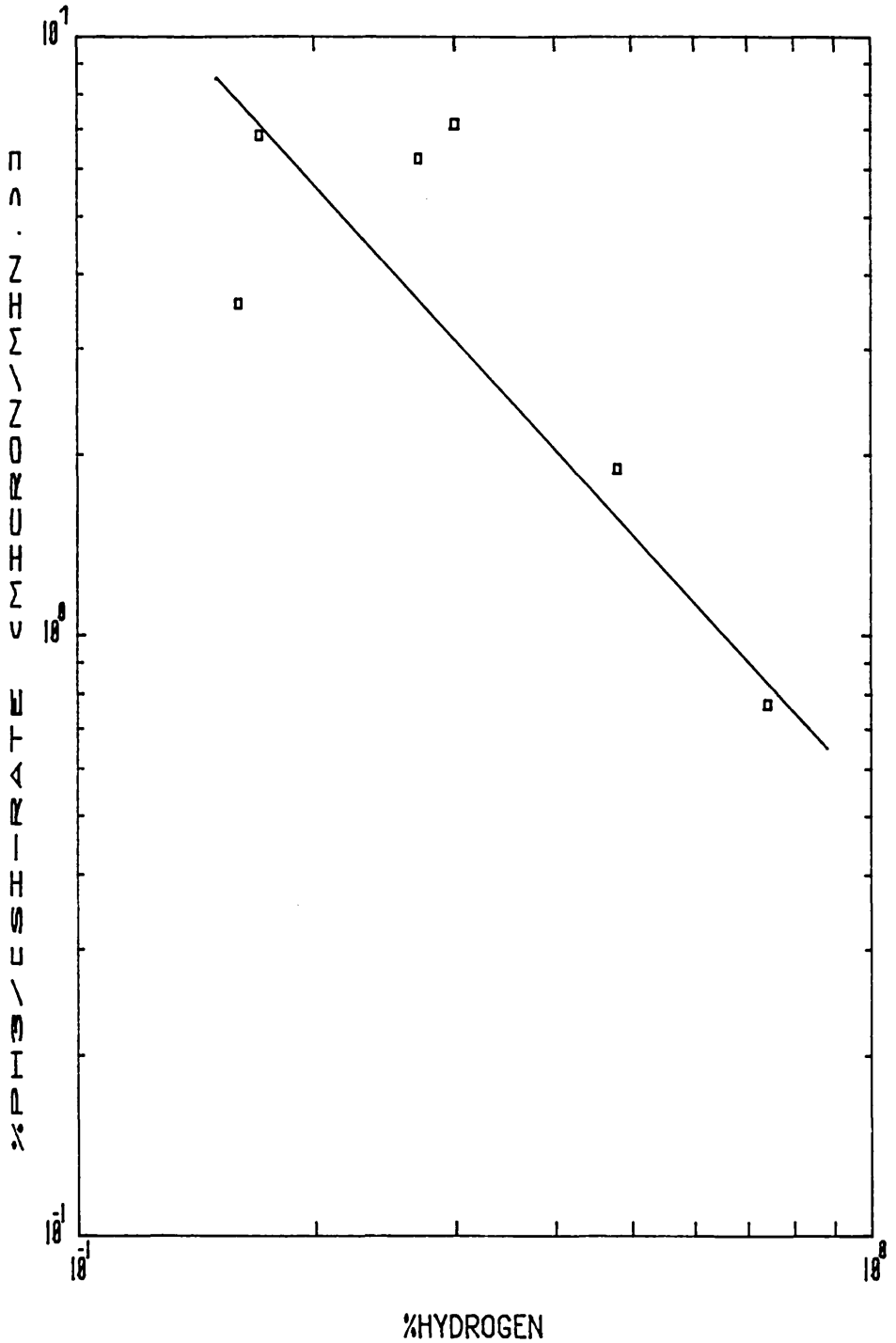

Fig. 4.23 The variation of hydrogen content with phosphorus incorporation.

(a) Antimony doped (solid phase)

(b) Phosphorus doped (gas phase)

(c) Boron doped (gas phase)

For the antimony doped films, as discussed in the last section, the hydrogen contents were relatively large (see Table 4.4) compared to the intrinsic samples. This was attributed to increased ionisation due to the presence of a significant density of antimony atoms.

In the case of doping with phosphorus, the hydrogen content was not significantly altered although there was a trend towards lower hydrogen content as the phosphorus content was increased (as is indicated in Table 4.5 and Fig. 4.23).

In Fig. 4.23 the variation of percentage PH_3/Si rate (μm/min) with percentage hydrogen content calculated from the wag mode is shown.

This trend was much stronger in the case of boron doping as indicated in Table 4.6 and Fig. 4.24. This trend was also found in glow-discharge films [18].

Discharge-produced amorphous silicon has been successfully doped because it has a relatively low density of gap states (Spear and LeComber 1972),[4]. The conductivity of ARE produced a-Si:H can be varied over eleven orders of magnitude by using a gas phase doping (see Chapter 5). Therefore it can be assumed that these films have a relatively low density of gap states. Early attempts to dope amorphous Ge and Si were unsuccessful (Luby 1971,[19], Anderson, Davey, Conas, Saks and Lucke 1974), [20] because

Sample No.	%B H / Si Rate (um/min)	%Hydrogen (Wag)
RE 256	0.23	1.88
RE 254	0.46	3.8
RE 258	1.4	0.083
RE 253	2.05	0.1
RE 252	8.0	0.09
RE 259	32.9	0.05
RE 248	38	0.03
RE 250	44	0.03
RE 249	66.7	0.003

Table 4.6

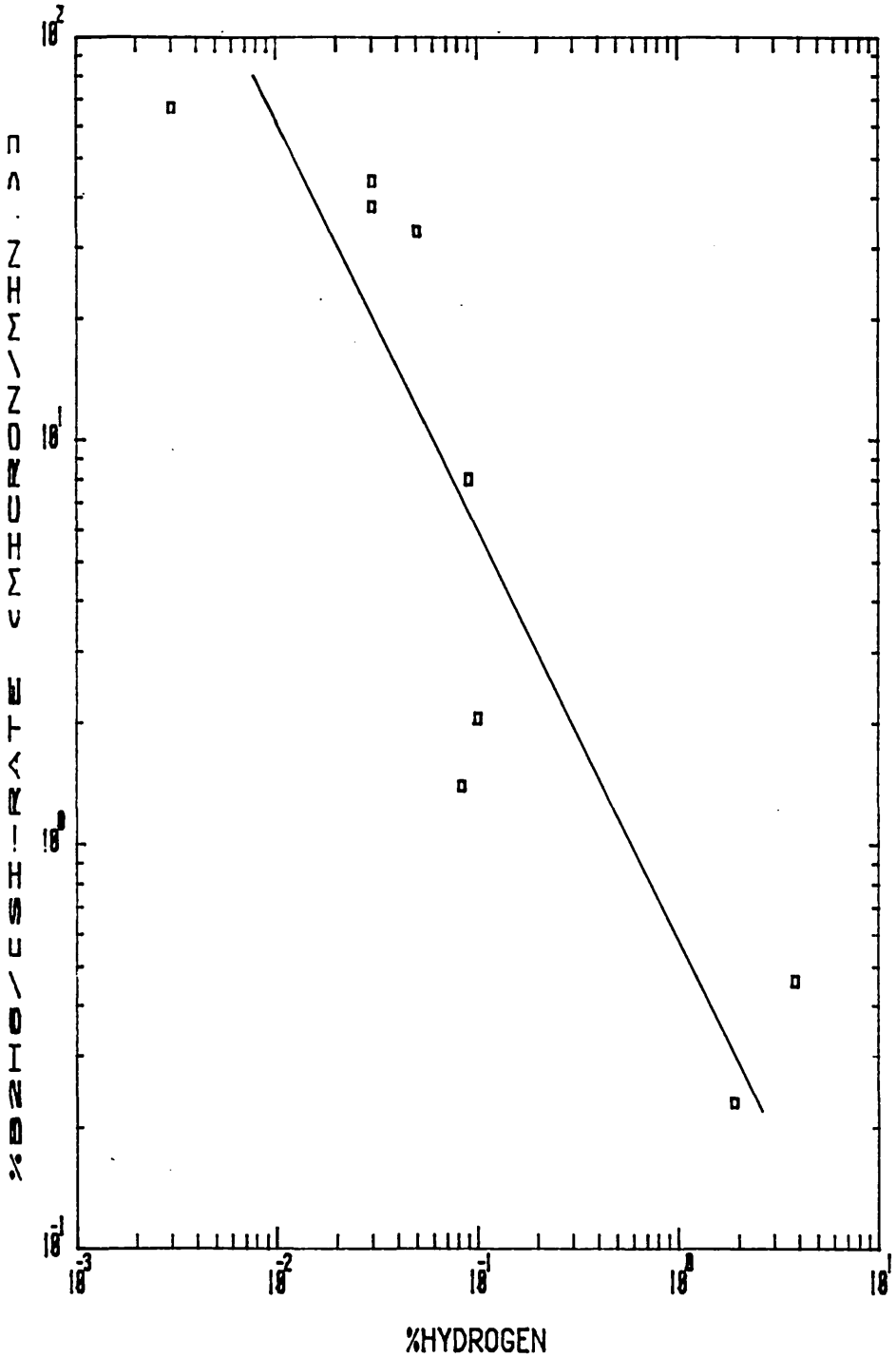

Fig. 4.24 The variation of hydrogen content with boron incorporation.

the films contained a large number of dangling bonds (Brodsky and Title 1969), [2]. The Fermi level is pinned by these states, and dopant atoms such as phosphorus have relatively little effect on the electrical properties of evaporated or sputtered films of a-Si (Carlson et al, 1982) [21].

Street and Biegelsen 1980, [22] suggested that doping increases the defect density by generating dangling bonds. Carlson et al [21], suggested that the increased defect density in a-Si:H is due to the formation of dopant-hydrogen complexes. They suggested that these complexes contribute to gap states even in lightly doped a-Si:H, and to achieve better quality films the plasma chemistry needs to be improved to minimise the formation of dopant-hydrogen complexes (B_xH_y, P_xH_y, where x and y = 1,2, etc.).

In the ARE films it appears that we have some formation of B-H bonds at the expense of Si-H bonds to give the following grouping:

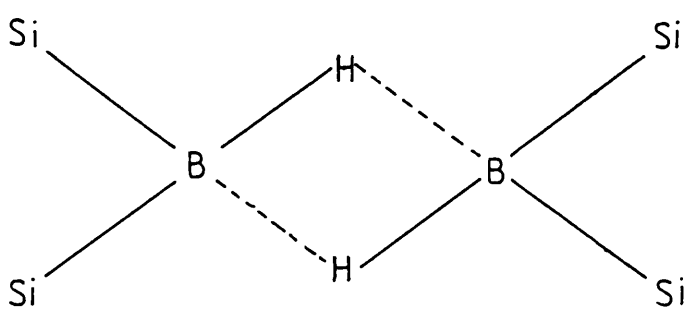

This is consistent with the results presented here. With increasing boron concentration the Si-H concentration decreases.

4.2 VISIBLE ABSORPTION MEASUREMENTS

Transmission and reflection spectra of the a-Si:H films in the visible range were taken on a Varian 2300 series spectrometer within the wavelength range of 0.5 μm to 1 μm. The spectrometer is a double beam type. For the transmission spectra, an identical blank 7059 glass substrate was placed in the reference beam which enabled the fractional transmittance of the film on a 7059 glass substrate to be obtained. The reflectance spectra were obtained by using a specular reflectance accessory with respect to an unobstructed reference beam.

The silicon films were deposited on 7059 glass for optical measurements because it is non-absorbing over the wavelength range used and has a reflectivity of less than 3.5% over the same range.

In the as-obtained spectra the interference maxima and minima were averaged out before calculations were performed.

The transmission coefficient is defined as the ratio of transmitted to the incident power, I/I_o. If the specimen has a thickness d, an absorption coefficient α, and a reflectivity R, the total transmission can be expressed as

$$T = \frac{(1-R)^2 \exp(-\alpha d)}{1-R^2 \exp(-2\alpha d)} \qquad (4.8)$$

The above expression [23,24] takes into account multiple reflections inside the film.

The absorption coefficient $\alpha(\omega)$ was calculated, on a CBM Commodore PET 4032 microcomputer using the program

in Appendix 3, from experimental transmittance and reflectance data. The program solves the above equation (4.2.1).

The optical bandgap was found from the dependence of the absorption coefficient α on the photon energy $h\nu$ [25], i.e.

$$\alpha h\nu = B(h\nu - E_o)^2 \qquad (4.9)$$

where B is a constant and E_o is the optical bandgap. The values of E_o were determined using $\sqrt{\alpha h\nu}$ versus $h\nu$ plots. The above relationship assumes a parabolic distribution of density of states N(E) with energy in the vicinity of the band edges.

Optical absorption in crystalline semiconductors involves the transition of an electron across the bandgap. In the case of direct bandgap semiconductors (e.g. crystalline GaAs), the momentum is automatically conserved in optical transitions.

In the case of indirect bandgap semiconductors, such as crystalline silicon, the transition is phonon assisted and the photon absorption is less efficient.

In the case of amorphous silicon the $\underset{\sim}{k}$ (wavevector) selection rules are relaxed and all transitions are allowed without phonon absorption or emission. In this respect it resembles a direct gap material and the absorption process is similarly more efficient.

Optical absorption in the visible range was measured for representative films with the results given in Figs. 4.25-4.28, in which the absorption coefficient in $(\mu m)^{-1}$ is plotted

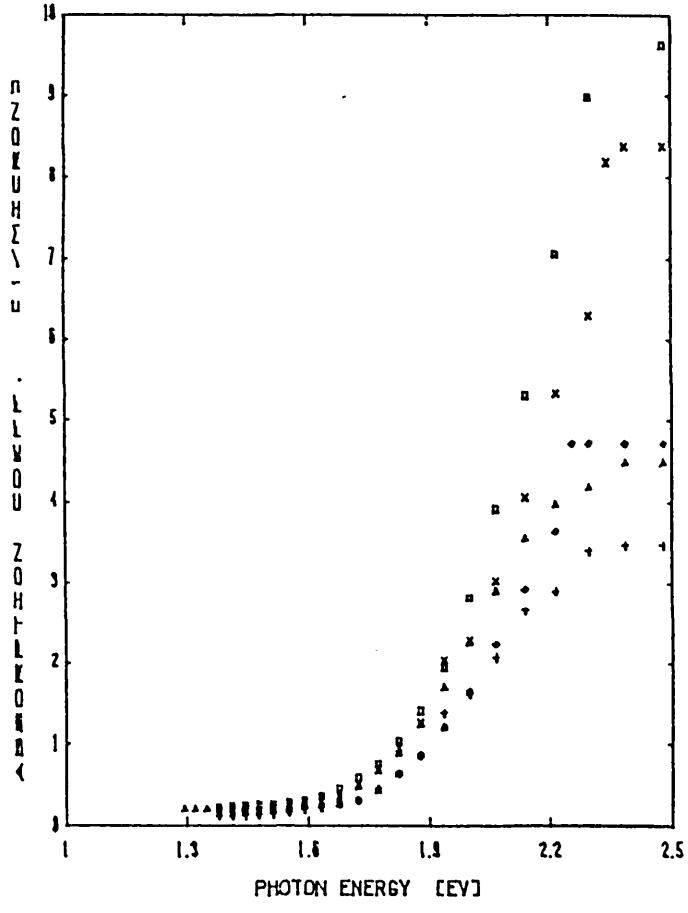

Fig. 4.25 Optical absorption spectra of intrinsic a-Si: H.

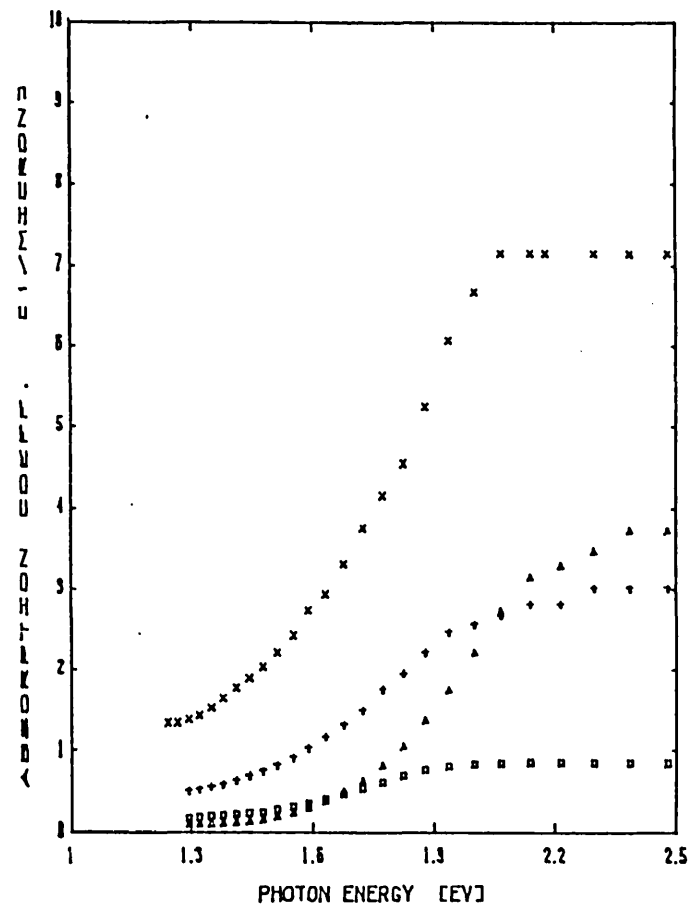

Fig. 4.26 Optical absorption spectra of B_2H_6 doped a-Si: H.

Fig. 4.25 to 4.28 - Saturation in α is a result of experimental artefact.

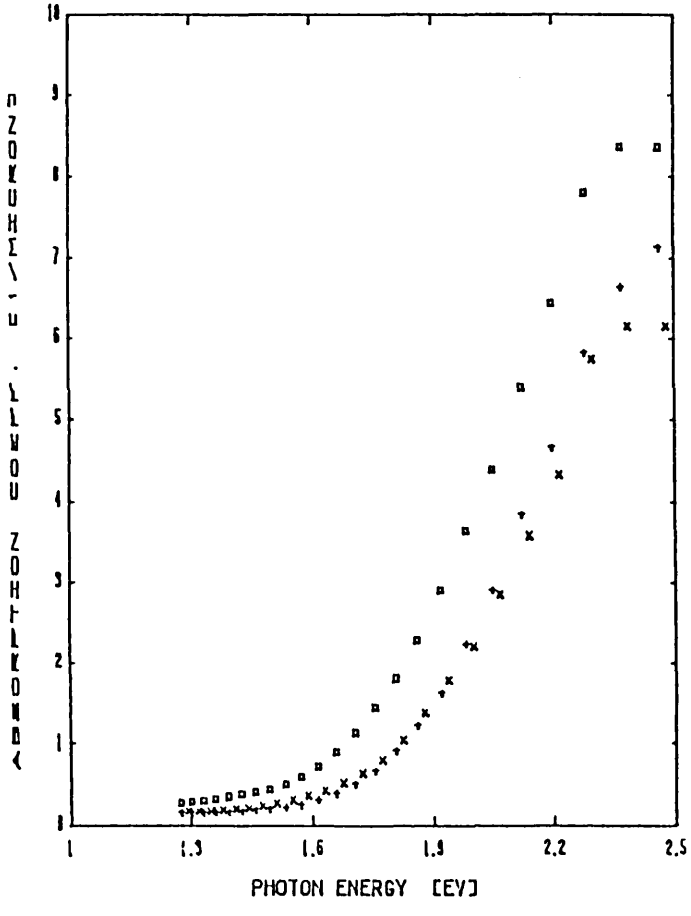

Fig. 4.27 Optical absorption spectra of PH_3 doped a-Si: H.

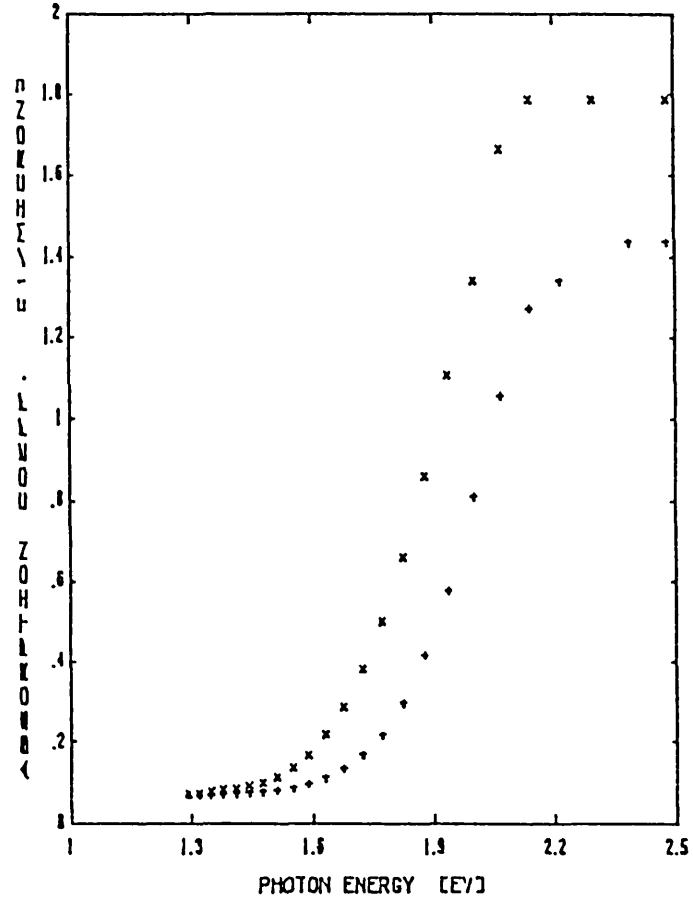

Fig. 4.28 Optical absorption spectra of Sb doped a-Si: H.

against photon energy in eV. For the intrinsic films (Fig. 4.25) the maximum absorption at 2.5 eV is in the range ~3.5 x 10^4 cm^{-1} to ~10^5 cm^{-1}, closely comparable with results from glow discharge films. The minimum absorption for sub-bandgap radiation is $\lesssim 10^3$ cm^{-1}.

In Fig. 4.26 the data is displayed for four p-type a-Si:H films. The maximum absorption at 2.5 eV for the film RE 253 is only ~1 x 10^4 cm^{-1} and was very untypical of the p-type films. In general their absorptions were between ~3 x 10^4 cm^{-1} and ~9 x 10^4 cm^{-1}.

In Fig. 4.27 are shown the spectra for three n-type films (PH_3-doped). The values for α were similar to the intrinsic films (at 2.5 eV).

In contrast to the above results, the absorption coefficient α at 2.5 eV for the antimony doped films (Fig. 4.28), prepared from the alloy ingot, was about an order of magnitude lower than the intrinsic or the phosphorus-doped films. The value of α also decreased with increasing antimony content contrary to the case of phosphorus doped films. This was an important finding since, for n-i-p solar cells, it is important to minimise the absorption of light in the n-layer.

The optical bandgap, E_o, is derived by extrapolating the straight part of the curve of $(\alpha h\nu)^{\frac{1}{2}}$ against $h\nu$ to cut the $h\nu$ axis. The four groups of films described above are represented in Figs. 4.29-4.32. All the values of E_o are shown in Table 4.7.

The results for the intrinsic films show the values of 1.55 to 1.67 eV for E_o. These are somewhat smaller

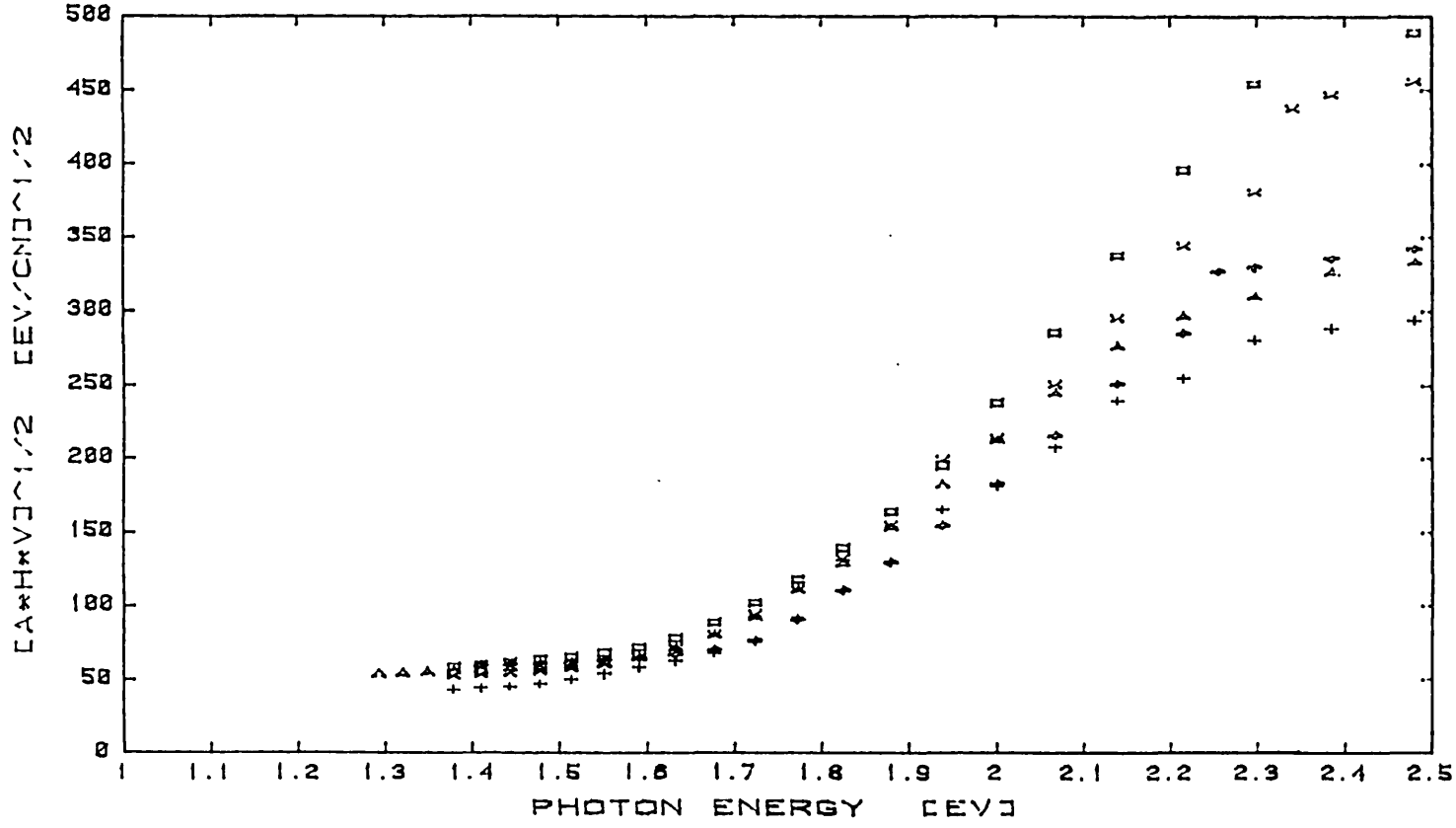

Fig. 4.29 Tauc plot for intrinsic a-Si: H.

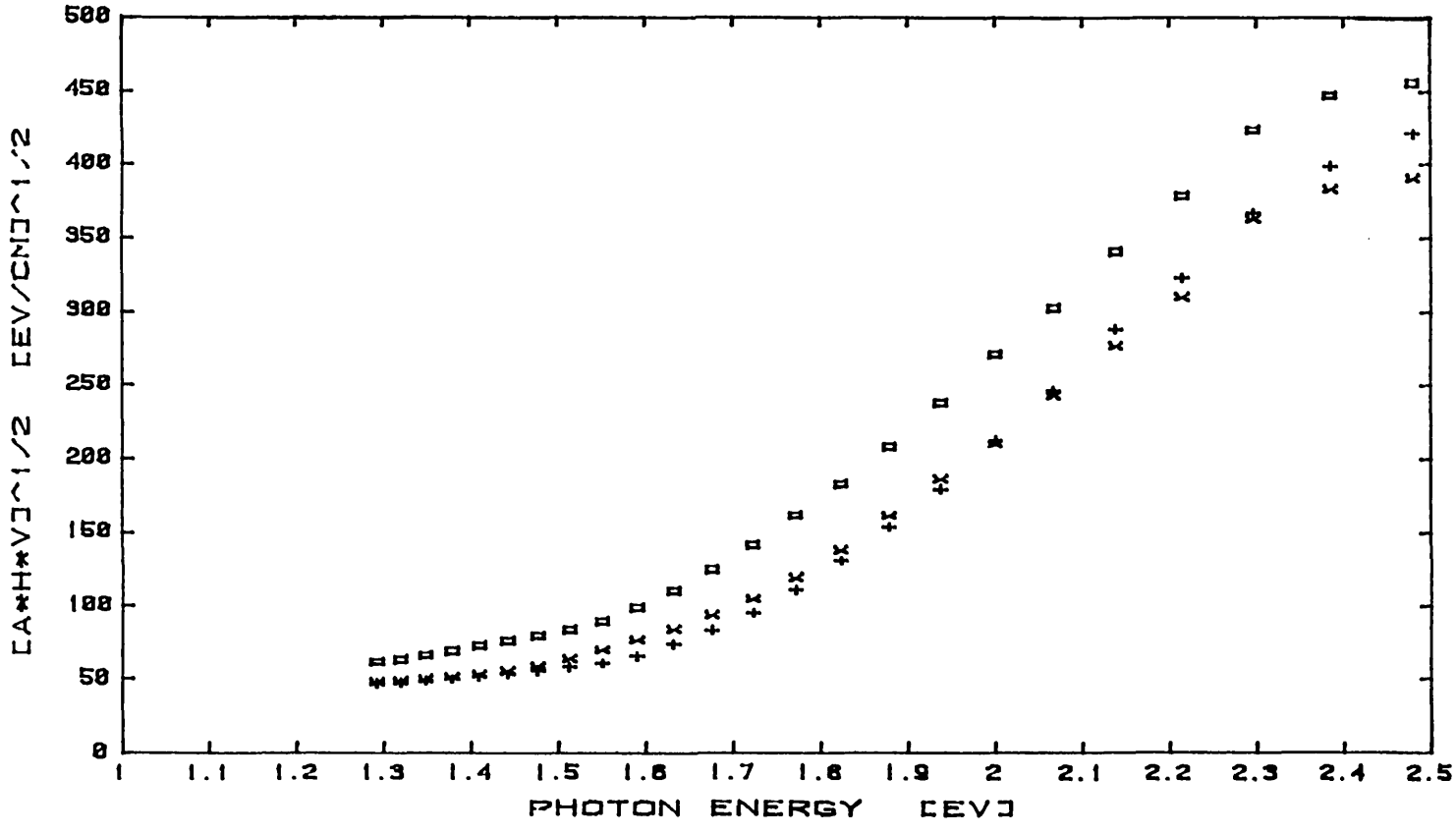

Fig. 4.30 Tauc plot for phosphrous doped a-Si: H.

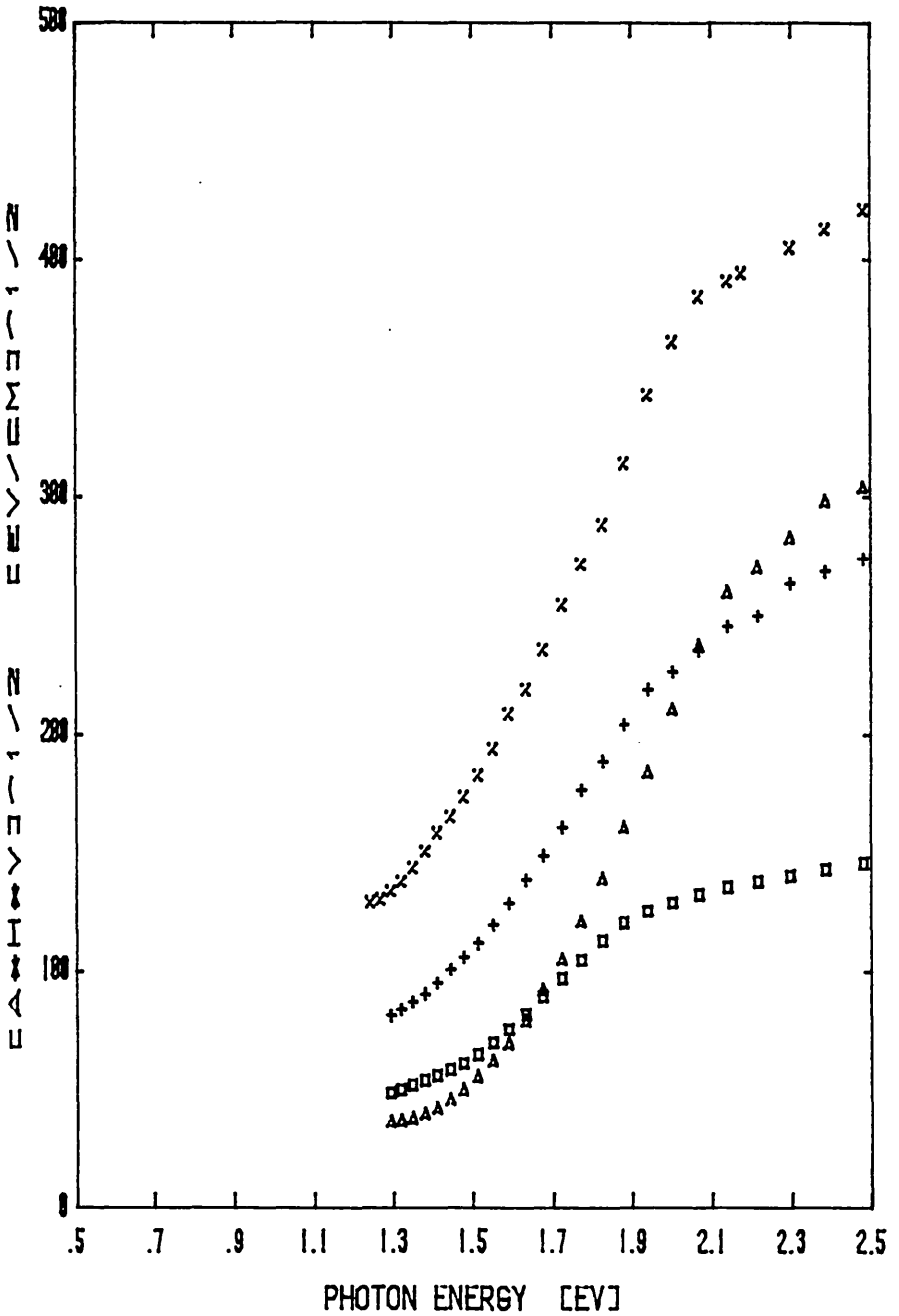

Fig. 4.31 Tauc plot for Boron doped a-Si: H.

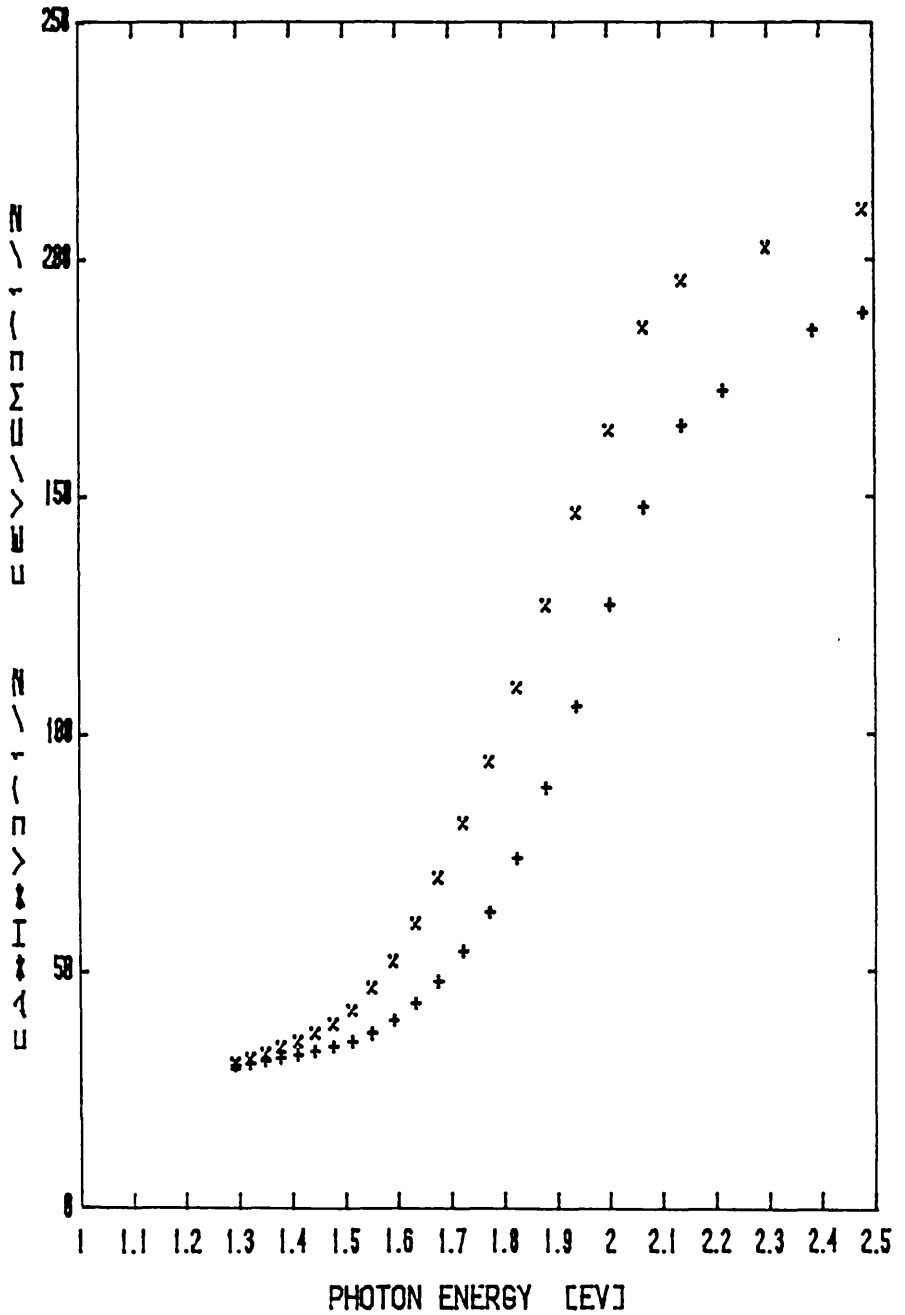

Fig. 4.32 Tauc plot for Antimony doped a-Si: H.

Sample No.	E_0(eV)	%H (Wag)	Type
RE 241	1.62	1.72	Intrinsic(I)
RE 240	1.56	0.72	I
RE 208	1.67	2.7	I
RE 209	1.62	2.08	I
RE 211	1.55	2.4	I
RE 237	1.52	0.16	N(PH)
RE 239	1.6	0.74	N
RE 236	1.49	0.17	N
RE 249	1.35	0.003	P
RE 251	1.11	_	P
RE 253	1.15	0.11	P
RE 256	1.48	1.88	P
RE 214	1.47	6.8	N(Sb)
RE 219	1.6	_	N

Table 4.7

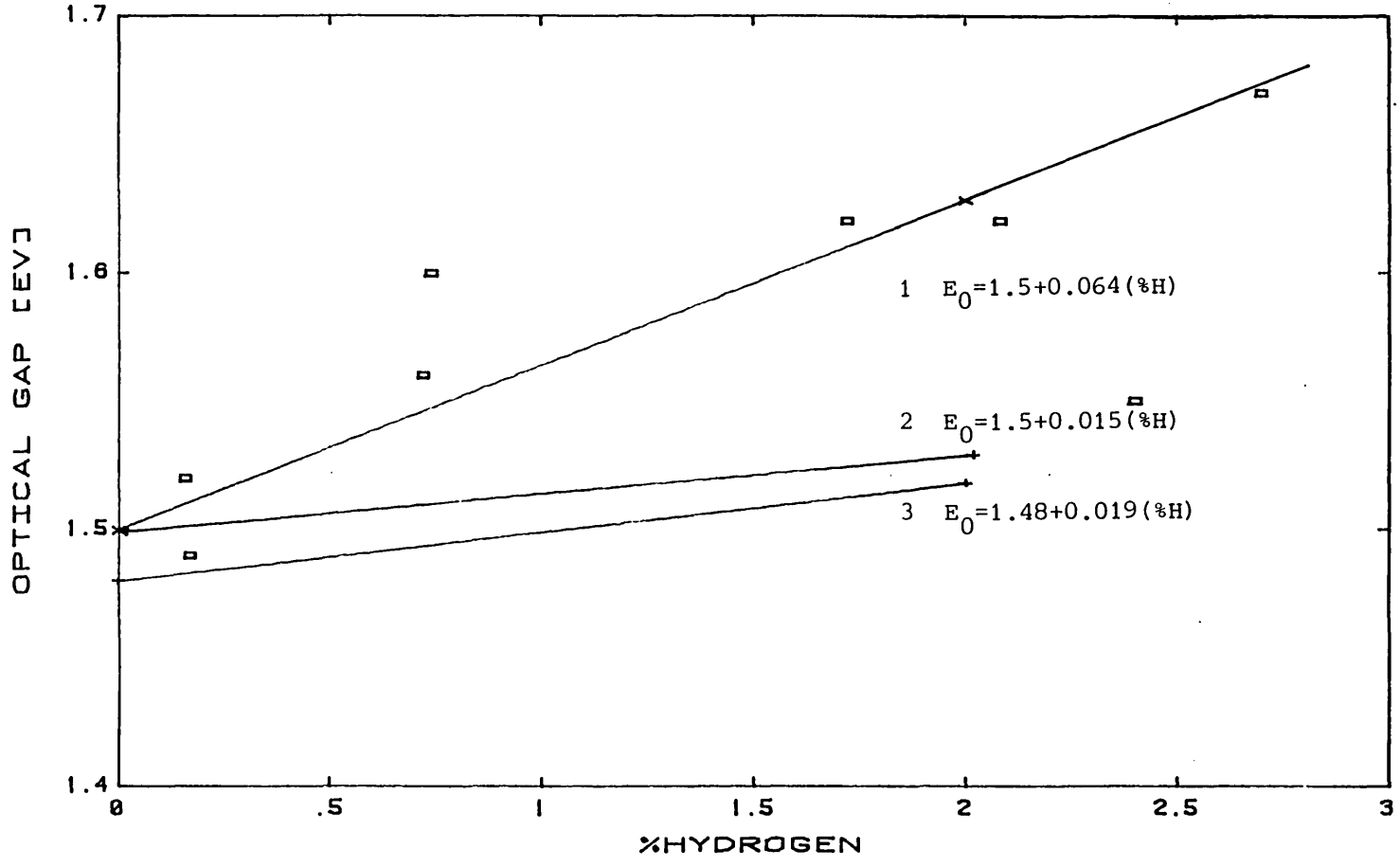

Fig. 4.33 Optical gap E_0 versus hydrogen content of a-Si: H samples.

than glow discharge films [18].

The primary source of variation in E_o is due to the hydrogen content of the specimens [18]. The valence band edge recedes with increased hydrogen content whilst the conduction band edge is relatively unaffected [18]. It is believed that the manifestation of this fact gives rise to lower E_o values in the ARE films.

Fig. 4.33 shows the plots for E_o versus the percentage hydrogen incorporation for three groups of films:

(1) ARE films from Table 4.7 which represents intrinsic and phosphorus doped films. The boron and antimony doped film data cannot be fitted into this graph. As shown on the graph, a linear relationship between E_o and %H exists; empirically it is $E_o = 1.5+0.064$ (%H).

(2) The straight line is given by $E_o = 1.5+0.015$ (%H). (after C.C. Tsai, H. Fritzsche, Sol. Energy Mat. 1, 11 (1979))[26], for glow discharge a-Si:H containing between 10 and 30 at.% of hydrogen. The films were prepared at above ~200°C.

(3) The straight line is given by $E_o = 1.48+0.019$ (%H) (after Mustada et al)[27], for films containing between 2 and 17 at.% of hydrogen. The films were prepared by reactive sputtering or glow discharge at substrate temperatures of ~300°C. This relationship also covers phosphorus and boron doped a-Si:H as well as undoped samples.

From the above graphs, to obtain a value of E_o = 1.75 eV using the ARE process would require an incorporation of only 3.9 at.%H, whereas from graph (2) 17% is required and from graph (3) 14% is required for glow-discharge and/or sputtered films.

For boron-doped films it is well known that E_o decreases with increased boron content [28], and is believed to be the result of altered plasma conditions in the presence of B_2H_6 [18].

It should be noted further that antimony doped films cannot also be included in the graph. Therefore one can assume that the plasma conditions are also altered drastically when antimony is present in the plasma. Hence the reason for the different results obtained.

4.3 MICROSTRUCTURE

The microstructure of the A.R.E. a-Si:H films was examined using an electron microscope. Fig. 4.34 shows an electron micrograph of a film of about 100 Å thick magnified 2×10^4 times. Fig. 4.35 shows the same film magnified to 2×10^5 times. In Fig. 4.36 is shown an electron diffraction pattern of the same film. The diffraction pattern shows broad rings corresponding to local ordering over one or two bond lengths. This changes to a continuous blur indicating the lack of long range order.

The average spatial separation of atoms in a solid is given by the radial distribution function J(r) and is defined in terms of the atomic density $\rho(r)$ at a distance r from any chosen atom [29]:

$$J(r) = 4\pi r^2 \rho(r) \qquad (4.10)$$

The radial distribution function (RDF) is a Fourier transform of the scattered intensity which gives a one-dimensional description of the atomic distribution [29]. Peaks in a RDF, when normalized, display the average separation between nearest neighbours, next nearest neighbours and so on.

This was carried out for the sample whose diffraction pattern is displayed in Fig. 4.36. It is assumed that the diffraction pattern is a Fourier transform of the scattered intensity from the atoms in the amorphous structure. The experimental procedure for obtaining a RDF is described below.

Fig.4.34 Electron micrograph of a film magnified to 2×10^4 times.

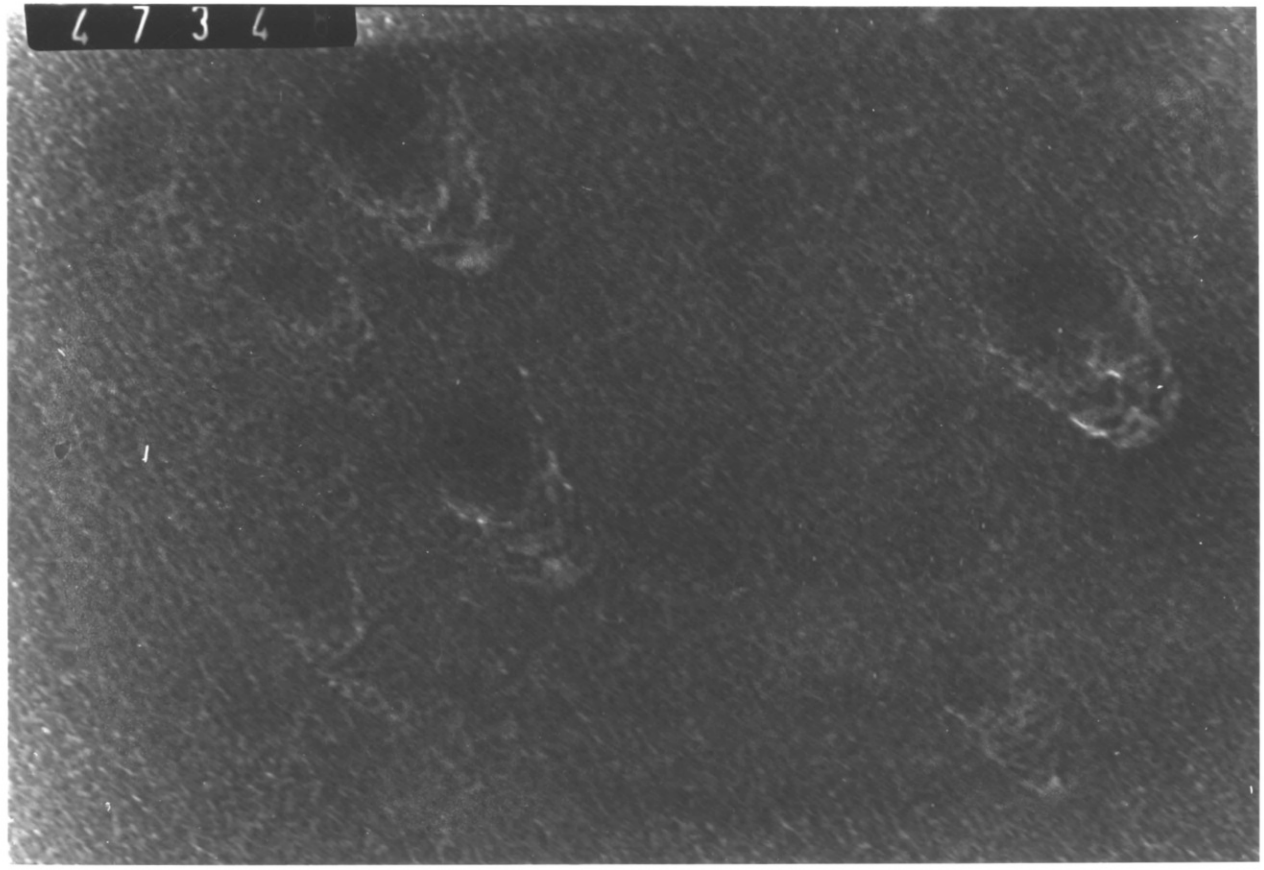

Fig.4.35 Electron micrograph of the same film of Fig.4.34 magnified to 2×10^5 times.

Fig.4.36 Electron diffraction pattern of the same film of Fig.4.34 and 4.35.

Using an optical micro densitometer (Tech/ops. Joyce Loebl) interfaced to a Data General Nova 3 mini-computer, the diffraction pattern negative was scanned in x and y directions. The intensity was scanned on a scale of 0-255 in 50 μm steps of distance.

The data was written on a 9 track 800 bits per inch (BPI) magnetic tape. This was subsequently written on a 9 track 1600 BPI tape using the main frame dual system C.D.C. Cyber 170/720 and Cyber 174 College computer for finally decoding the data on a Digital P.D.P. 11/44 using a software initially written by Dr. A. Kwabwe, Imperial College.

In Fig. 4.37 is shown a plot of intensity vs. distance across the negative of the diffraction pattern for a chord (about 7 mm off the centre). Unfortunately a scan across the centre of the diffraction pattern could not be used as the white area due to the electron microscope pointer caused saturation of the densitometer. This was unfortunate, as a plot across the diameter would have enabled the calculation of the nearest neighbour distance straight from Fig. 4.37. The distance is measured in pixels, the pixel separation being 100 μm. The intensity is on a scale of 0 to 255 grey levels.

On each half of the figure (either side of 30 pixel) there are two distinct peaks and no other distinct peaks can be observed, corresponding to nearest neighbour and next neighbour distances; confirming an amorphous structure.

Using the relationship below

$$K = D \times \ell \qquad (4.11)$$

the lattice constant, ℓ, can be calculated,

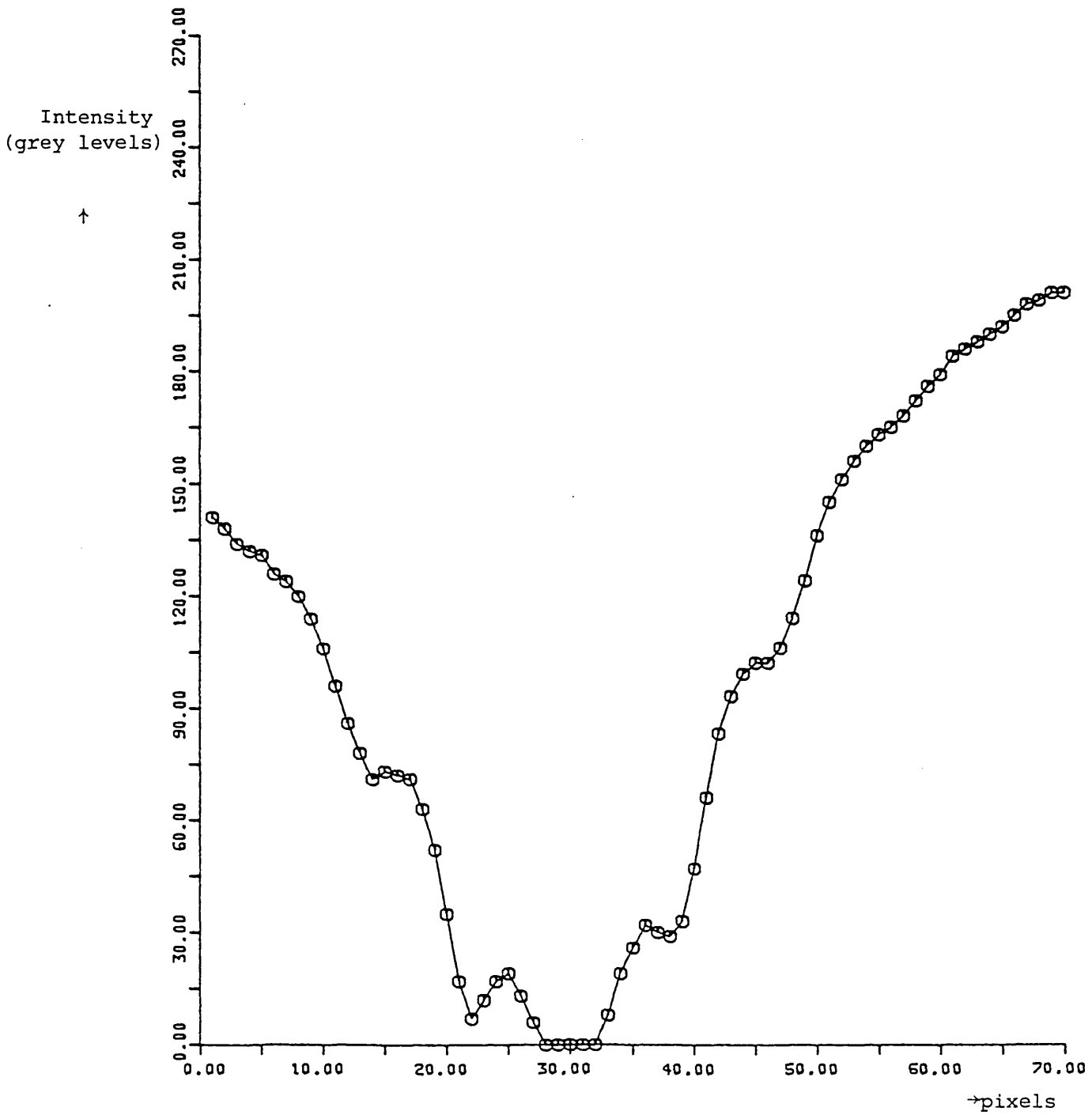

Fig. 4.37 A non-normalised RDF obtained from the electron diffraction pattern of Fig. 4.36.

where K is the camera constant of the electron microscope, which was quoted, for 100 kV, as equal to 5.19. However a variation of up to ±5% in this figure is possible according to the setting of the microscope for the specific picture taken. D is the diameter of the first ring in the diffraction pattern in centimeters, and ℓ is the lattice constant in Angstroms.

Using the diameter of the first ring on the negative to be ~2.0 cm a lattice constant of 2.59±.26 Å is obtained, which is somewhat higher than the 2.35 Å quoted by Moss and Graczyk [30]. This could possibly be accounted for by an error of ±1 mm in the measurement of the diameter of the ring and also a ±5% error in the quoted value of the camera constant.

CHAPTER 5

ELECTRICAL MEASUREMENTS

5.1 THE MEASUREMENT SYSTEM

5.1.1 Introduction

The emergence of inexpensive microcomputers has made the control, logging and data processing by computer common-place in laboratories. Most of the experiments described in this chapter were controlled by a 32 K Commodore PET 4032 microcomputer fitted with an 8 K graphics board.

The basic role of the microcomputer was to control the substrate temperature to given specifications and to collect data from specific instruments and averaging them before storing them on a floppy disk. The averaging was done by taking several readings at particular temperatures. This, in turn, improved the signal-to-noise ratio. The data was finally viewed, processed and was plotted directly using a Tektronix 4062 Interactive Digital Plotter.

5.1.2 The Cryostat

All the electrical measurements reported were performed on samples mounted in a cryostat (Fig. 5.2). This is made of stainless steel, inside the casing is a copper sample platform resting on a copper cold finger which can be cooled using liquid nitrogen. The platform has wound within it an electrically isolated Thermocoax 20 W heater filament,capable of raising the temperature of the substrate

Fig. 5.1 Photograph of Measurement Apparatus

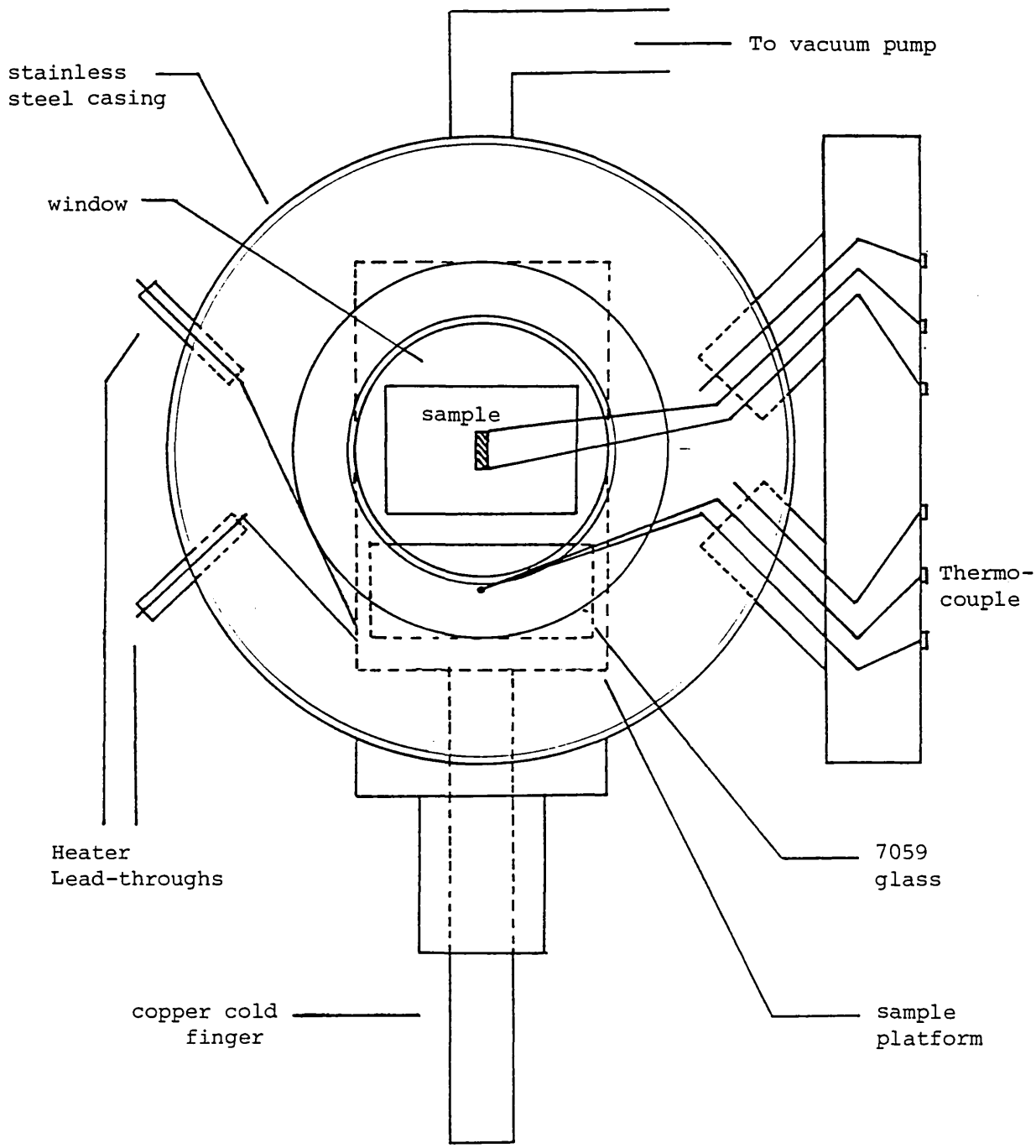

Fig. 5.2 The Cryostat

to 250°C. A minimum of -170°C is reached with liquid nitrogen cooling. The cryostat is evacuated to $\sim 10^{-4}$ torr using an Edwards EDM2 combined rotary and diffusion pump system.

The sample is mounted onto the platform using a small quantity of electrodag 915 (silver dag) and connections are made by means of thin copper wires from the sample contact pads via a 12-way lead-through to the measuring instruments. Sample temperatures are monitored with a type K thermocouple attached to a small 7059 glass slide mounted adjacent to the sample. The sample can be illuminated through a borosilicate glass window from a fibre-optic attached to a quartz-iodine tungsten light source. The lamp power could be varied by adjusting a built-in variac to give illumination of ~ 1000 W/m^2 (AM1 light).

5.1.3 Temperature Control and Data Collection

The microcomputer controls the sample temperature through a program developed by Drazin (1984) [1] by evaluating the following algorithm twice per second, concurrently with other tasks:

$$P(t) = A\int_0^t [T_t - T(t)]dt + B[T_t - T(t)]dt + C\frac{dT(t)}{dt} \qquad (5.1)$$

where P(t) is the heater power, T_t the target temperature and T(t) the measured temperature. The constants A, B, and C are chosen to give a critically damped response.

The heater power, P(t), is converted to one of 16 levels and transmitted across the IEEE 488 bus to vary the heating duty cycle using a pulse width generator. This oscillates at ~1 Hz and switches the output of a variac by means of a solid-state relay.

All d.c. current measurements are made with a Keithley 619 electrometer connected via an interface into the IEEE 488 bus. The Keithley 619 is a fully autoranging instrument and hence measurements are taken without supervision. A Fluke 415B stabilized power supply is used to provide the voltage to the sample. The temperature is monitored using a Comark 6600 thermometer connected to the computer via a Peripherial Interface Adaptor (PIA) Board. Conductivity-temperature measurements consist of a set of three points averaged at each temperature, measurements being taken at 10°C intervals. Readings are only taken if the absolute deviation in the sample temperature from the target temperature does not exceed 0.1°C.

A schematic diagram of the set-up is given in Fig. 5.3.

The standard programme for conductivity measurement and annealing is:

(1) Raise temperature of the new sample to 200°C, measuring at 10°C intervals.

(2) Anneal at 200°C for 3 hours.

(3) Cool to room temperature, measuring at 10°C intervals.

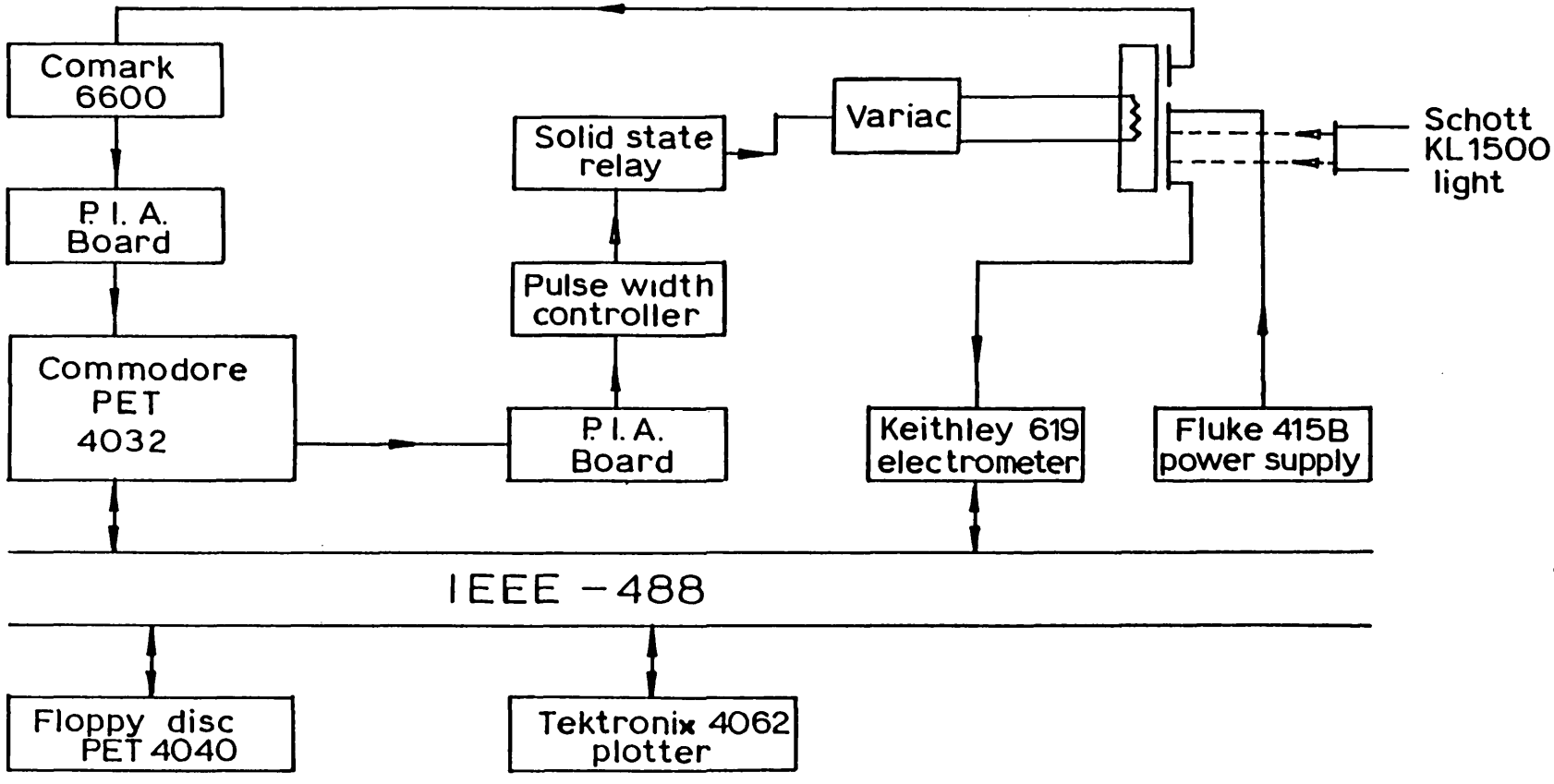

Fig. 5.3 CURRENT MEASUREMENT

(4) Heat to 200°C, measuring at 10°C intervals.

(5) Anneal at 200°C for 1 hour.

(6) Cool to room temperature, measuring at 10°C intervals.

(7) Illuminate and heat to 200°C, measuring at 20°C intervals.

(8) Cool to room temperature.

The thermal stability of the films is indicated by the extent to which the dark conductivity changes on annealing. In general, with optimised deposition conditions with bias >2000 volts negative, there was no observable change in the conductivity versus reciprocal temperature plots during the second anneal of 1 hour. The change between the preannealed state and the annealed state was also generally small. However under some deposited conditions the change of conductivity and activation energy with annealing was considerable and this behaviour was invariably associated with poor electrical and other properties. For these reasons the above annealing programme was always used and was viewed as a crude "quality control" factor.

The current-voltage relationship was normally taken before the annealing programme in order to establish that the metal/semiconductor contacts were ohmic, as evidenced by a linear current/voltage relationship. Four-probe conductivity measurements were thus considered not to be

necessary and all the measurements were carried out using two-contact geometry on coplanar samples.

5.1.4 Optimisation of Deposition Conditions

In Chapter 3 the basic problems of ideal plasma conditions were laid out. It was mentioned that for a given rate setting the efficiency of ionisation is a function of the electron velocity determined by the probe field. Experimentally, a curve of plasma current against probe voltage for a pressure of 2×10^{-2} mB and a rate setting of ~0.1 μm/min is of the form given in Fig. 5.4. From this the optimum probe voltage chosen was ~300 V.

The characteristic of the plasma current as a function of pressure is given in schematic form in Fig.5.5. The catastrophic rise in current corresponds to a plasma discharge in which a complete reaction between silicon and hydrogen occurs, forming mainly a gaseous silicon hydride and preventing deposition. It is necessary to work in the plateau region when only a partial gas-phase reaction occurs.

The deposition rate is primarily a function of the electron beam current as determined by the setting of the e-beam power supply. Using an HT voltage of 7.2 kV the e-beam filament current is in the range 0.2 to 0.26 A. Fine control is provided by a calibrated dial which sets the filament current, which is arbitrarily calibrated. A setting of 220 gives 0.2 A whilst 280 gives 0.26 A. The higher the setting, the larger the molten pool produced on the ingot and the higher the evaporation rate. The

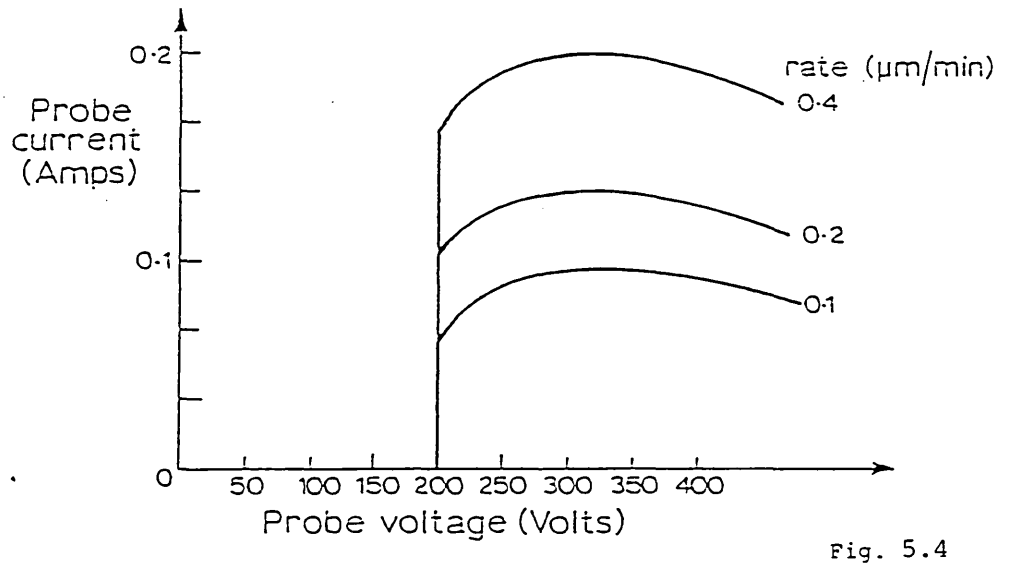

Fig. 5.4

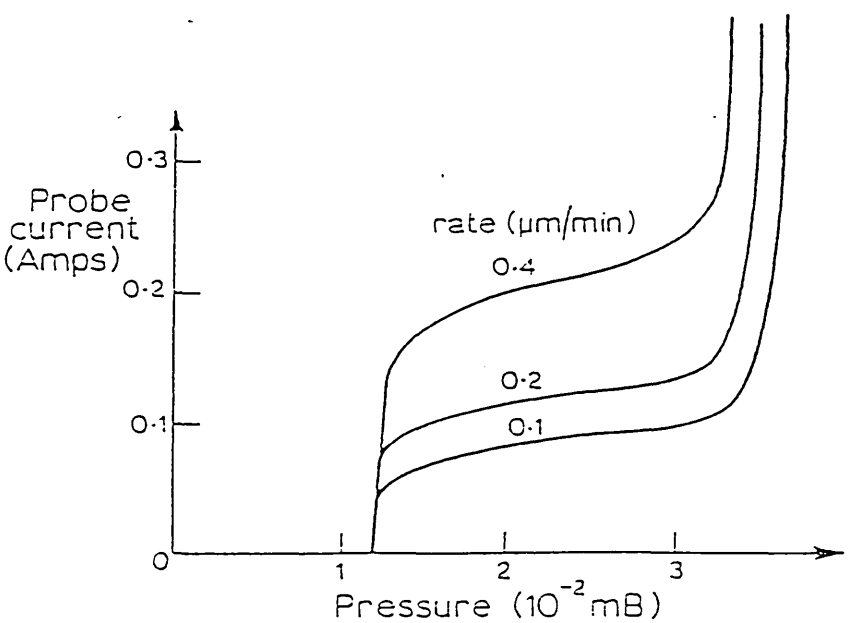

Fig. 5.5

Fig. 5.4 Plasma current as a function of voltage for fixed pressure.

Fig. 5.5 Plasma current against pressure for fixed voltage.

size of the pool should be limited to less than the 2" diameter of the ingots used; if the pool runs over the edge and contacts the cooled crucible there is a 'volcano' effect in which globules of molten silicon are sprayed into the chamber. This limits the filament current setting generally to a maximum of ~0.24 A with a dial setting of 260.

The actual primary electron beam current depends, for a given filament current setting, on the electrical conductivity of the ingot and, in particular, its area of contact with the water-cooled copper hearth. When an overflow 'volcano' has occurred the area and goodness of this electrical contact increases and a significant increase in deposition rate is observed.

A further parameter is the height of the ingot surface above the floor of the hearth. If it is too high, the primary beam tends to be partially reflected from the surface. As the ingot is reduced in height by evaporation, the electron reflection is reduced and the rate of evaporation increases. The maximum efficiency is reached at an ingot height of approximately 5/8". When the ingot surface becomes too low the rate is again reduced due to rapid heat extraction to the water-cooled hearth.

The deposition rate also depends upon the gas pressure in the chamber, higher pressures causing reduced rate due to scattering of the evaporating atoms.

Finally the deposition rate is also affected by the amount of substrate bias used, higher bias values producing lower rates, although the reduction is relatively small for bias up to -2500 V.

All these variables can be monitored simultaneously, for a given ingot, by observing the plasma current collected at the probe electrode. The plasma current, for a fixed probe voltage, gas pressure and bias is determined by the rate of evaporation. This is illustrated in Fig. 5.6 in which deposition rate is plotted against plasma current for a probe voltage of 290 V pressure 2×10^{-2} mB and bias -2500 V, where the ingot made good electrical contact with the hearth due to previous spill-over. The plasma current varied due to changes in the primary beam current setting and to the level of the ingot surface.

To overcome the problem of contact area a 3" diameter intrinsic silicon ingot was machined to a cone shape which fitted the copper hearth. This gave consistent results with the following fixed values; filament current setting 260, bias -2500 V, pressure 2×10^{-2} mB, probe voltage 290 V. The plasma current varied from 0.18 to 0.2 A during a series of depositions and the deposition rate from 0.13 to 0.14 μm/min. An increase of pressure to 2.2×10^{-2} mB with other settings the same,reduced the rate to 0.11 μm/min. The rates obtained are relatively low because the ingot height was $1\frac{1}{4}$" and because of the high resistivity of the ingot material.

In another example a 2" ingot overflowed and was subsequently used. Its surface was ~3/4" above the hearth

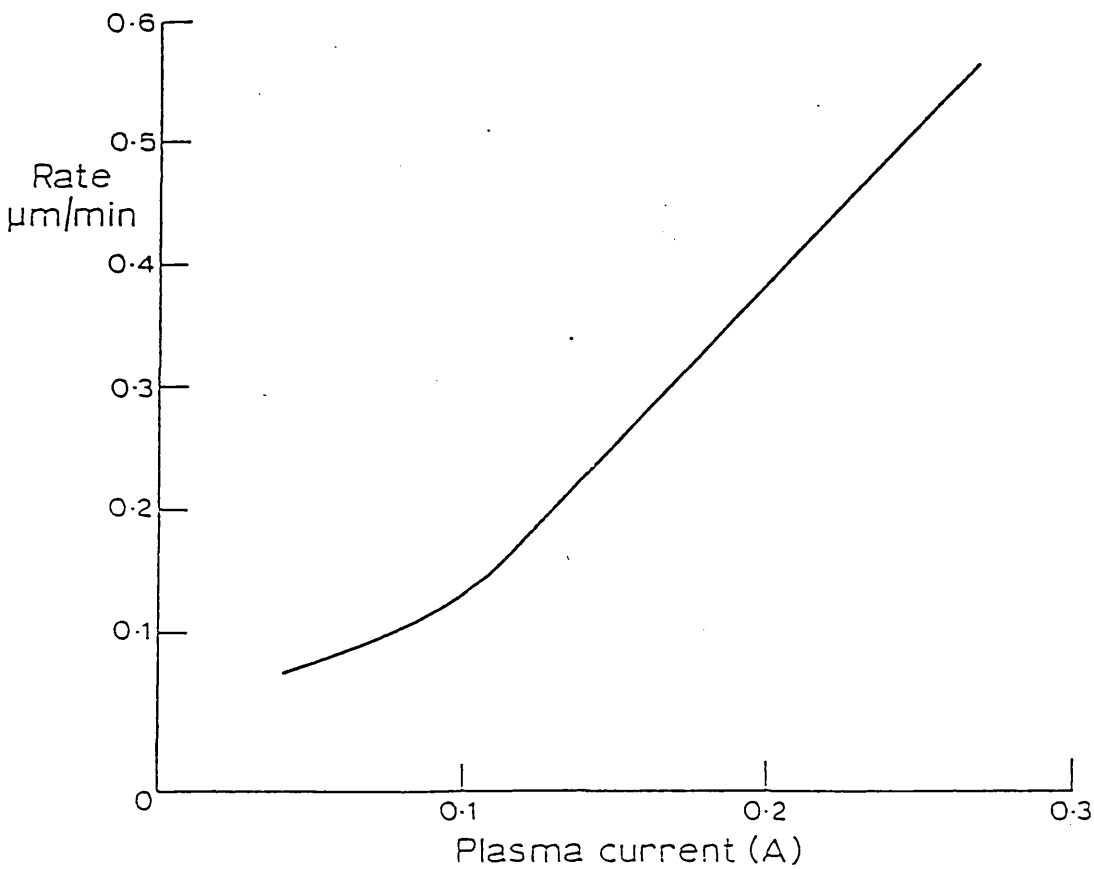

Fig. 5.6 Deposition rate as a function of plasma current for a probe voltage of 290V, pressure 2×10^{-2} mb and bias -2500V.

base and it made excellent electrical contact. With a filament current setting of 260 and other conditions as above, a plasma current of 0.22 A was obtained with a deposition rate of 0.52 μm/min.

For production, ingots should be machined to fit snugly into the hearth and should have the optimum height. It will be necessary to provide deposition rate control using a crystal monitor to control the primary electron beam current.

5.2 D.C. CONDUCTIVITY AND PHOTOCONDUCTIVITY OF INTRINSIC FILMS

The best quality of "intrinsic" film was taken to be that with the lowest dark conductivity at room temperature (21°C), and the highest photoconductive ratio given by

$$\text{p.c.r.} = \frac{\text{conductivity in AM1 light}}{\text{conductivity in dark}}$$

at room temperature ($1/T = 3.4 \times 10^{-3}\ °K^{-1}$)

Over the course of this work the deposition parameters varied were: probe voltage, hydrogen pressure, various mixtures of hydrogen and argon, deposition rate, substrate temperature and bias (zero, positive d.c., negative d.c., self bias, r.f. negative). The optimum probe voltage and pressure for a given setting of primary beam power and zero bias were taken to be the values which gave the highest plasma current, corresponding to the highest ionisation efficiency. For the physical configuration used,

Bias(volts)	P.C.R.
0	110
-150	1.36×10^3
-920	7×10^3
-2000	9.4×10^3
-2420	1.33×10^4
-2500	7.8×10^4
-2500	1.4×10^5

Table 5.1

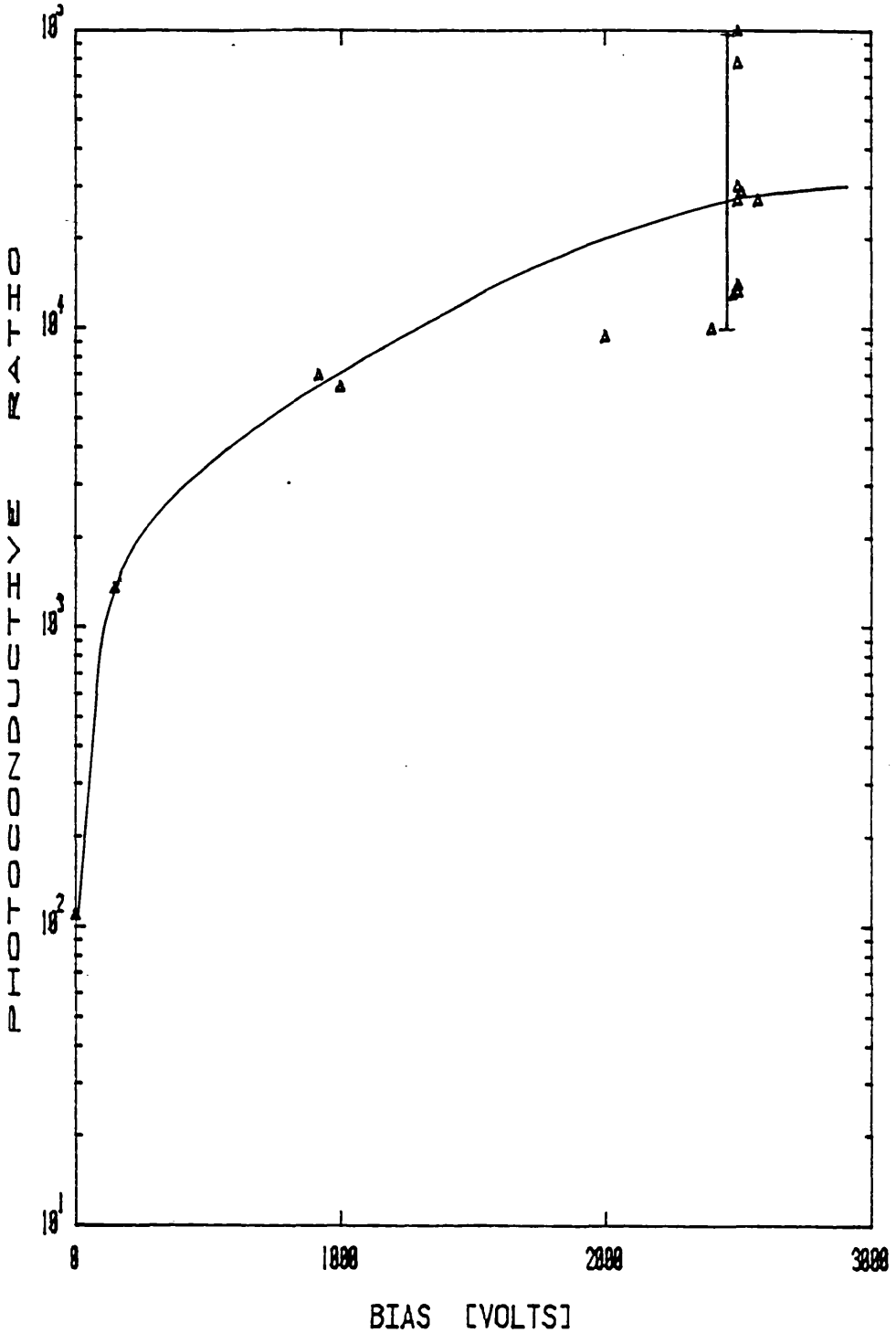

Fig. 5.7 P.C.R. as a function of bias

these were found to be probe voltage ~300 V positive, pressure ~2 x 10^{-2} mB (pure hydrogen) (see Chapter 3, section 7.1). Using these values it was found that the best films were produced with a substrate bias of >2000 V negative. The standard bias used was ~2500 V negative, corresponding to the maximum r.f. power available. The effect of bias is shown in Table 5.1 for a set of films prepared with substrate temperature ≈250°C, pressure ~2 x 10^{-2} mB and probe voltage 290 V. Fig. 5.7 shows a plot of the variation of p.c.r. with applied bias between 0 V and -2500 V. Within the first one hundred volts the p.c.r. increases by an order of magnitude from 10^2 to 10^3 and thereafter the curve flattens out. The error-bar shows the spread of the maximum p.c.r. at -2500 V, the minimum value being ~1 x 10^4 and the maximum ~1 x 10^5.

It will be seen from Table 5.1 that the rate of deposition varied from one run to the next. As pointed out earlier the rate depends on a number of factors, not all of which are well-controlled. It is believed that it is variation of deposition rate which is principally responsible for the spread in conductivity and p.c.r. observed in films deposited under nominally similar conditions. Accurate control of deposition rate using a crystal rate monitor would be highly desirable.

5.2.1 Non-Optimised Films

Only a brief discussion of these films is presented here. In Fig. 5.8 is shown the conductivity/temperature curve for films prepared under non-optimised conditions. On

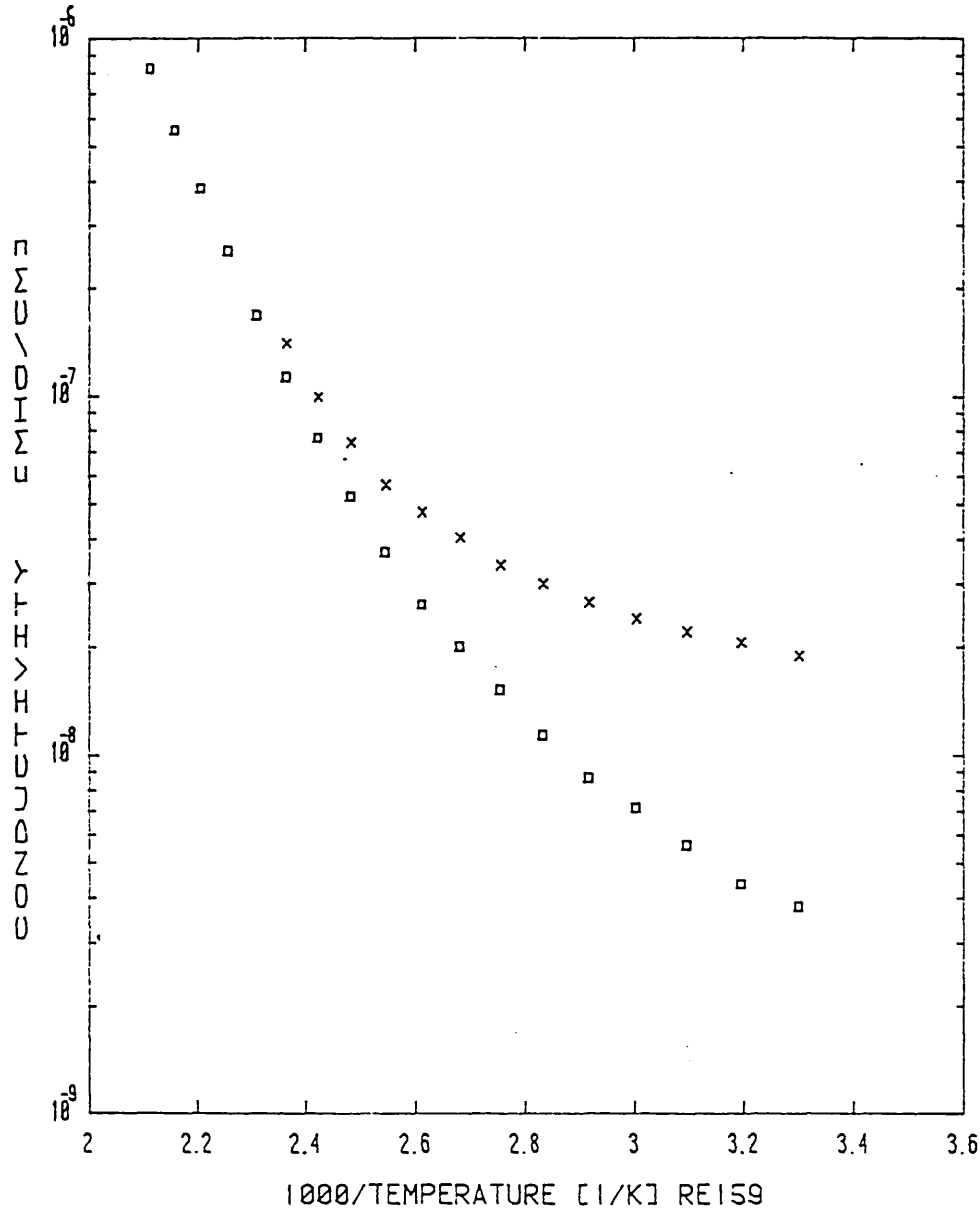

Fig. 5.8 Dark and Photoconductivity vs.1000/Temperature for a non-optimised film.

the activation plot of log conductivity versus 1/Temperature, it is apparent that hopping conductivity is dominant even at room temperature [2]. This is a property associated with a very large number of states at the Fermi level, often observed in elemental evaporated a-Si. The p.c.r. is less than an order of magnitude, indicating a large number of trapping centres.

This particular film was prepared using a probe voltage of +400 V, substrate bias of ~-1500 V, pure hydrogen atmosphere with pressure of 1 x 10^{-2} mB, HT voltage of 6.6 kV for the primary e-beam. The deposition rate for the above parameters was 0.046 μm/min.

In Fig. 5.9 is shown the effect of incorporating some argon during the deposition under various non-optimised conditions (pressure of ~2 x 10^{-2} mB and temperature ~250°C being kept constant). The curves A, B, C and D are plots of dark conductivity versus 1/temperature; A/Li and B/Li are those corresponding to curves A and B respectively under illumination.

Curve A represents a film prepared with 50% hydrogen and 50% argon mixtures using zero probe voltage and a substrate bias of -2500 V. It was possible to sustain a plasma without having to accelerate the primary electrons, using a probe voltage, due to the low ionisation potential of argon and the presence of the bias field. Curve A is not singly activated and shows evidence of tail state hopping [3] but no hopping at Fermi level is indicated above room temperature. A relatively low state density at the

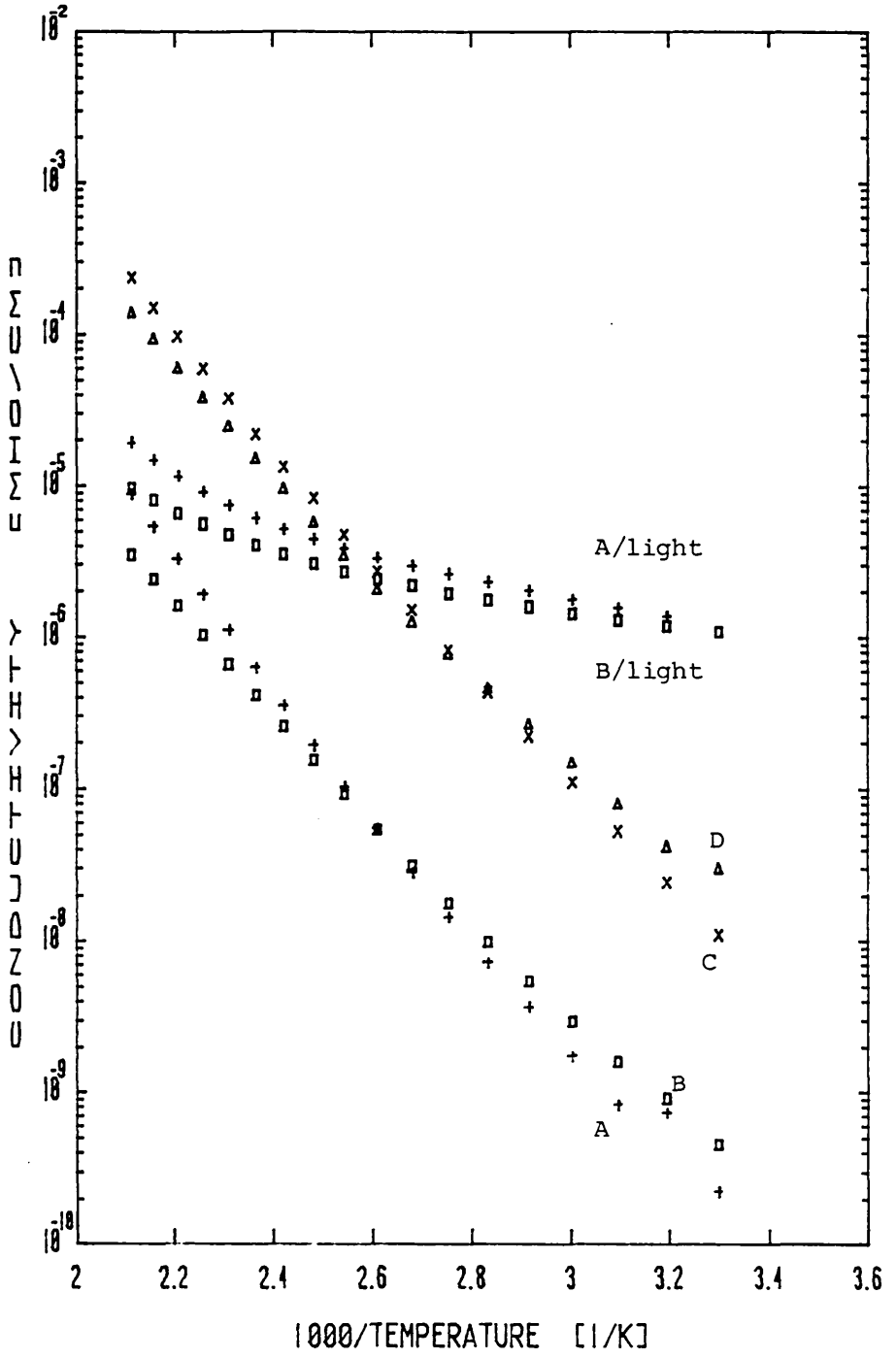

Fig. 5.9 Dark conductivity vs.1/temperature for various deposition conditions using argon and hydrogen mixtures.

Fermi level is further substantiated by the moderately high p.c.r. value of ~10^4.

Curve B is representative of a film prepared using 66% argon with a probe voltage setting of 160 V and a substrate bias of -2000 V; again tail state hopping is indicated by the variation activation energy at low temperature and the high temperature activation energy is lower compared with curve A. The p.c.r. is $< 3 \times 10^3$ (see curve B/Li). The addition of a probe voltage increases the ionisation efficiency and there are therefore more +ve argon ions available to bombard the biassed film during growth. This should lead to more incorporation of argon in the film which is known to introduce more defect states [4].

Both curves C and D represent films prepared with 50% argon, and a probe voltage of 160 V. Sample C had a substrate bias of -100 V (r.f.) and sample D had a substrate bias of +108 V (d.c.). Both these films had p.c.r. of less than one order of magnitude and a relatively high conductivity in the dark. Again the curves are not singly activated. These features indicate a large density of gap states. It should be noted that 160 V is not a sufficient probe electrode voltage to produce a plasma in pure hydrogen. The fact that a plasma is obtained is due to the presence of the argon. Keeping the positive ions away from the substrate with a positive voltage produces a film with lower activation energy and higher conductivity than is the case for a small negative bias. The low negative bias produces

a mild bombardment of the growing film which increases the activation energy and lowers the conductivity. These results show that bombardment of the growing film by positive ions improves film quality, but if the ions include argon, high negative bias produces argon-induced defects in the film.

5.2.2 Optimised Intrinsic Films

Using optimum values for deposition conditions mentioned earlier, intrinsic films were deposited (see Table 5.2 (repeat of Table 4.2) and Table 5.3). Each film was subjected to the anneal cycle mentioned in section 5.1.3.

In Figs. 5.10 to 5.14 are shown the anneal cycles of each film and the photoconductivity versus 1/temperature for the fully annealed films. In Figs. 5.10, 5.11 and 5.12 it can be seen that the anneal does not produce a signfiicant change in the dark conductivity as function of temperature. The up and down cycles almost superimpose in each case. The slopes are all singly activated. The activation energies can be found in Tables 5.2 and 5.3.

All three samples contain about 2% hydrogen (calculated from the I.R. wag mode). It is suggested that the structure is highly co-ordinated and the density of dangling bonds is relatively low, there is low concentration of clusters of atomic hydrogen trapped in the structure and therefore annealing does not reorganise the film structure to any great extent.

Sample No.	Ingot Type	Rate um/min	Thickness um	H Flow sccm	Pressure mb	Bias volts	r.f.Power watt	Probe Volt	H(W) %	H(S) %	Room Temp. Cond. $(\Omega cm)^{-1}$	E_σ eV	P.C.R.
195	0.002n	.115	.525	45	1.8×10^{-2}	-2400	350	290	5.16	1.52	1×10^{-10}	.84	1×10^{4}
209	12p	.16	.8	50	1.2×10^{-2}	-2577	380	310	2.08	1.87	3×10^{-11}	.77	2.7×10^{4}
211	12p	.16	.82	52	1.5×10^{-2}	-2500	350	320	2.4	0.4	3.7×10^{-11}	.79	7.8×10^{4}
213	12p	.24	1.2	52	1.3×10^{-2}	-2500	350	310	19.6	2.28	7×10^{-12}	.87	3×10^{4}
240	Int	.14	.7	60	2.0×10^{-2}	-2420	365	300	0.72	0.72	9×10^{-11}	.77	1.33×10^{4}
241	12p	.10	.6	60	2.0×10^{-2}	-2514	380	290	1.72	1.3	3.5×10^{-10}	.73	2.86×10^{4}

Table 5.2

Sample No.	Ingot Type	Rate um/min	Thickness um	H Flow sccm	Pressure mb	Bias volts	r.f.Power watt	Probe Volt	H(W) %	H(S) %	Room Temp. Cond. (Ωcm)$^{-1}$	E eV	P.C.R.
123	20p	.15	.74	43	1.8×10^{-2}	1000	350	400	5	-	1×10^{-10}	.83	6.4×10^{3}
125	20p	.18	.9	44	2.0×10^{-2}	2000	350	400	.33	-	1.7×10^{-11}	.92	9.4×10^{3}
207	12p	.16	.8	50	1.2×10^{-2}	2500	380	310	2.08	1.87	2.3×10^{-10}	.76	7.4×10^{3}
247	.014p	.19	.95	60	2.0×10^{-2}	2482	360	290	1.1	.05	9.5×10^{-11}	.69	1.3×10^{4}
257	.014p	.16	.8	60	2.0×10^{-2}	2500	380	290	1	.78	1.0×10^{-12}	.77	1.4×10^{5}

Table 5.3

However, in Figs. 5.13 and 5.14 are shown two samples containing 5.16% and 19.6% of hydrogen respectively. The p.c.r. for both films is $>10^4$ and they are both singly activated above room temperature. The striking difference is the lower room temperature conductivity and higher activation energy after each subsequent anneal. Unlike Figs. 5.10, 5.11 and 5.12 the up and down cycles are not superimposed upon each other. This would be consistent with restructuring of the silicon and hydrogen bonds and also evolution of non-bonded hydrogen and perhaps even restructuring of clusters of hydrogen trapped in the amorphous structure.

It can, therefore, be concluded that, ARE films with lower concentrations (~2%) of hydrogen show greater thermal stability than films with greater concentrations of hydrogen.

In Fig. 5.15 is shown a plot of p.c.r. versus percentage hydrogen concentration for the intrinsic films in Tables 5.1 and 5.2. It shows a sharp increase in the p.c.r. for very small amounts of hydrogen incorporation. The p.c.r. rises steadily with increased hydrogen concentration to a maximum value, for about 2.5 to 3% hydrogen. It then decreases and flattens off to a value of $\sim 10^4$ for much higher hydrogen concentrations.

Similar behaviour has been reported by Moustakas et al. [5] and Anderson et al [6] for sputtered films. In their samples, however, the drop in the photoconductivity occurred at about 6 atomic percent of hydrogen.

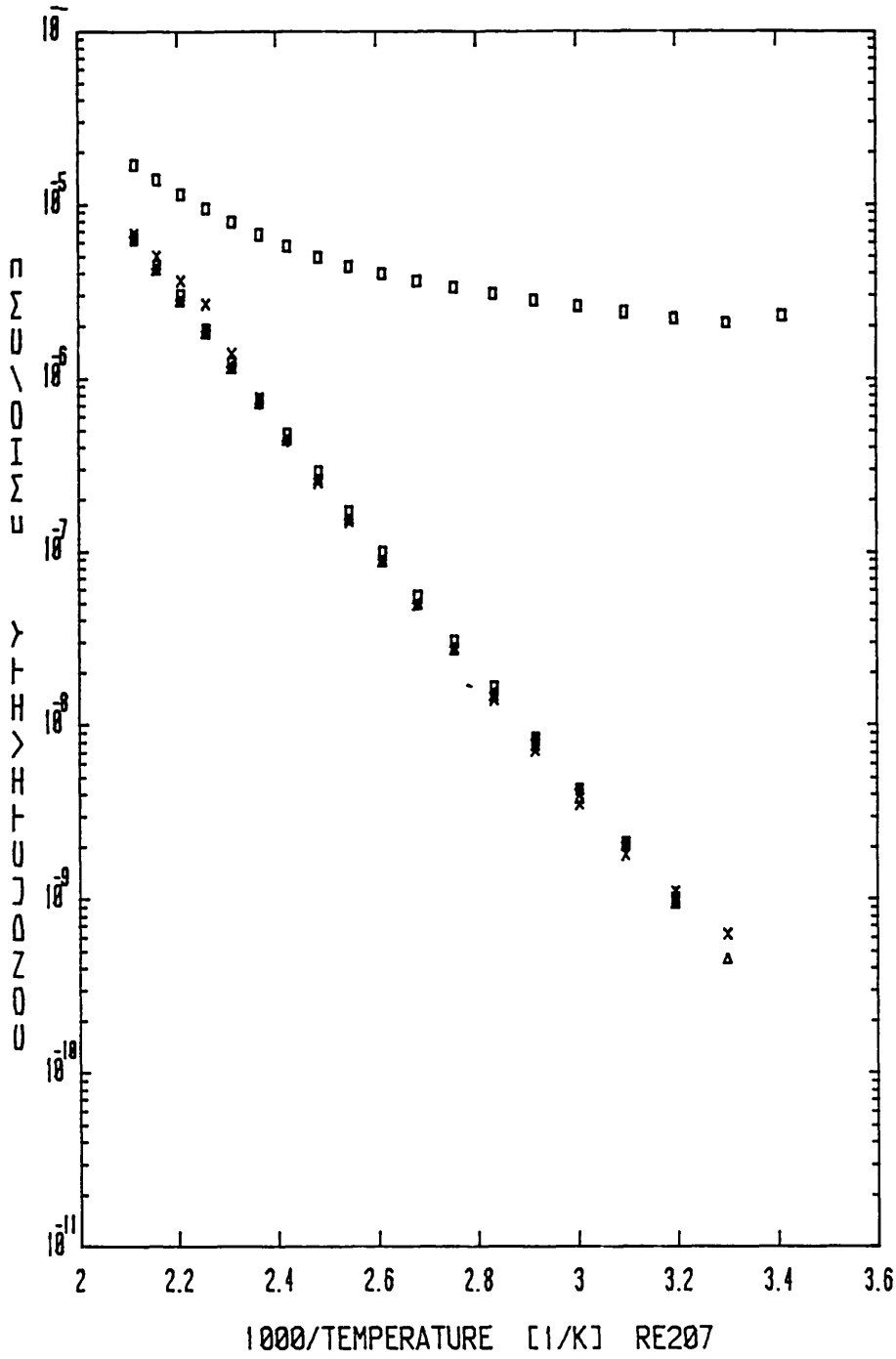

Fig. 5.10 Figures 5.10 to 5.14 show dark and photo-conductivity vs .1000/temperature for complete anneal cycles of some optimised films.

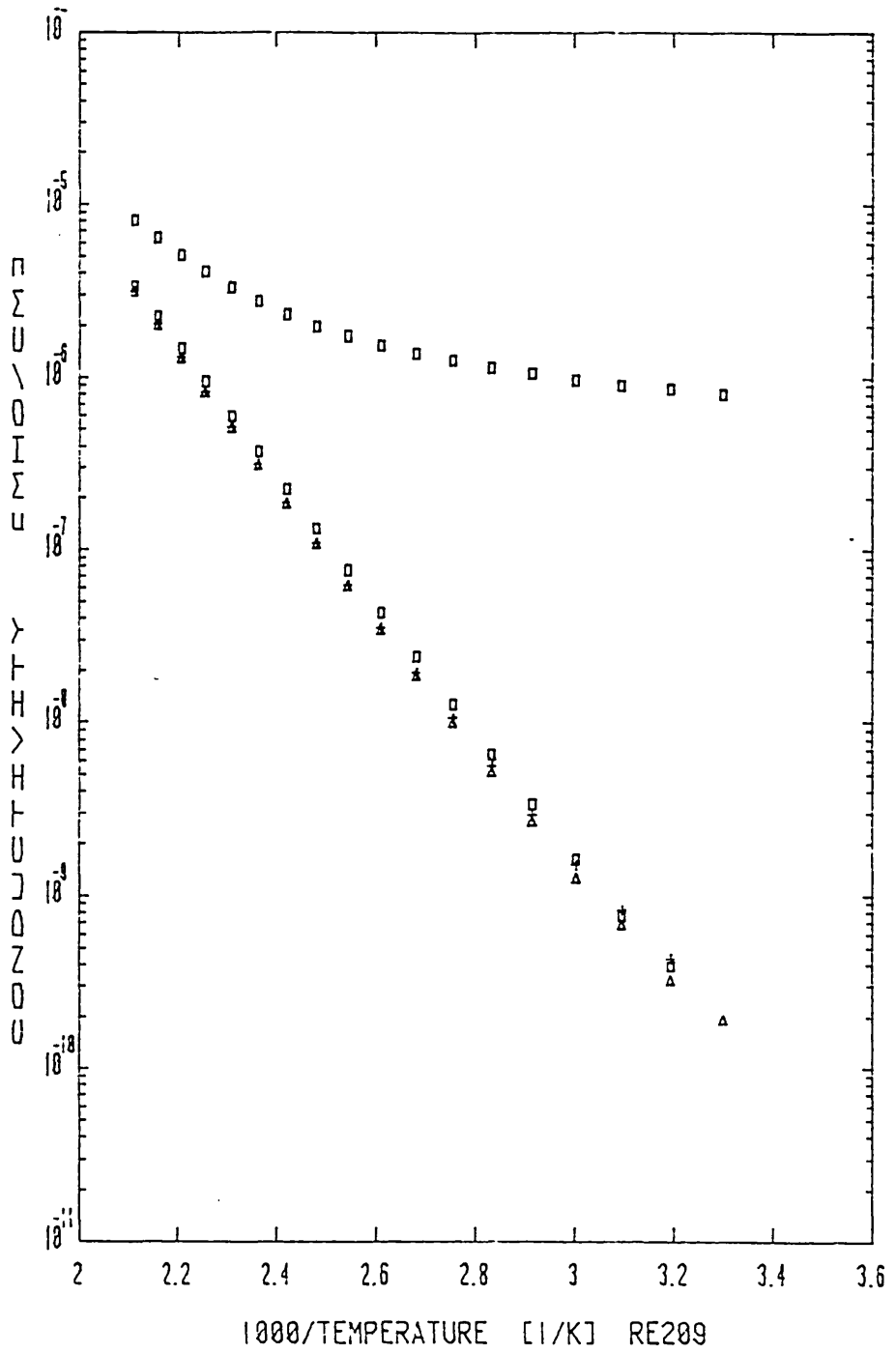
CONDUCTANCE (MHO)
MEASURED
2
2.2
2.4
2.6
2.8
3
3.2
3.4
3.6
1000/TEMPERATURE [1/K] RE209

Fig. 5.11

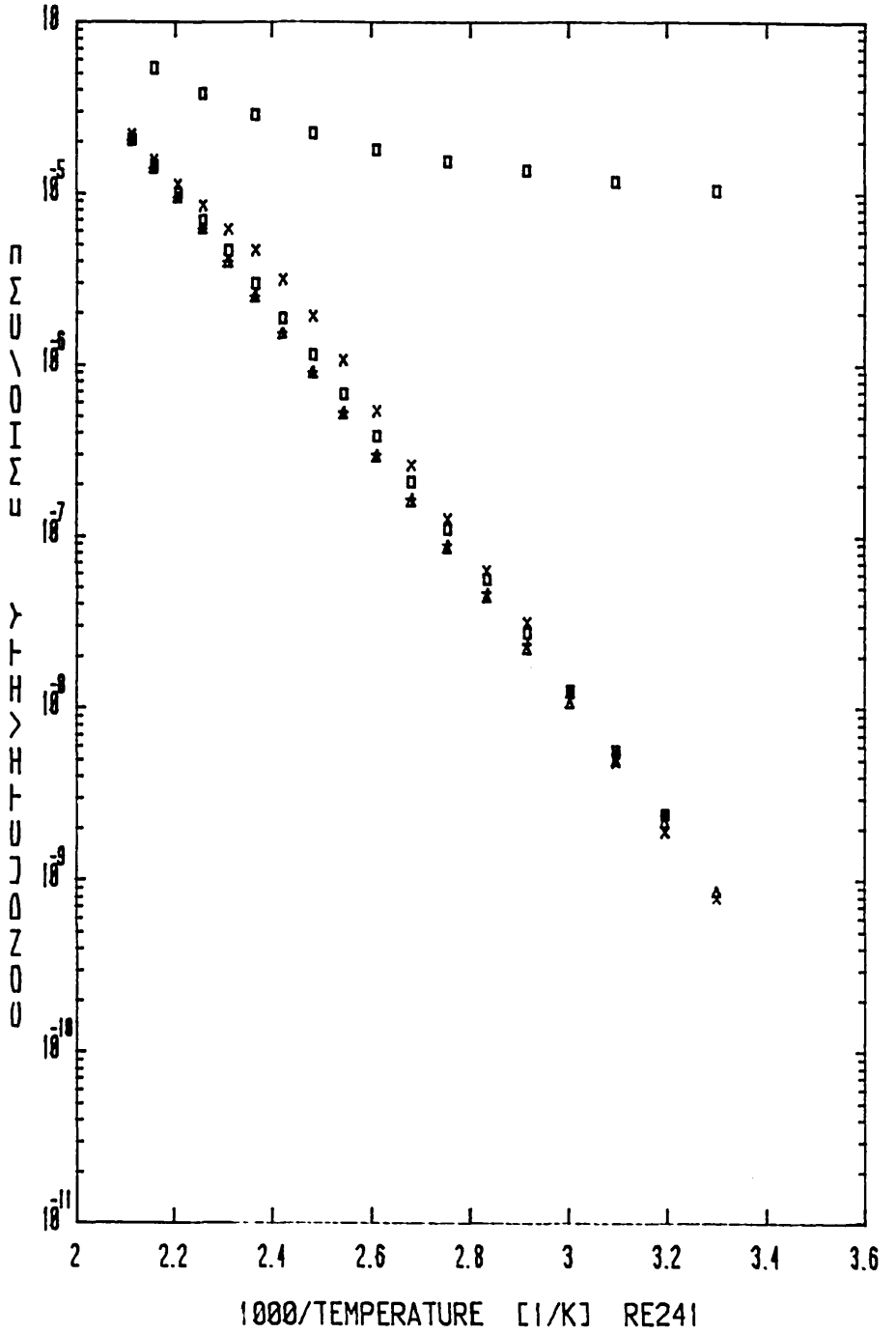
CONDUCTANCE \ OHM
EMISSION
2
2.2
2.4
2.6
2.8
3
3.2
3.4
3.6
1000/TEMPERATURE [1/K] RE241

Fig. 5.12

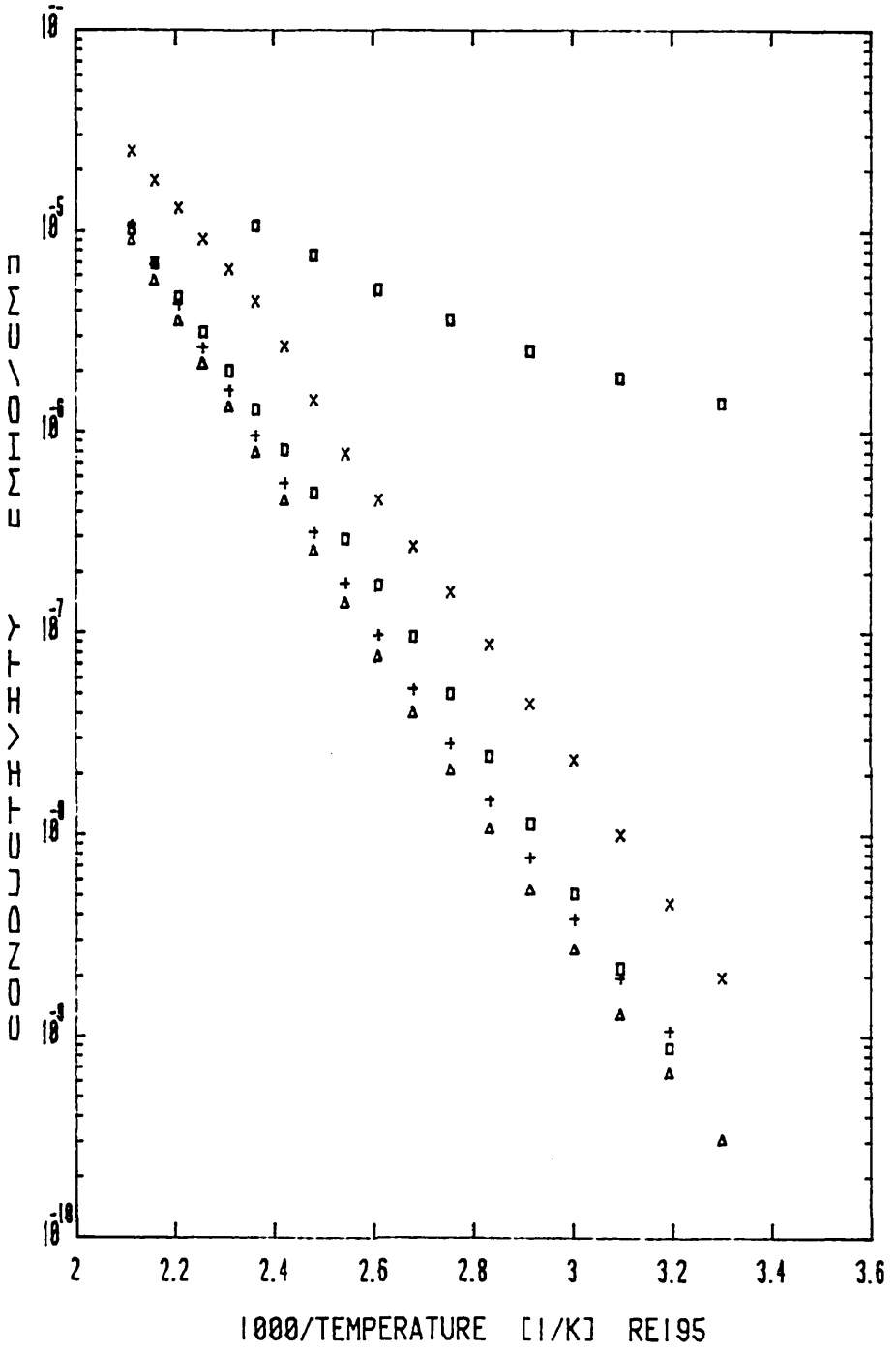
10^-4
10^-5
10^-6
10^-7
10^-8
10^-9
10^-10
2
2.2
2.4
2.6
2.8
3
3.2
3.4
3.6
1000/TEMPERATURE [1/K] RE195

Fig. 5.13

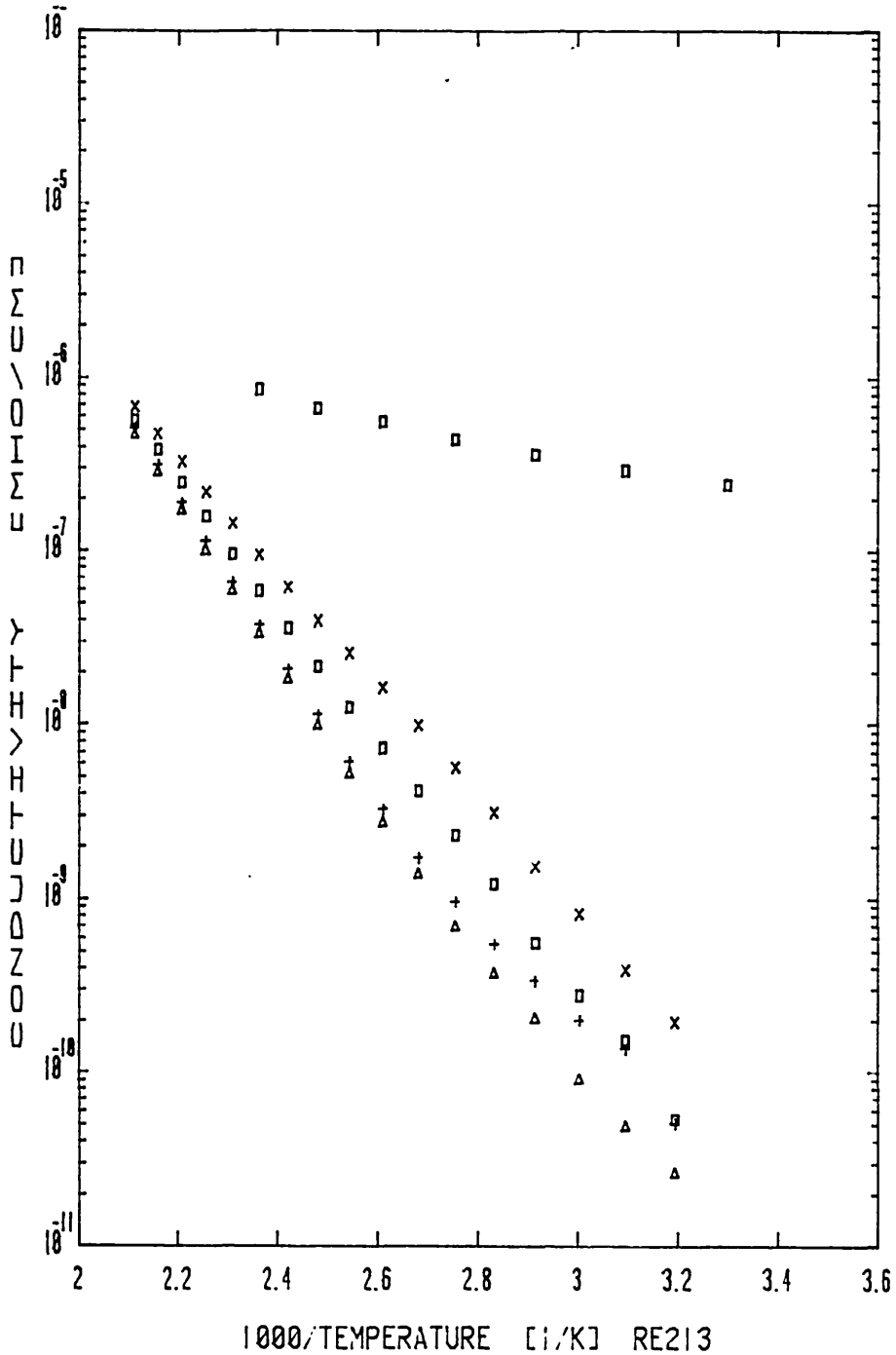
10^-4
10^-5
10^-6
10^-7
10^-8
10^-9
10^-10
10^-11
2
2.2
2.4
2.6
2.8
3
3.2
3.4
3.6
1000/TEMPERATURE [1/K] RE213

Fig. 5.14

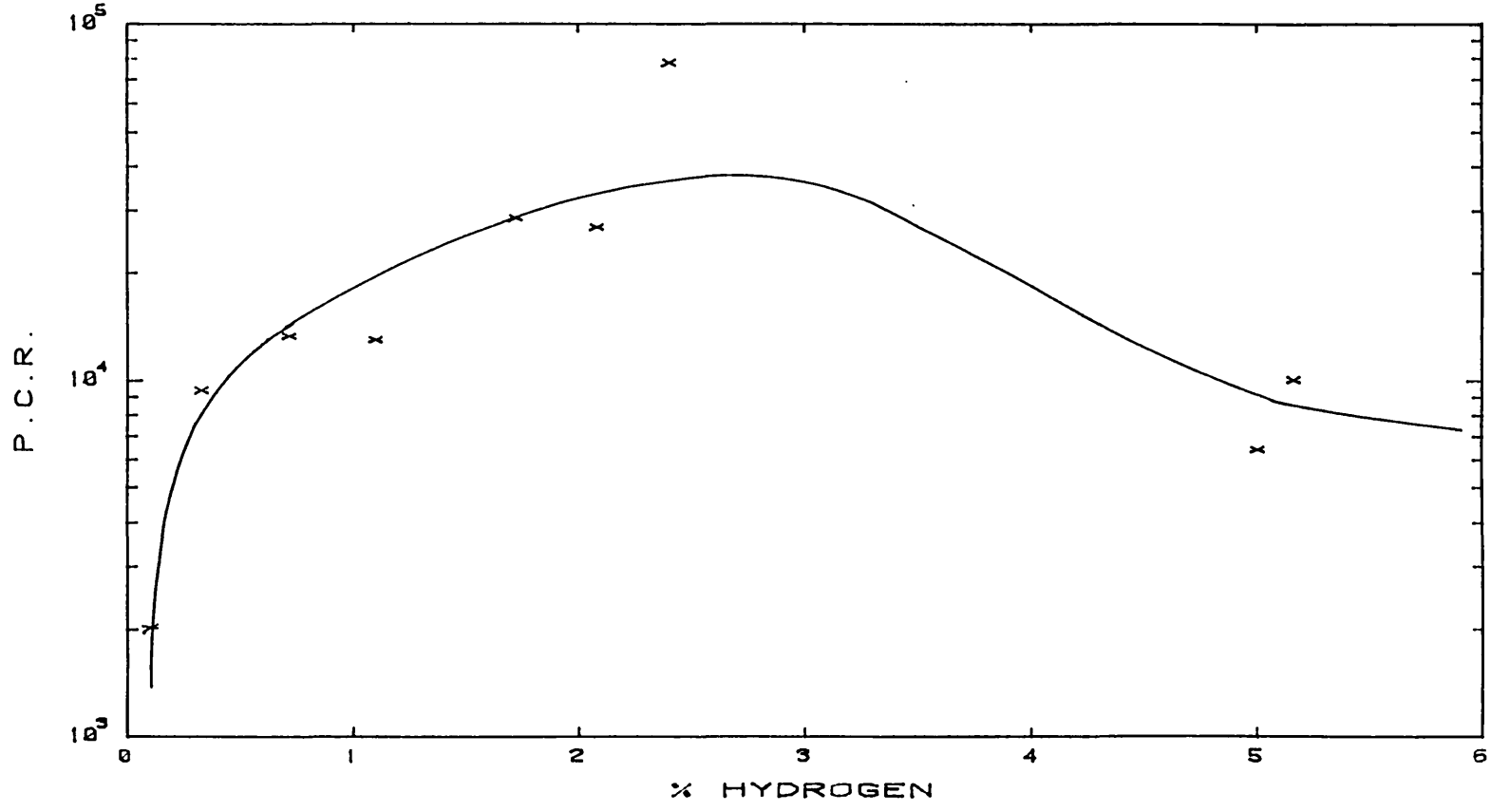

Fig. 5.15 P.C.R. as a function of percentage hydrogen incorporation.

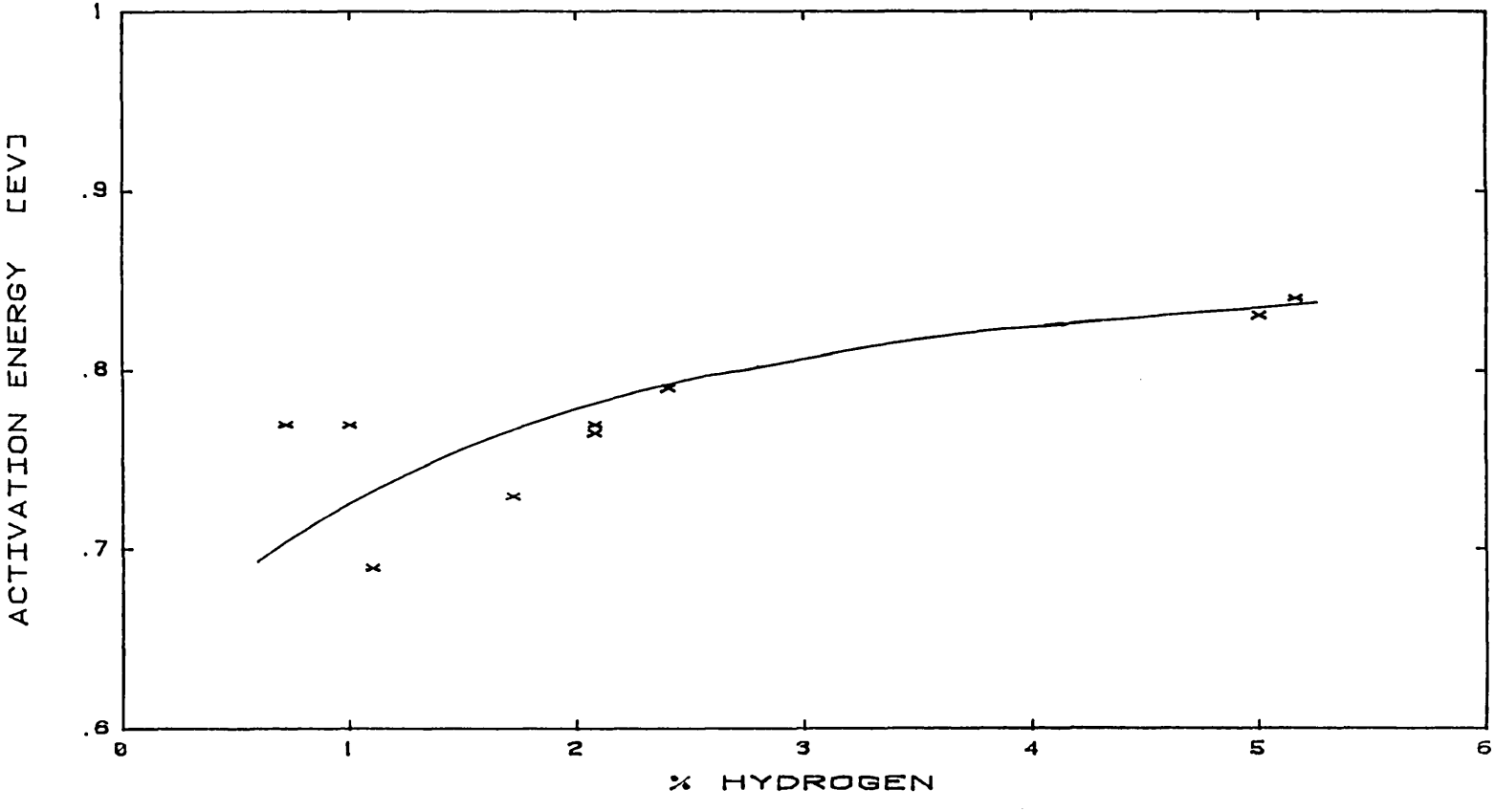

Fig. 5.16 Activation energy as a function of percentage hydrogen incorporation.

In Fig. 5.16 is shown the variation of activation energy of intrinsic films with hydrogen concentration. The activation energy shows a slow increase with increased hydrogen up to a value of 0.87 eV for ~19% hydrogen. In glow discharge materials often activation energies of up to 1.0 eV are found [7,8] and are, perhaps, a manifestation of the very large quantities of hydrogen present in the samples. The increase in the activation energy with increase in hydrogen concentration has been reported by Anderson and Paul [9] in sputtered materials. In their samples, the activation energy increases from 0.7 eV to 0.9 eV for partial pressure of hydrogen of about 0.1 m torr to 1 m torr during deposition. This value decreases slightly as the hydrogen partial pressure is increased to 5 m torr.

The above results suggest that,in biassed ARE films, the dangling bond density is minimised by hydrogen incorporation at much lower hydrogen content than is the case with GD or sputtered films.

5.2.3 Staebler-Wronski Effect

In glow discharge films it is normally found that the dark conductivity decreases and the activation energy increases, from the values obtained in the as-prepared state, when the film is illuminated for a period at room temperature. The original conductivity and the activation energy are recovered after annealing the film in the dark above 150°C. This is called the Staebler-Wronski (SWE) effect, [10,11]. There is concern that this effect might result in solar cell degradation under prolonged illumination. Although the SWE

has been known for some years its nature remains unclear. Its origin was initially thought to be due to surface band bending [12]. On the other hand, there is much evidence to suggest that this is not the case [11,13,14, 15], but rather that it is a bulk effect. Nevertheless the microscopic mechanisms responsible for the bulk effect have not yet been identified. Irsigler et al [16], suggest,on the basis of comparison of the quantitative values observed for the SWE by different authors, that it is strongly dependent on the deposition process parameters. Staebler and Wronski [17] observed that there was no change in the optical properties of a-Si:H during illumination, so there is no gross photostructural or photo-chemical change in the material. There is also a reduction in the photoconductivity, which indicates an increase in either the number or the cross-section of recombination centres and may be accounted for by photocreation of deep defect centres in the material. This provides an explanation of the observed experimental results, but the specific mechanism by which these defects are created is not known. Reorientation or atomic displacement of hydrogen centres has been suggested by Staebler and Wronski.

To check the presence of SWE in ARE intrinsic films deposited under optimised conditions, they were first annealed at 200°C in the usual way in the dark. They were then illuminated with AM1 light at room temperature for 16 hours and the conductivity was remeasured. A typical result is shown in Fig. 5.17, from which it can be seen that there is no Staebler-Wronski effect in these films. This may be

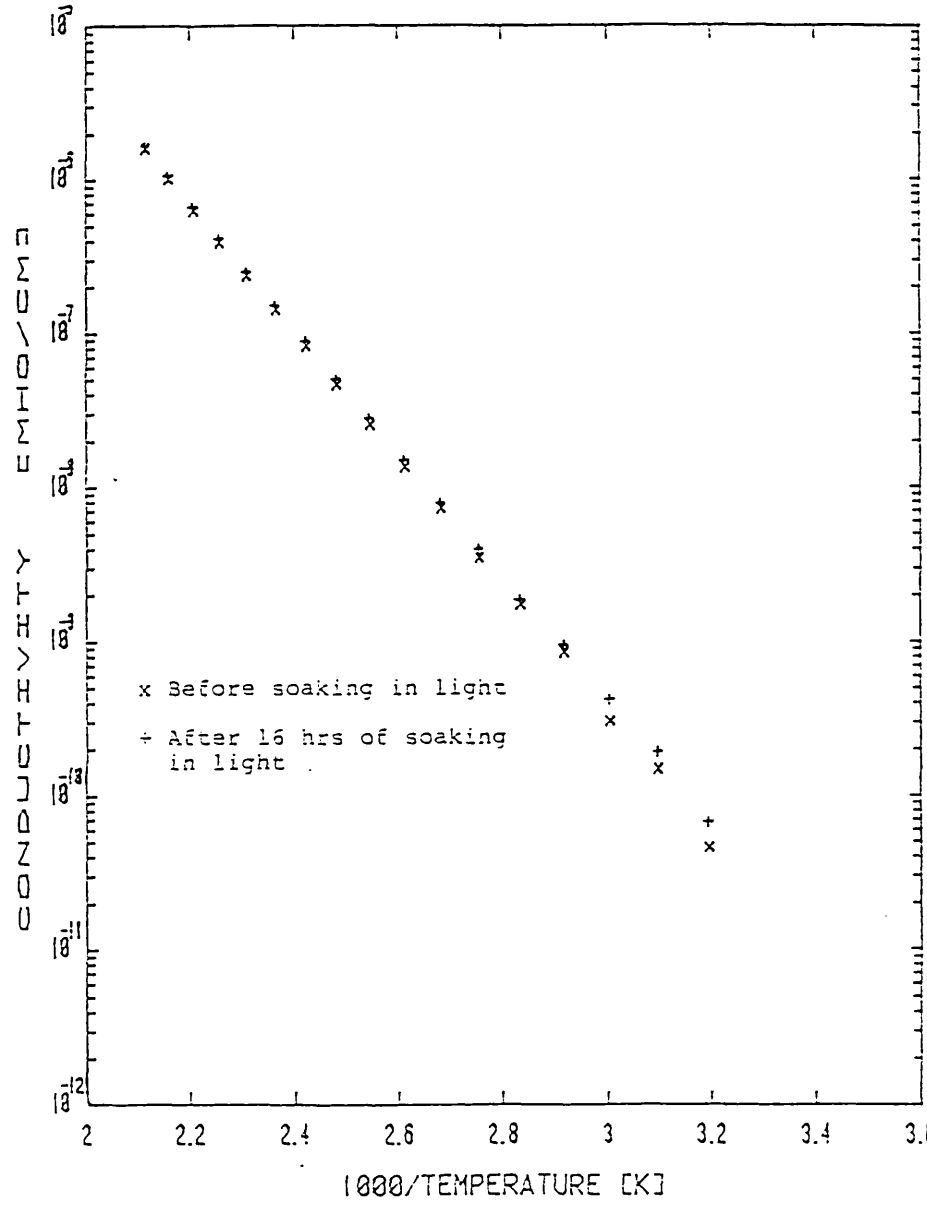

Fig. 5.17 Dark conductivity vs 1000/temperature of an annealed sample before and after soaking in AM1 light.

an inherent property of this particular type of deposition technique.

5.2.4 Discussion on Intrinsic Films

The data presented here on conductivity and photoconductivity of the intrinsic ARE films represents a contribution to the further understanding of the role played by hydrogen in modifying the electronic density of states in amorphous silicon. It is an established fact that hydrogen is effective in reducing the density of states in the mobility gap. The data presented here is consistent with this fact (on the basis of similarities seen between these conductivity and photoconductivity data to those found in the literature on glow discharge and sputtered a-Si:H films). The results have shown that the amount of hydrogen required to neutralise effectively the number of dangling bonds is about 2%, yet most of the materials characterised by other laboratories [18,19, 20] contain at least 10% or more. A detailed study of sputtered a-Si:H by Anderson and Paul [9] containing hydrogen from 0 to >10% has shown that films containing smaller amounts of hydrogen do not show hydrogen associated defects. They suggest that excess hydrogen can create defects in the film in one of two ways:

(1) By occupying a site in the network which would have been a viable site for a silicon atom, therefore terminating the network at that point and forcing it to grow around the hydrogen atom.

(2) By the formation of multiply bonded SiH_x or $(SiH_2)_x$ complexes which can also force the network to depart from a regular, random fully co-ordinated tetrahedral network. When the hydrogen concentration increases, the volume fraction occupied by these defects also increases to a point that the defect regions can be regarded as a completely separate phase. This phase can become dominant in the conduction mechanism only when it becomes so extensive that it surpasses the a-Si:H phase. Therefore, in high hydrogen concentration films a two-phase structure should be considered in the interpretation of conductivity data.

The results shown in Figs. 5.13 and 5.14 (in view of infrared measurements presented in Chapter 4) can be attributed, primarily, to the first reason given above, i.e. termination of the tetrahedral network (relatively small peaks at 500 cm^{-1}), and, secondly, to the larger fraction of SiH_x sites present in the material (there were no $(SiH_2)_x$ sites evident from the infrared measurements).

It is suggested the annealing effects seen in these films are due to the re-organisation of the network.

Due to the lack of Staebler-Wronski effect in the low hydrogen content films, it is tentatively suggested that this effect is found in high hydrogen content films and is

associated with defect structure created by excess hydrogen, as observed in glow discharge films. (It may also be process parameter dependent, as has been claimed by some authors [16], for glow discharge films.) Anderson and Paul [9] observed that films with small (2%) hydrogen content showed very little Staebler-Wronski effect, and this would support the view presented above.

Summarising, it has been shown that ARE films produced with zero or low substrate bias showed relatively poor thermal stability and had, in general, higher hydrogen content than films produced with high negative substrate bias. Furthermore, the high bias produced films with better electrical properties and no Staebler-Wronski effect.

In physical terms the effect of the negative bias is to produce continuous bombardment of the growing film by positive ions, which evidently has the effect of improving short-range order and reducing dangling bond density. The results presented in this section are consistent with such a model and also show that, where the bombardment includes a heavy ion such as argon, new defects are created which worsen the film quality.

Further support for this interpretation is to be found from the infrared absorption spectra (chapter 4) in which it is shown that the 500 cm^{-1} peak, which is associated with short range order, is increased in magnitude and reduced in relative width by the introduction of negative bias, where the hydrogen content is relatively low.

5.3 DOPED a-Si:H FILMS

Doping can be achieved by mixing diborane (B_2H_6) or phosphine (PH_3) with silane (SiH_4) in a glow discharge system, or with hydrogen and argon in a sputtering system, to produce p-type or n-type a-Si:H respectively. The room temperature conductivity can thus be changed by several orders of magnitude. This approach was used with the ARE process to produce both p-type and n-type a-Si:H films.

15% phosphine in hydrogen and 5% diborane in hydrogen gas mixtures were available. A chosen fraction of dopant gas was obtained by controlling the rates of flow of the dopant/hydrogen mixture and the hydrogen gas to give an appropriate ratio of dilution in the chamber. The films were deposited under optimum conditions, which produced the best quality intrinsic films. The conductivity results of these films are presented in the next section.

Phosphine and diborane are very toxic gases and the preparation of doped films without their use would be very attractive. As mentioned earlier, a set of experiments was carried out in order to investigate whether doped samples could be obtained using a doped ingot of silicon. This proved unsuccessful, as doped ingots available from industry contain only a few parts per million of the dopant atoms and the doping efficiency was low. A silicon ingot containing a few percent of antimony was finally used (see Chapter 3) to obtain n-doped a-Si:H. These results are presetned in section 5.3.2.

5.3.1 Gaseous Doping

Various levels of doping were achieved by introducing controlled amounts of phosphine or diborane into the deposition chamber. In Figs. 5.18 and 5.19 are shown the variation of dark conductivity as a function of 1/temperature for eight different levels of phosphorous doping. In Figs. 5.20 and 5.21 are shown the same for boron doping.

It is conventional to present the doping in terms of plots of dark conductivity and activation energy against the ratio of dopant gas partial pressure/SiH_4 partial pressure for glow discharge depositions. In the ARE process the silicon is provided by evaporation from the ingot and it is necessary to determine the equivalent partial pressure of silicon vapour in order to compare the results with those in the glow-discharge system. Whilst the vapour pressure of silicon above molten silicon is known as a function of temperature, the precise temperature of the electron-beam heated pool is not known. Furthermore, the hydrogen pressure in the chamber is such that diffusive transport of the silicon to the substrate will occur and the effective temperature of the plasma is not known. It is, therefore, not possible to make an absolute calculation of the effective partial pressure of silicon in the chamber.

In Figs. 5.22 and 5.23 are shown the room temperature dark conductivity versus percentage dopant gas in hydrogen/ silicon evaporation rate for n-type and p-type films respectively. The corresponding activation energies for the

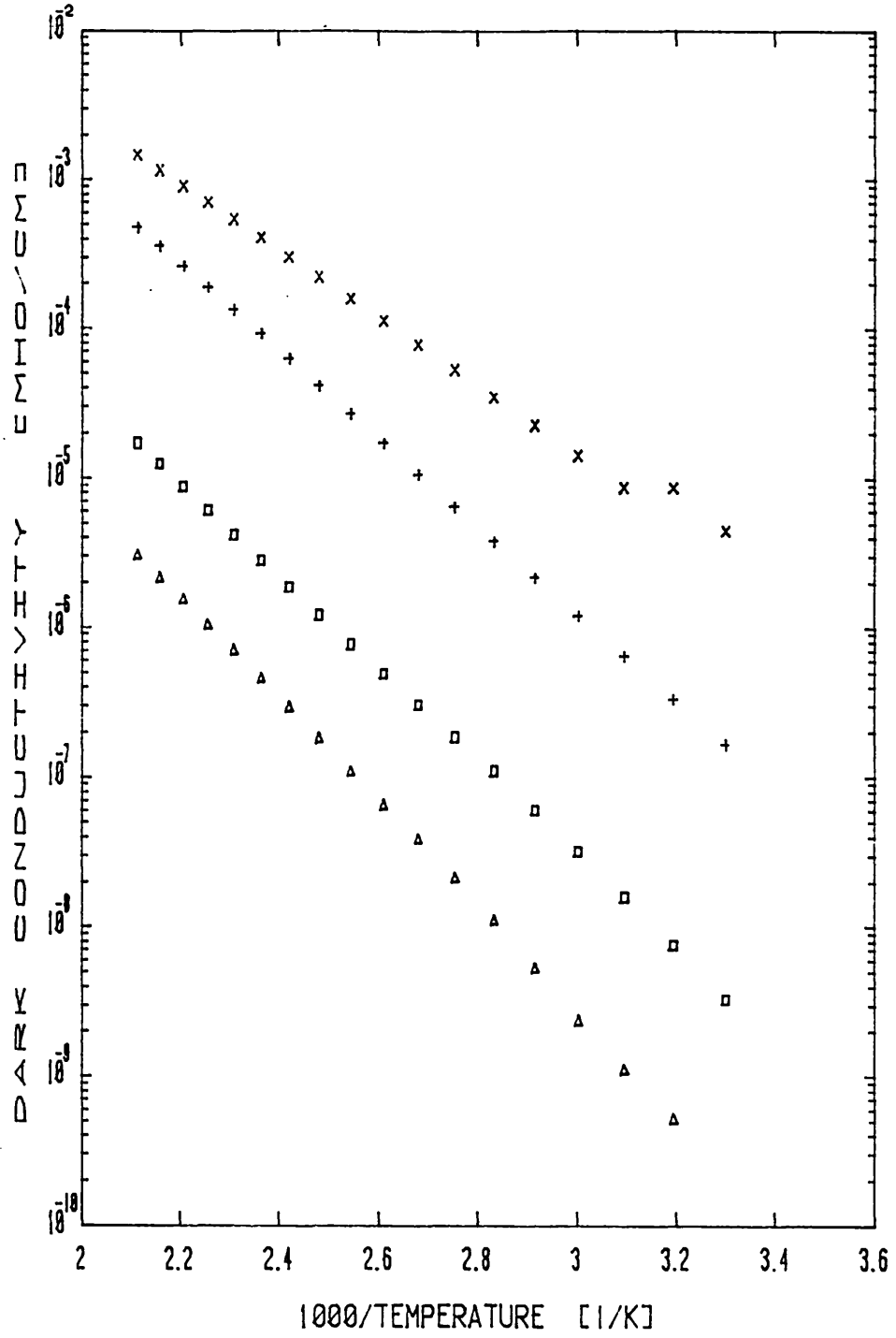

Fig. 5.18 Figures 5.18 and 5.19 show dark conductivity vs.1000/temp. for n-type samples.

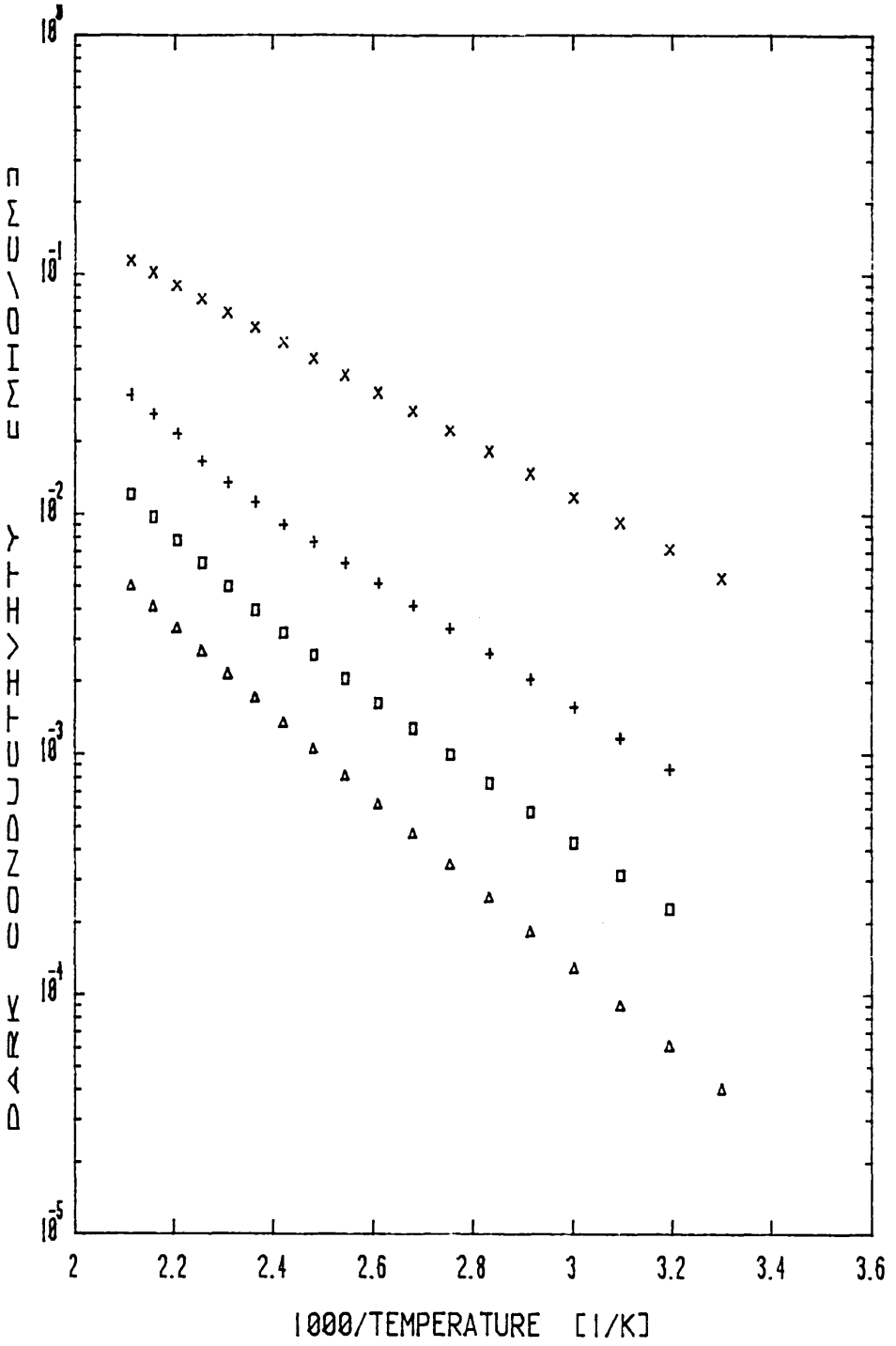
DARK CONDUCTIVITY [1/OHM CM]
1000/TEMPERATURE [1/K]
2
2.2
2.4
2.6
2.8
3
3.2
3.4
3.6

Fig. 5.19

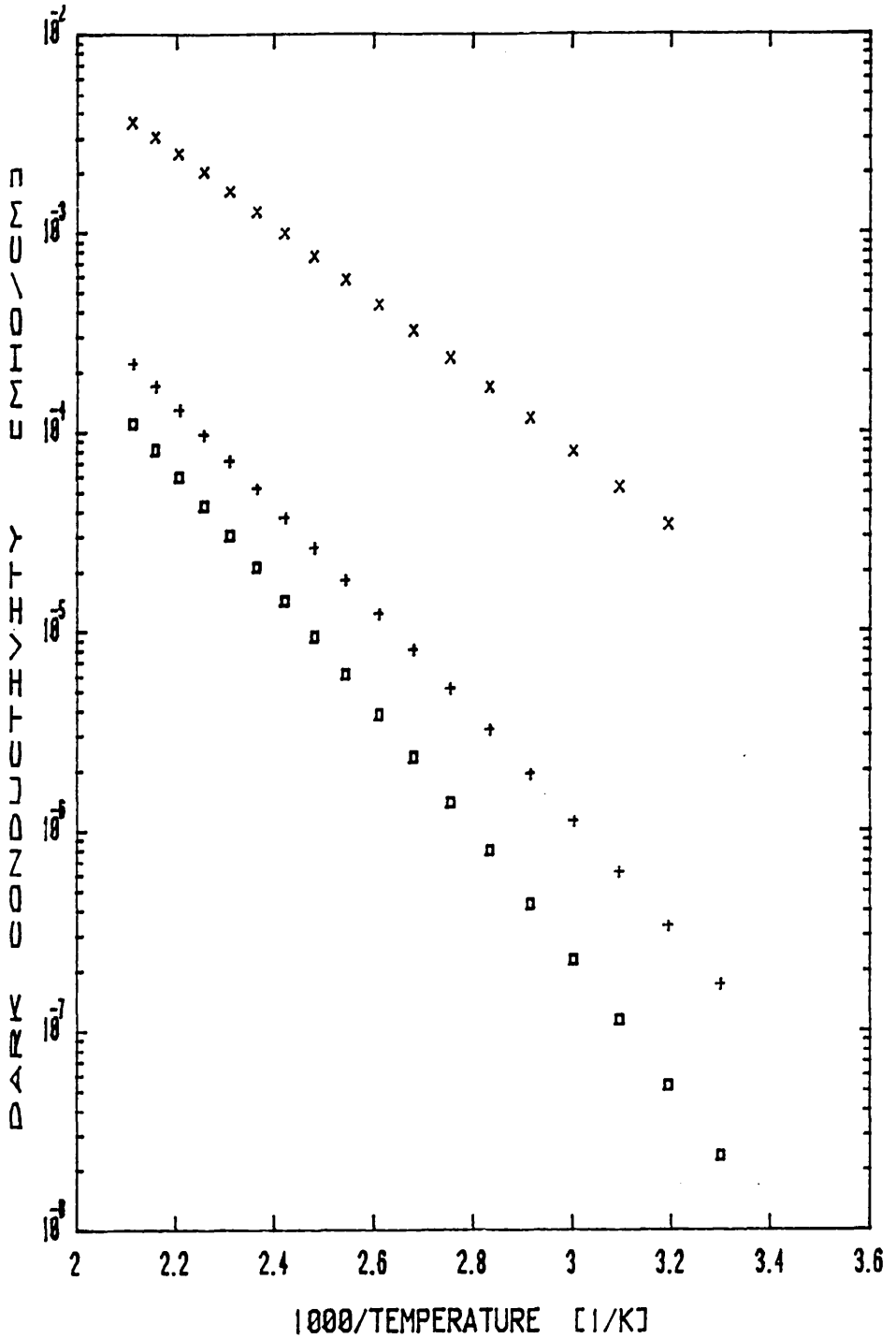

Fig. 5.20 Figures 5.20 and 5.21 show dark conductivity vs.1000/temp. for p-type samples.

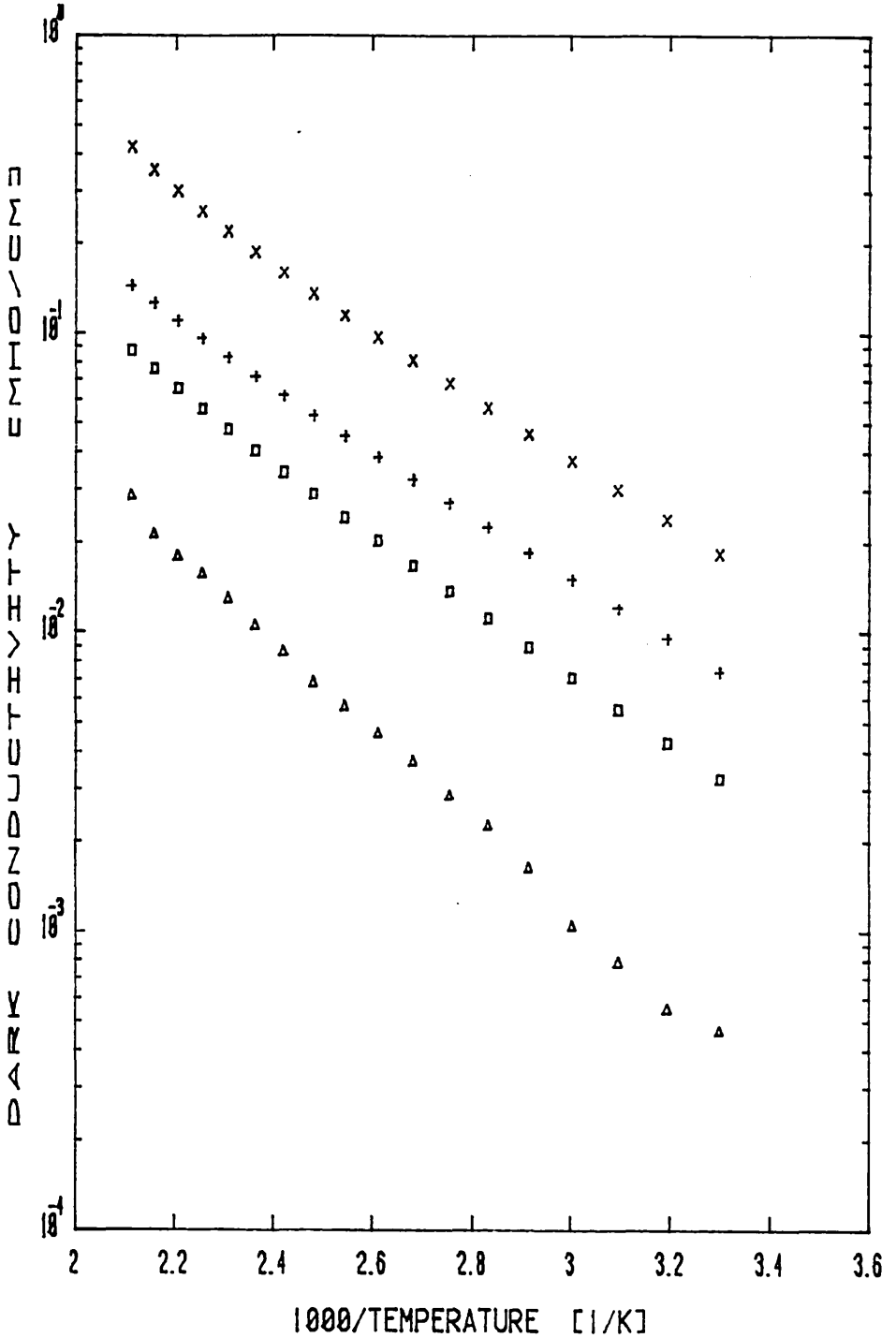
DARK CONDUCTIVITY [Ω⁻¹cm⁻¹]
10⁰
10⁻¹
10⁻²
10⁻³
10⁻⁴
2
2.2
2.4
2.6
2.8
3
3.2
3.4
3.6
1000/TEMPERATURE [1/K]

Fig. 5.21

two groups are shown in Figs. 5.24 and 5.25 respectively as a function of the percentage dopant gas in hydrogen/ silicon evaporation rate.

If, however, one uses the following to represent the doping results, i.e.

$$R = \frac{\text{fraction of dopant gas in hydrogen}}{\text{deposition rate of silicon in } \mu m/min}$$

fortuitously, the values of this ratio are similar to the partial pressure ratio used for the glow-discharge method. The results of p and n doping, with diborane and phosphine respectively are shown in Fig. 5.26, which gives the room temperature conductivity as a function of the above ratio, R and, in Fig. 5.27, which gives the activation energy against R. The dotted lines in these graphs show Spear's and LeComber's results [21], where the horizontal axis represents the pressure ratio in their case and R for the ARE films. It is seen that the shapes of the curves are similar, but that, for the ARE films there is a wide range of R over which there is little doping effect, approximately up to $R = 10^{-4}$. It would appear that there is a threshold value for dopant gas partial pressure above which electrically active doping is achieved. This has the considerable advantage that traces of dopant gas in the chamber do not affect subsequent deposition of intrinsic material, and so the system does not suffer from cross-contamination problems when depositing p-i-n structures.

With traces of diborane, i.e. for $R = 10^{-3}$, a room temperature conductivity in the dark of value 10^{-12} $(\Omega\ cm)^{-1}$

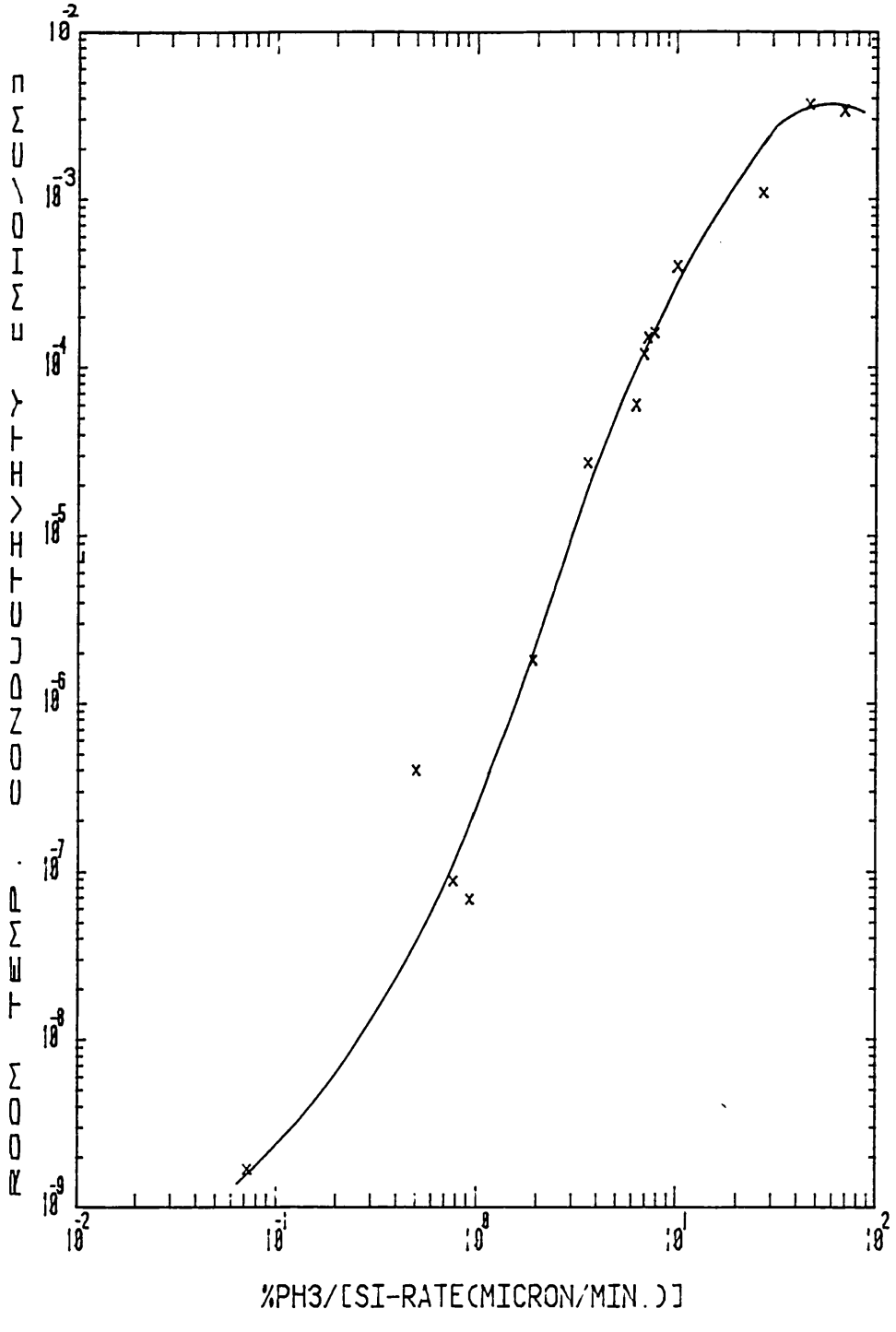

Fig. 5.22 Room temp. dark conductivity vs. percentage PH_3 in hydrogen/silicon evaporation rate.

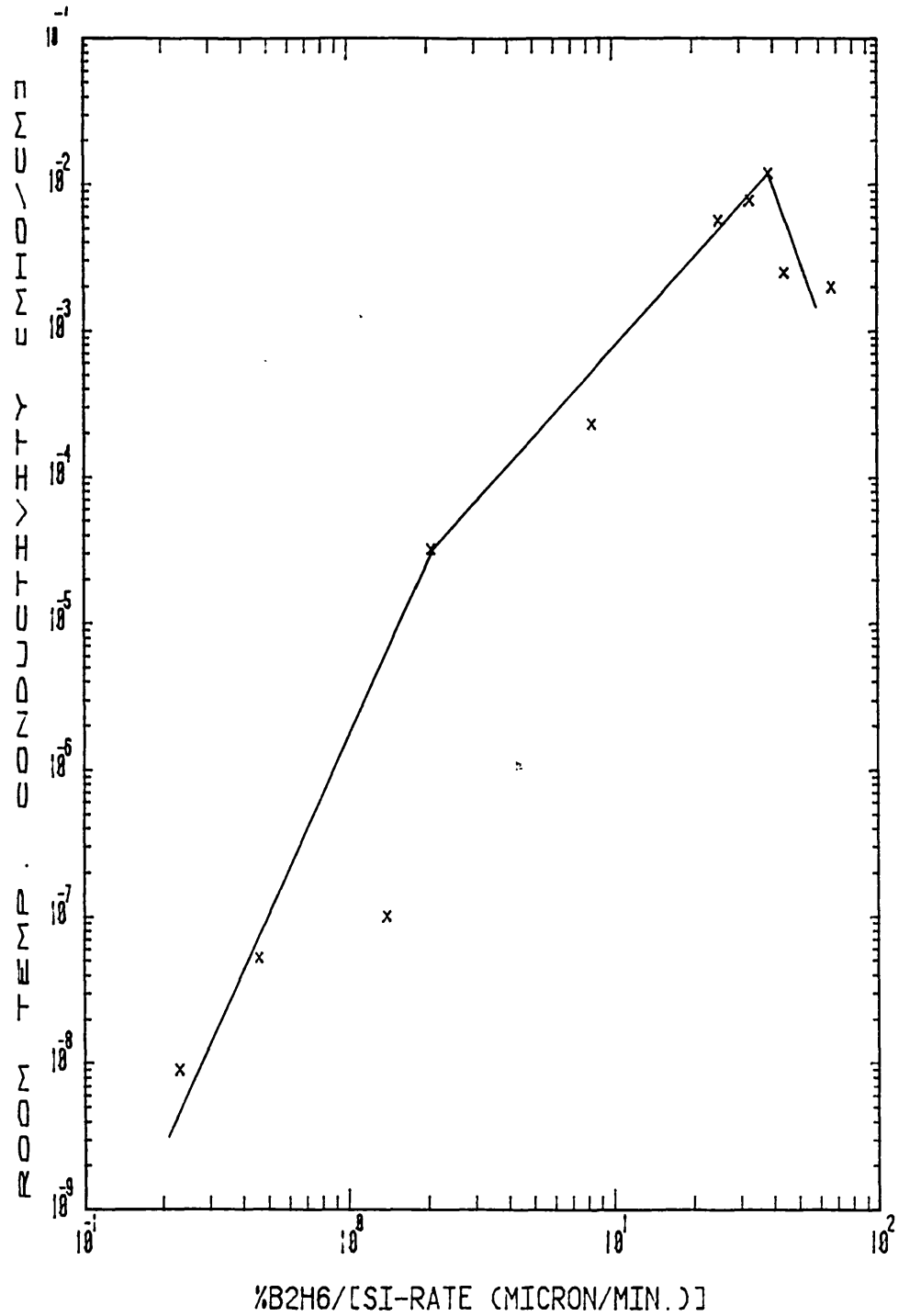

Fig. 5.23 Room temp. dark conductivity vs. percentage B_2H_6 in hydrogen/silicon evaporation rate.

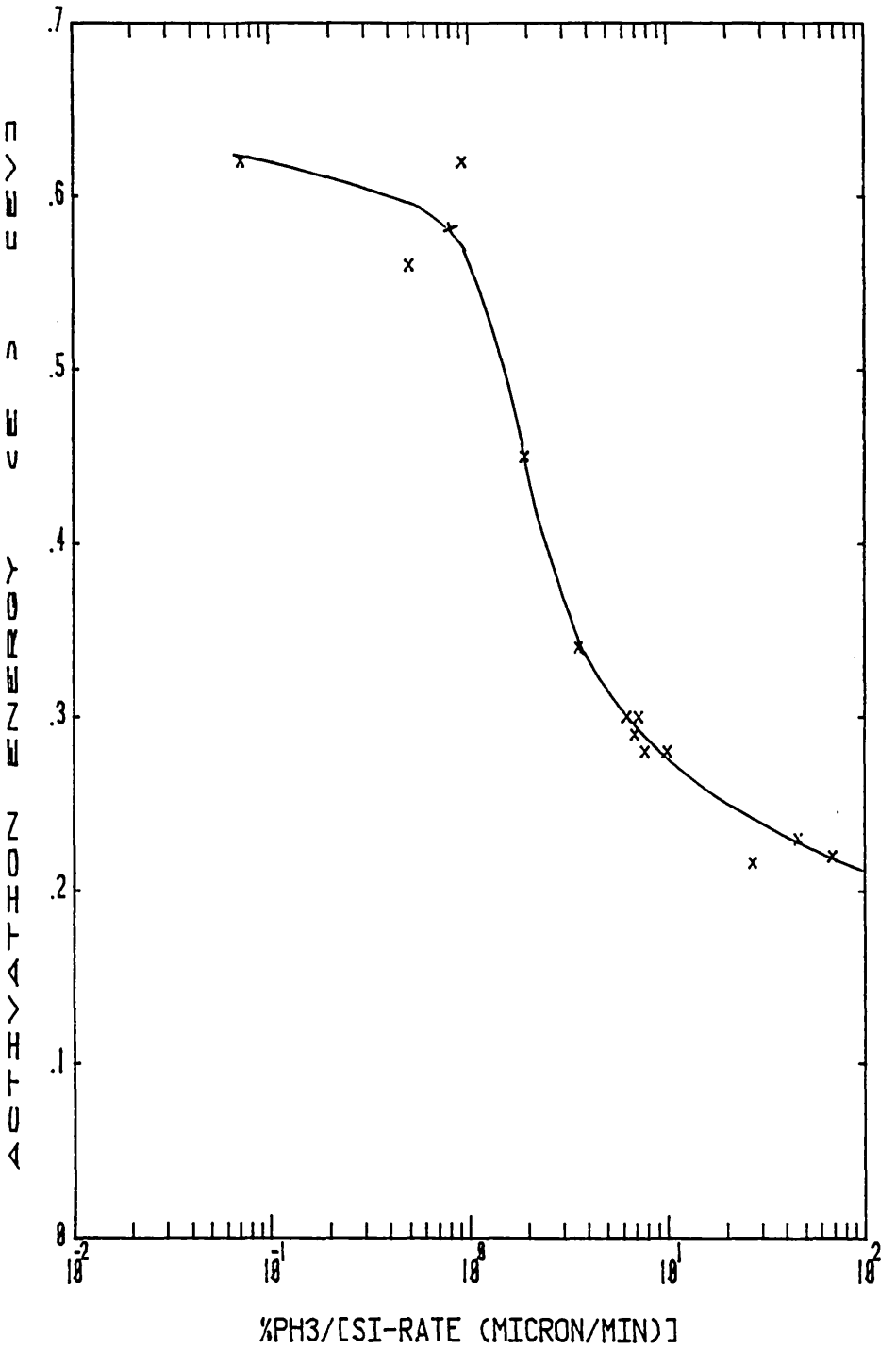

Fig. 5.24 Activation energy vs. $\%PH_3$ in hydrogen/silicon evaporation rate.

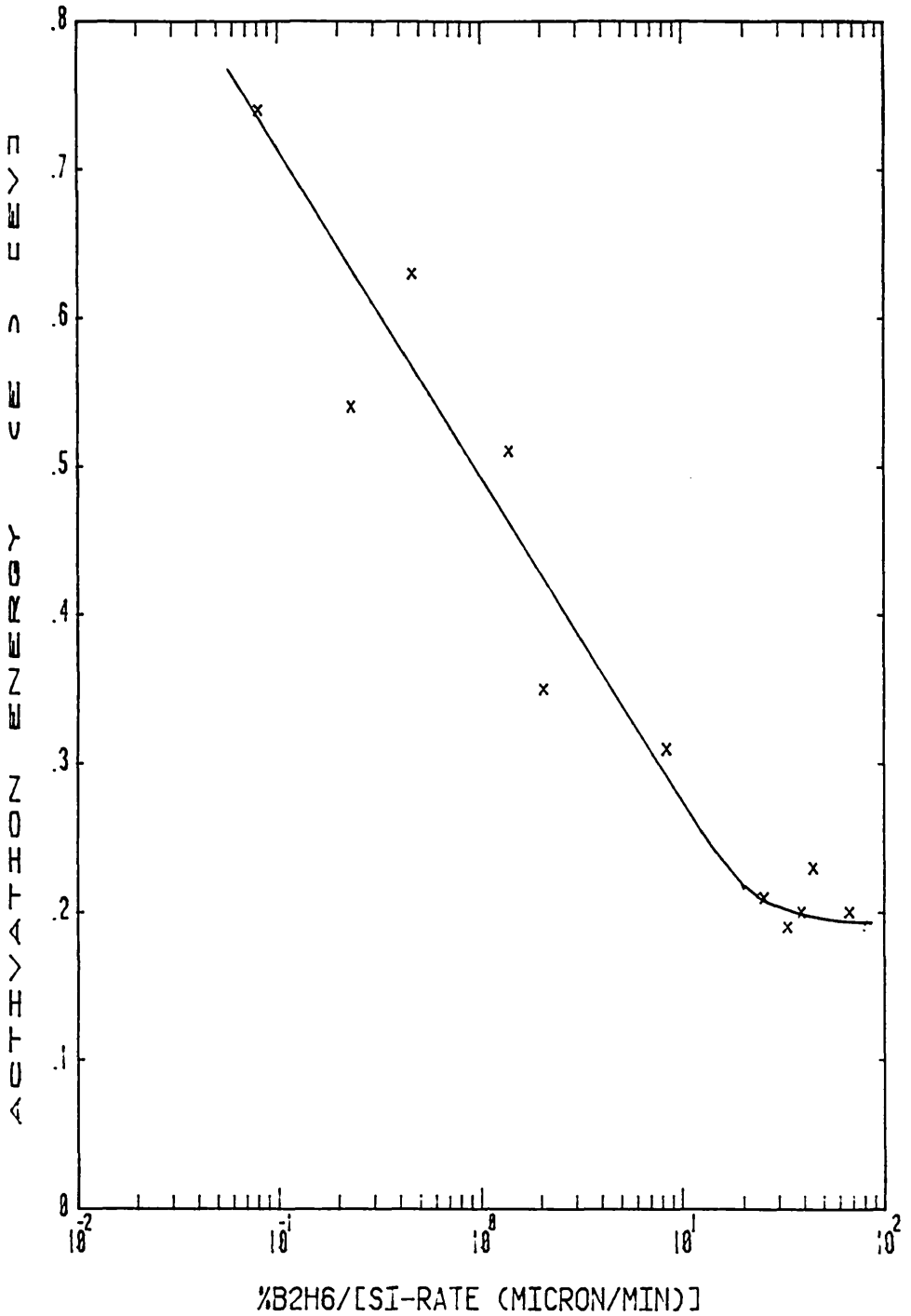

Fig. 5.25 Activation energy vs. $\%B_2H_6$ in hydrogen/silicon evaporation rate.

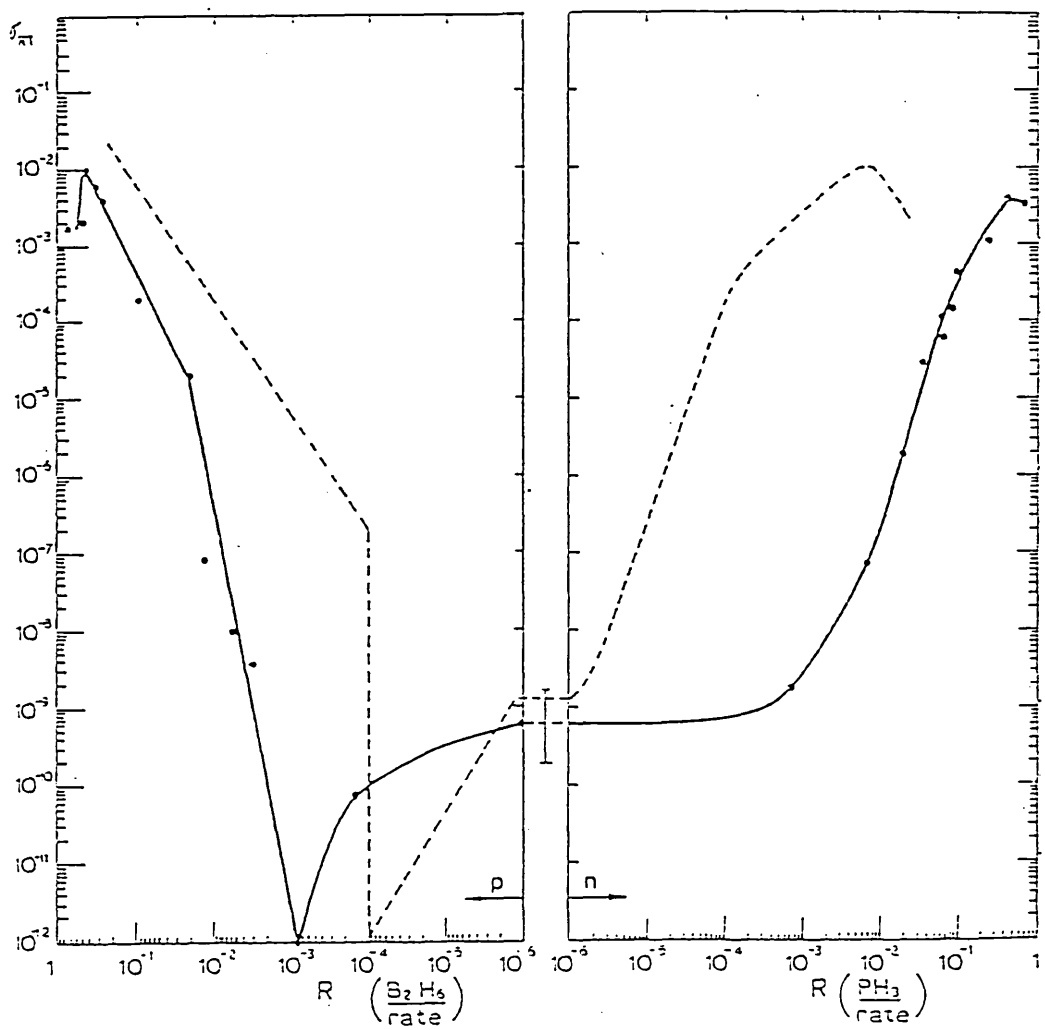

Fig. 5.26 Plot of room temperature conductivity against the ratio

$$R = \frac{\text{fraction of dopant gas in hydrogen}}{\text{deposition rate in um/min}}$$

Dotted line gives results for glow discharge method where

$$R = \frac{\text{partial pressure of dopant gas}}{\text{partial pressure of silane}}$$

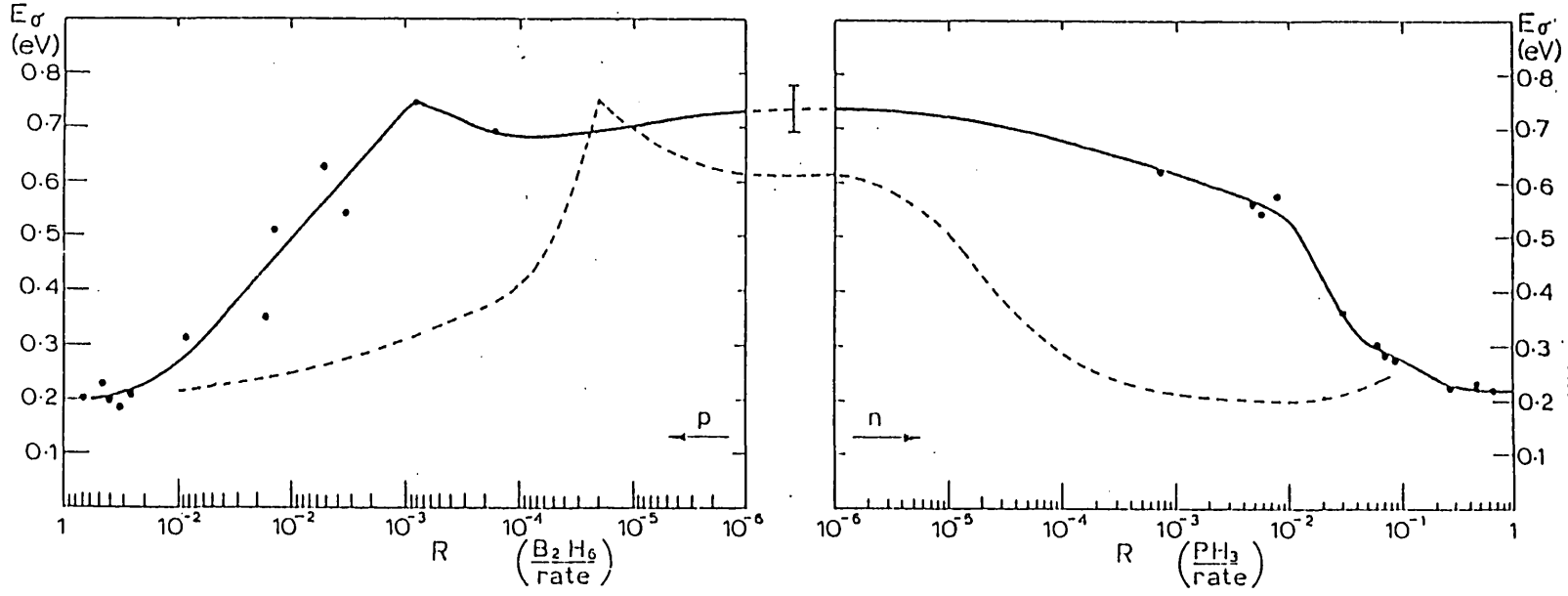

Fig. 5.27 Activation energy against

$$R = \frac{\text{fraction of dopant gas in hydrogen}}{\text{deposition rate in } \mu m/min}$$

Dotted line gives results for glow discharge method where

$$R = \frac{\text{partial pressure of dopant gas}}{\text{partial pressure of silane}}$$

has been obtained. The corresponding p.c.r. for this film was 10^5 and equals the best reported results for glow discharge films.

Secondary Ion Mass Spectrometry (SIMS) analysis of a p-type and an n-type film was carried out. For a film prepared in a gas mixture of 1% phosphine in hydrogen under standard conditions, the phosphorous concentration in the film was found to be 1×10^{19} cm^{-3}. Using an electron mobility of 0.2 cm^2 V/s this gives a value for the carrier density of 1.26×10^{16} cm^{-3}. This implies a doping efficiency of 1.26×10^{-3}, i.e. 0.13%. For a film doped with 5% diborane in hydrogen the SIMS analysis gave the boron concentration as 2×10^{21} cm^{-3} for $R = 2.5 \times 10^{-1}$. Using drift mobility for holes of 5×10^{-4} cm^2 V/s quoted by Streemers et al [22], the value for the carrier concentration is 7×10^{19}, and implies a doping efficiency of 3.5×10^{-2}. (For GD and r.f. sputtered films doping efficiencies of 30% [23] and approx. 1% [24] are quoted respectively.) The relatively low doping efficiencies support the view that cross-contamination in the preparation of p-i-n structures should not be a problem. SIMS analysis also revealed in both cases that the distribution of the dopant atoms was uniform throughout the film and were not incorporated in the film in clusters.

5.3.2 Solid State Doping

It is believed that for a dopant atom to achieve tetrahedral co-ordination [25] and hence electrical activity in the film, it is necessary for it to enter the film with

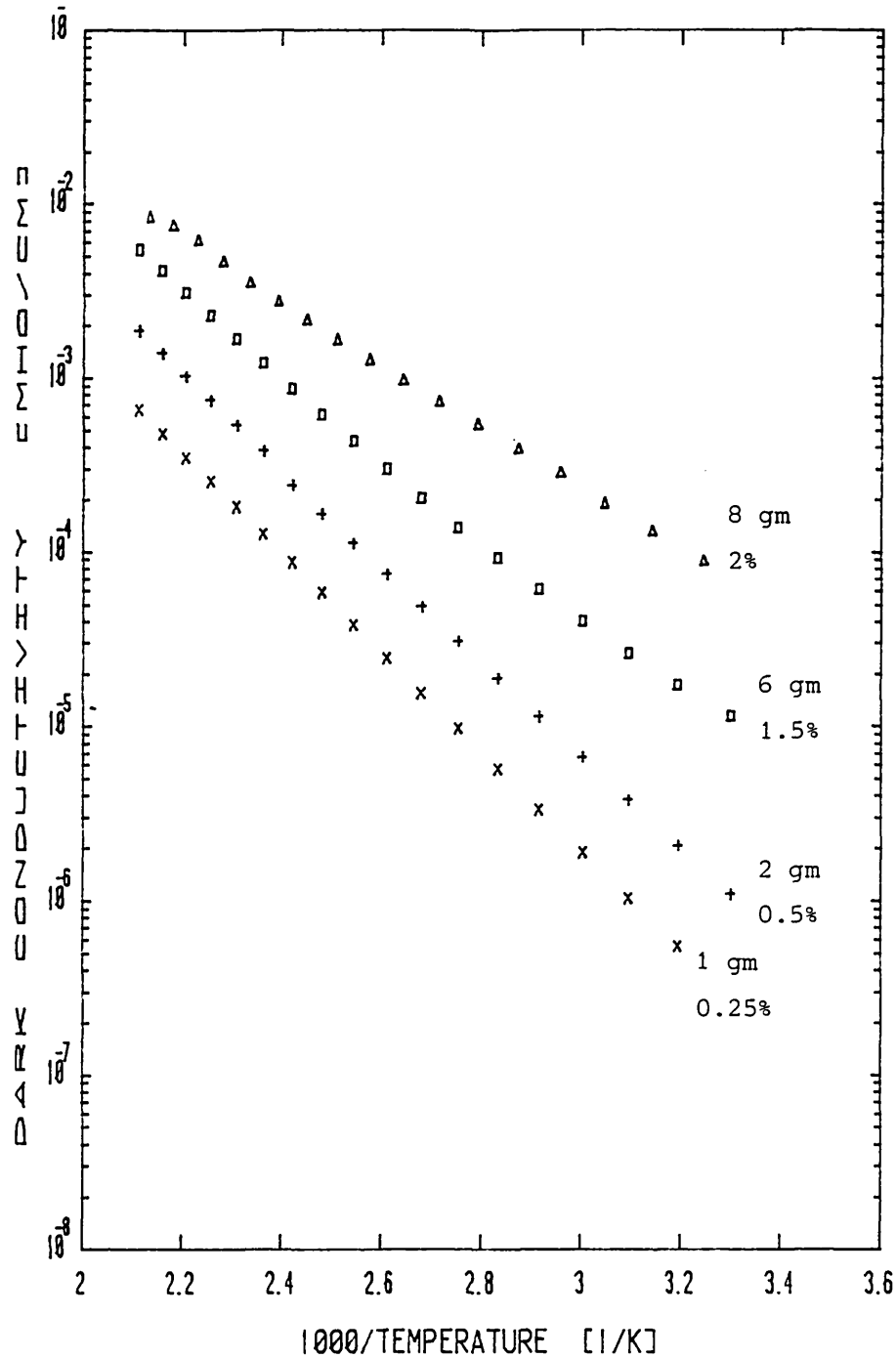

Fig. 5.28 Dark conductivity vs.1000/temp for various levels of Sb doping.

a hydrogen atom attached. It was argued that, if an ingot was pre-doped, the evaporated dopant atoms would pick up a hydrogen atom in the plasma and hence provide electrically active doping of the film. However, in view of the low doping efficiency achieved in the gaseous doping system it is clear that the initial concentration of dopant atoms in the ingot must be at percentage levels rather than the normal parts per million. To date it has been found impossible to persuade a silicon manufacturer to provide the necessary ingot material.

Some crude experiments were carried out in which a few grams of antimony were placed around the edge of the cold ingot and this was melted into the silicon on heating up with the electron beam. Unfortunately, since antimony melts at ~600°C and silicon at 1420°C, much of the antimony is evaporated before it dissolves into the silicon. It was, therefore, impossible to make an accurate assessment of the amount of antimony actually entering the silicon. On completion of the experiments the silicon ingot was analysed in a scanning electron microscope energy analyser and ~2% antimony was detected in the silicon. This was the result of the addition of 8 gms of Sb; the other results were proportioned to 2% according to the amounts of Sb added and the family of conductivity curves of Fig.5.28 was produced, in which each curve is labelled with the percentage of Sb assumed present in the ingot. Conductivity at room temperature is plotted against percent antimony content in Fig. 5.29 from which it is seen that doping does take place. The rates used were ~0.25 μm/min. Furthermore,

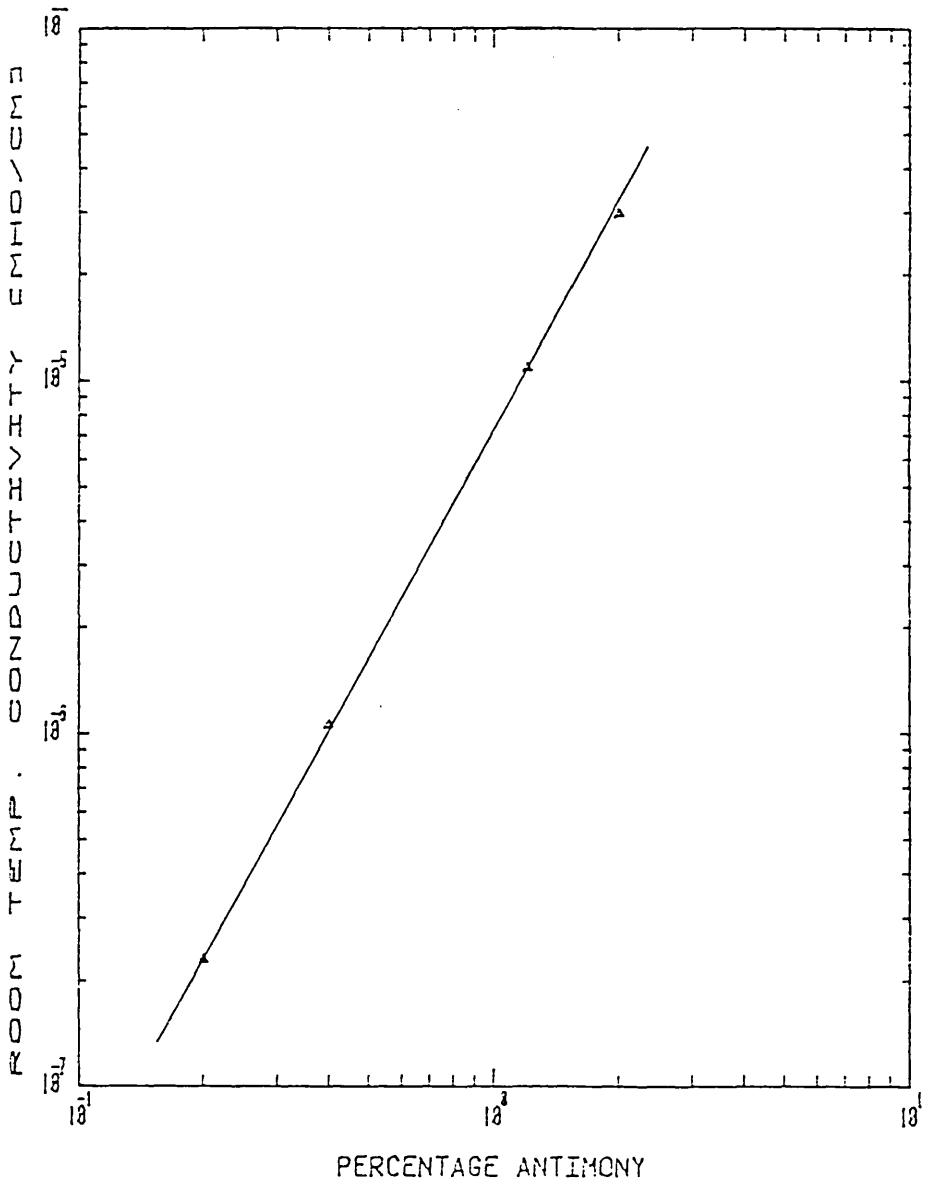

Fig. 5.29 The variation of room temp. dark conductivity with percentage antimony.

the conductivity for a given percent over the range used, is comparable with the conductivity obtained with gaseous phosphorous doping.

These results indicate that gaseous doping is not necessary if ingots containing the required concentrations of dopant can be obtained. However, the doping efficiency in this case is estimated to be ~3 x 10^{-5} for Sb.

5.3.3 The Pre-Exponential Factor (σ_o)

The pre-exponential factor (σ_o) was discussed in Chapter 2, (section 2.3.2) and it was pointed out that the values of σ_o varied from ~10 to ~10^4. The value of σ_o has been found to follow a systematic relation

$$\sigma_o = \text{const} \quad e^{E_\sigma/kT}$$

which is referred to as the Meyer-Neldel rule [26]. E_σ is the activation energy for conduction which is varied by doping [26, 24]. Fig. 5.30 shows a variation of σ_o with E_σ obtained by Anderson and Paul [24]. In this plot they have included some samples from their own work and from the Marburg and the Dundee groups. Those broadly conform to the Meyer-Neldel rule.

In Fig. 5.31 is shown a plot of σ_o versus E_σ (the activation energy) of all the samples referred to in this thesis, which include the intrinsic samples (x), the phosphorous doped samples (□), the boron doped samples (Δ) and the antimony doped samples (+). With the exception of the three arrowed points (←), all points seem to lie in a line with a certain amount of scatter. It is considered

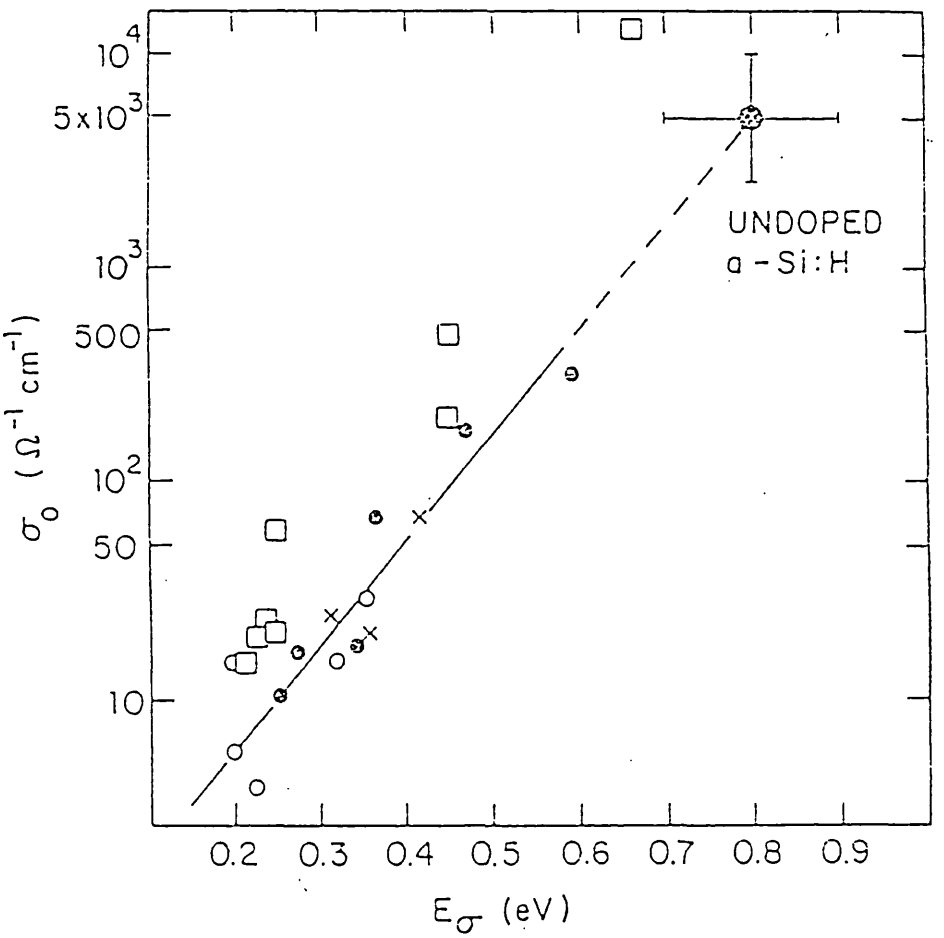

Fig. 5.30 Plot of σ_0 versus activation energy for a-Si:H from various groups

x, ● Harvard group

o Marburg group

□ Dundee group

(After D.A. Anderson and W. Paul, ref. 24).

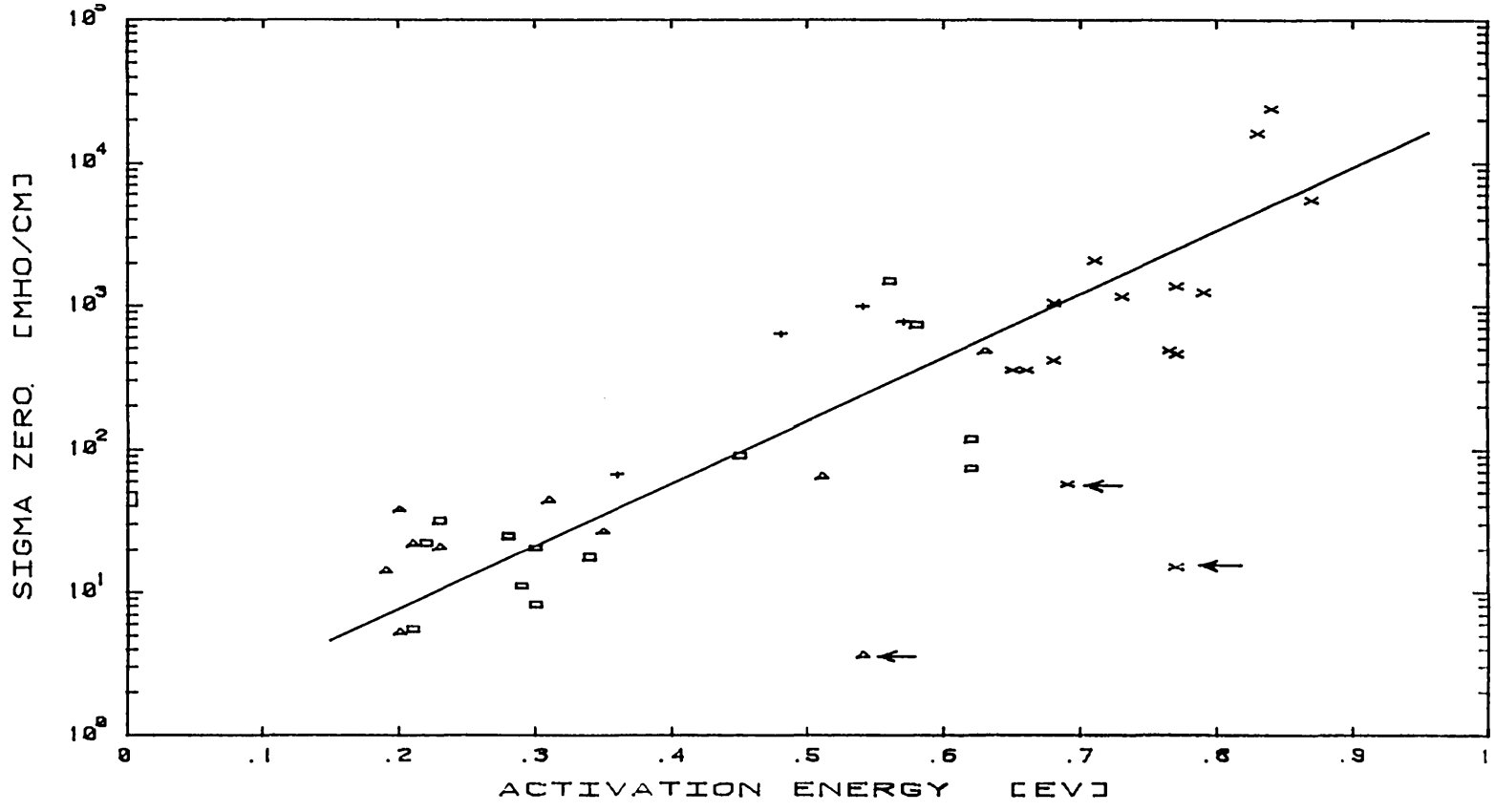

Fig. 5.31 Plot of σ_0 versus activation energy for ARE films.

that the σ_o versus E_σ plot follows the Meyer-Neldel rule for the ARE samples. It is believed by Mott [26] that σ_o is very sensitive to homogeneity and if this is the case the scatter in σ_o values is to be expected due to the lack of absolute control of the deposition parameters.

CHAPTER 6

CONCLUSIONS AND FUTURE WORK

6.1 CONCLUSIONS

It has been shown that it is possible to produce good quality (comparable to glow discharge and sputtered) hydrogenated amorphous silicon using the ARE process developed in this laboratory. The process was developed on the proposition that, in activated reactive evaporation, the conditions pertaining in the normal glow discharge silane plasma, would be synthesised. The best deposition conditions were found to be: probe voltage ~300 volts positive, pressure ~2 x 10^{-2} mB (pure hydrogen) and a substrate bias of >2000 volts negative (r.f.).

The introduction of r.f. negative bias on the substrate during deposition improves the electrical, optical and mechanical properties of the film. This is due to the fact that continuous bombardment of the growing film by positive ions, consisting of H^+ and species of the SiH^+ type, appears to be "hammering" the structure together. The additional energy input to the growing film, due to ion bombardment, increases the mobility of the deposited atoms, so that they are able to find lower energy, fully bonded sites. The overall effect of the bias is to reduce the number of micro-voids and dangling bonds in the amorphous film, with consequent improvement of its thermal stability resistance to internal oxidation and stability of electrical properties under irradiation with light.

It is further shown that for all optimised intrinsic films, there is a substantial and relatively sharp Si-Si peak at 500 cm^{-1} indicating that most of the silicon atoms are in tetrahedral co-ordination and that there are relatively few dangling bonds to be taken up by hydrogen, hence a relatively low hydrogen concentration (~1 atomic percentage) is observed in the infra-red absorption spectra. In the intrinsic films prepared under optimum conditions, the hydrogen bonding is predominantly in the Si:H configuration although $Si:H_2$ bonds are also observed. All films contained traces of oxygen and it has been explained, in chapter 4, that these may be working as a network softener, as in the case of sputtered a-Si:H films [1].

For the optimised intrinsic films a dark room temperature conductivity in the range 10^{-10} to 10^{-11} $(\Omega\ cm)^{-1}$ was obtained with a photoconductivity rate in the range 10^4 to 10^5 under AM1 illumination. These films showed singly activated conduction above room temperature in the dark with activation energies between 0.7 and 0.9 eV.

No Staebler-Wronski effect could be observed in these films; this is a desirable feature for solar cell fabrication. It has been suggested that this may be an inherent property of this particular type of deposition technique.

Electron diffraction patterns have shown the films to have an amorphous structure. A non-normalised radial distribution function obtained from the electron-diffraction pattern confirmed this, showing only first and second nearest neighbour order.

The optical band gap, E_o, was measured. For intrinsic films, a range of values of E_o between 1.55 and 1.67 eV were obtained, which is similar to results for glow discharge films. Empirically a relationship between E_o and the hydrogen concentration for intrinsic and phosphine doped films is derived and is given by $E_o = 1.5 + 0.064$ (%H). For intrinsic films the optical absorption coefficient was found to be in the range 3.5×10^4 cm^{-1} to 10^5 cm^{-1}.

Only a low density of gap states enables the films to be doped from gaseous hydrides, in the same manner as other techniques (i.e. G.D., sputtering, CVD, etc.). However, the doping efficiencies were found to be lower than that for the glow discharge technique. This is not, in practice, an important limitation since full doping over 11 orders of magnitude on the p-side and 8 orders of magnitude on the n-side has been achieved. SIMS analysis showed that the distribution of dopant atoms was uniform throughout the film and were not incorporated in the film in clusters. It was argued that the low doping efficiencies would enable the preparation of p-i-n structures without cross-contamination.

For the gaseous doped films, the hydrogen content decreased with increased dopant concentration, particularly for B_2H_6. This has been explained in terms of formation of B-H bonds at the expense of Si:H bonds in the case for boron doping.

For boron-doped films it is well known that the optical gap, E_o, decreases with increased boron content [2] and, for G.D. films, the minimum value is usually 1.2 to 1.3 eV. For the ARE films a value of 1.1 eV was obtained.

For the phosphorous doped films E_o varied between 1.45 to 1.6 eV with the lower value corresponding to the higher doping level.

"Solid state doping" with antimony mixed with the silicon ingot produced doped films, with room temperature conductivity which could be varied over several orders of magnitude. This proved the point of earlier work of Anderson et al. [3] that a doped a-S:H film could be obtained starting with a doped source. The fact that the optical absorption of antimony doped material is an order of magnitude lower than that of phosphorous doped material, and decreases with increasing antimony content, suggests that antimony could be used in the fabrication of a n-i-p solar cell, as it is important to minimise the absorption of light in the n-layer. Antimony doped n^+ layers are, therefore, extremely suitable for application in solar cells.

Finally, the pre-exponential factor (σ_o) was found to follow the Meyer-Neldel rule for the ARE deposited films, in which σ_o values varied from ~10 to ~10^4 in close comparison to those obtained by various groups working with G.D. and sputtered a-Si:H films [4].

Finally, the advantages of the new method can be summarised as:

(1) High-rate deposition - up to 20 μm per hour has been achieved in the present plant.

(2) Film quality comparable to glow discharge and sputtered a-S:H.

(3) No silane required.

(4) Insensitivity to contamination.

(5) Capable of full range of doping from p^+ to n^+ from gaseous hydrides.

(6) Potential for solid-state doping, eliminating the use of gases.

(7) The absence of Staebler-Wronski effect.

6.2 FUTURE WORK

The density of states of the ARE films was not measured directly for all the different deposition conditions due to lack of time. However, during the course of finishing this thesis, two field effect transistors (n^+ and p^+) were fabricated by the author and Mr. H. Guo (Academic Visitor, Hua Chiao University, China) and measurements were carried out by Mr. Guo, following the work of Z.S. Jan et al. [5] and values of drift mobility (μ) for electrons in n^+ material were found to be 0.6 cm^2/vs with an activation energy of 0.275 eV at room temperature and a corresponding $N(E_f)$ (density of states) of 4.14×10^{18} cm^{-3}. For holes in p^+ material, $\mu = 8.04 \times 10^{-3}$ cm^2/vs with an activation energy of 0.195 eV and a corresponding $N(E_f) = 7 \times 10^{18}$ cm^{-3}. The above experiments have to be repeated for various ranges of doping levels.

Further work on the fabrication of various working devices, such as a p^+-i-n^+ solar cell and xerographic devices, etc. should be carried out.

Flexibility of the system would enable the fabrication of nitrides, oxides or carbides by changing the gaseous ambient. This opens up a whole new area of study for the continuation of the present work.

APPENDIX 1

PHILOSOPHICAL MAGAZINE B, 1980, VOL. 43, No. 1, 51–60

Preparation of amorphous silicon by sputtering in silane

By J. C. ANDERSON, KI-WAN KIM† and E. SEFERIADES
Department of Electrical Engineering, Imperial College of Science and Technology, London SW7, England

[Received 17 October 1979 and accepted 10 April 1980]

ABSTRACT

In the work reported here we have r.f. sputtered silicon in argon–silane mixtures using undoped, n-type and p-type targets. Doped films have been produced, but the doping efficiency is extremely low. It appears that the dopant atoms are able to satisfy their natural valencies and are therefore not electrically active. Infrared absorption spectroscopy has been used to establish the hydrogen bonding in the films and values for oscillator strengths of the various modes have been derived. No correlation has been found between the nature of the hydrogen bonding in the film and the electrical properties.

§ 1. INTRODUCTION

Amorphous silicon films prepared by deposition from a glow discharge have been extensively studied (see, for instance, Spear 1977). These have been successfully doped by the addition of borane or phosphine to the silane gas. The present work was undertaken to explore the possibility of preparing doped films by sputtering from a doped silicon target in a mixture of argon and silane gases. Infrared absorption spectra were used to determine the amount and nature of the bonded hydrogen in the films in order to compare them with glow-discharge films reported on in the literature (Brodsky, Cardona and Cuomo 1977, Knights 1976, Tsai and Fritzsche 1979) and with films prepared by silicon sputtering in argon–hydrogen mixtures (Freeman and Paul 1978). This led to a determination of the oscillator strengths of the various infrared vibration modes associated with silicon–hydrogen bonds.

The electrical conductivities of the films down to liquid nitrogen temperatures were measured and the activation energies were compared with those reported for glow-discharge films by Spear and Le Comber (1976) in order to estimate the degree of doping attained.

§ 2. EXPERIMENTAL

An r.f. sputtering system was built, incorporating two target electrodes and a counter-electrode. A power-splitter enabled r.f. power to be supplied either to the two targets simultaneously with the counter-electrode earthed, or to one target and the counter electrode. The latter was provided with an electrical

† Now at Kyungpook National University, Department of Electronics, Daegu, Republic of Korea.

0141–8637/81/4301 0051 $02·00

heater which could be used to heat the substrates up to 400°C when the counter-electrode was earthed, but it was not possible to heat the substrate when r.f. power was supplied to the counter-electrode. A gas-flow control system enabled the argon flow rate to be set, usually at 40 cm^3 min^{-1}. The percentage of silane was set by adjusting to the appropriate flow rate of SiH_4 and the control system ensured that the argon/SiH_4 ratio was kept constant. The vacuum system had a background pressure of 10^{-3} μm and sputtering was carried out at pressures in the range 3–20 μm by adjustment of flow rate and pumping speed. The substrates used were 7059 glass, ultrasonically cleaned and subsequently vapour cleaned in isopropyl alcohol, for electrical measurements, and single-crystal KBr slices for infra-red measurements. Thicknesses were measured by a 'Talysurf' and by multiple-beam interferometry.

A magnetron target was also available. This contains the lower energy electrons near the target, reducing the electron bombardment of the substrate, and also gives higher rates of sputtering compared with the conventional system.

The silicon targets used were 3 in. diameter, single-crystal (111) slices doped both n- and p-type to various concentrations, supplied by Wacker Chemitronics A.G. The deposition rate from each target was determined by sputtering in pure argon. When silane is admitted, silicon is deposited from the gas at a rate determined by gas pressure and flow rate but this rate is relatively independent of sputtering power. At a pressure of 3 μm, silicon is deposited from the gas at 0·02 μm per hour per per cent silane and, of course, deposits both on the substrate and on the target. When this deposition rate exceeds the sputtering rate the film obtained appears to be only undoped silicon, independent of the nature of the target. This is evidenced by the films obtained showing typical 'intrinsic' activation energies and by the fact that the target itself is found to be covered with an amorphous silicon film. With typical sputtering rates in the range 0·2–0·3 μm/hour and an input power of 250 W to a 3 in. target, the maximum permissible silane proportion is in the range 10–15% of the total gas admitted in order for the target to contribute to the deposited film.

§ 3. Infra-red spectra

Absorption peaks characteristic of hydrogen bonded to silicon in the amorphous material have been studied by, amongst others, Brodsky *et al.* (1977), Knights (1976) and Tsai and Fritzsche (1979) and table 1 gives the frequencies of the various types of bond given in these papers.

In films produced by glow discharge the predominant form for the hydrogen is ≡Si–H with the principal absorption peak at 2000 cm^{-1}. For films sputtered in argon–hydrogen and argon–silane mixtures the principal peak is at 2100 cm^{-1}, indicating that the hydrogen is mainly incorporated in the two-bond $=Si-H_2$ form. Tsai and Fritzsche (1979), following a suggestion by Knights (1976), deduced that the SiH_2 is in fact often in the form of polysilane chain molecules and that these give rise to a doublet absorption at 850 and 900 cm^{-1}. In films prepared by sputtering in silane this doublet is invariably present for substrate temperatures up to 375°C. After annealing at a temperature above the deposition temperature in vacuum for several hours the 2100 cm^{-1} peak remains dominant but the doublet may be replaced by a single peak at ~875 cm^{-1}, suggesting that the polysilane has been broken up into separate

Table 1. Frequencies of the infra-red absorption peaks for various silicon–hydrogen bonds.

Bond	Frequency (cm^{-1})	Mode
≡Si–H	2000	stretch
	~640	wag
=Si–H_2	2000	stretch
	875	bend
	~640	wag
(=Si–H_2)$_n$	850, 900 (doublet)	bend
–Si–H_3	~2200	stretch
	500	bend
	~640	wag

SiH_2 groups. The –Si–H_3 bending mode at 500 cm^{-1} is often observed but the stretch mode at 2200 cm^{-1} is generally obscured by the 2100 cm^{-1} peak. Annealing at 275°C usually eliminates the SiH_3 peaks.

The concentration of bonded hydrogen in the film is obtained from the area under the curve of α/ω against ω where α is the absorption coefficient and ω is the reciprocal wavelength in cm^{-1}. Brodsky *et al.* (1977) give oscillator strengths for the various types of bond and the appropriate dielectric constant correction for their polarizabilities. The uncertainties in the latter, however, yield an accuracy only to within a factor of two for the calculated strengths. Using these, the hydrogen concentrations for a typical set of sputtered films is given in table 2. In each case the deposition conditions were: flow rate 40 cm^3 min^{-1} argon, 7½% SiH_4, pressure 3 μm, substrate temperature 250°C. A typical absorption spectrum for a film deposited at a power of 100 W is shown in figs. 1 (*a*) and (*b*).

Table 2. Hydrogen content for films produced at different powers.

Target	R.f. power (W)	≡Si–H ($\times 10^{21}$ cm^{-3})	=Si–H_2 ($\times 10^{21}$ cm^{-3})	Total H ($\times 10^{21}$ cm^{-3})
0·009 Ω cm n-type	250	1·92	1·92	3·84
	180	2	4·09	6·09
	110	0·63	9·7	10·33
0·007 Ω cm p-type	250	1·07	2·14	3·11
	190	1·3	3·39	4·69
	100	0·7	10·1	10·8

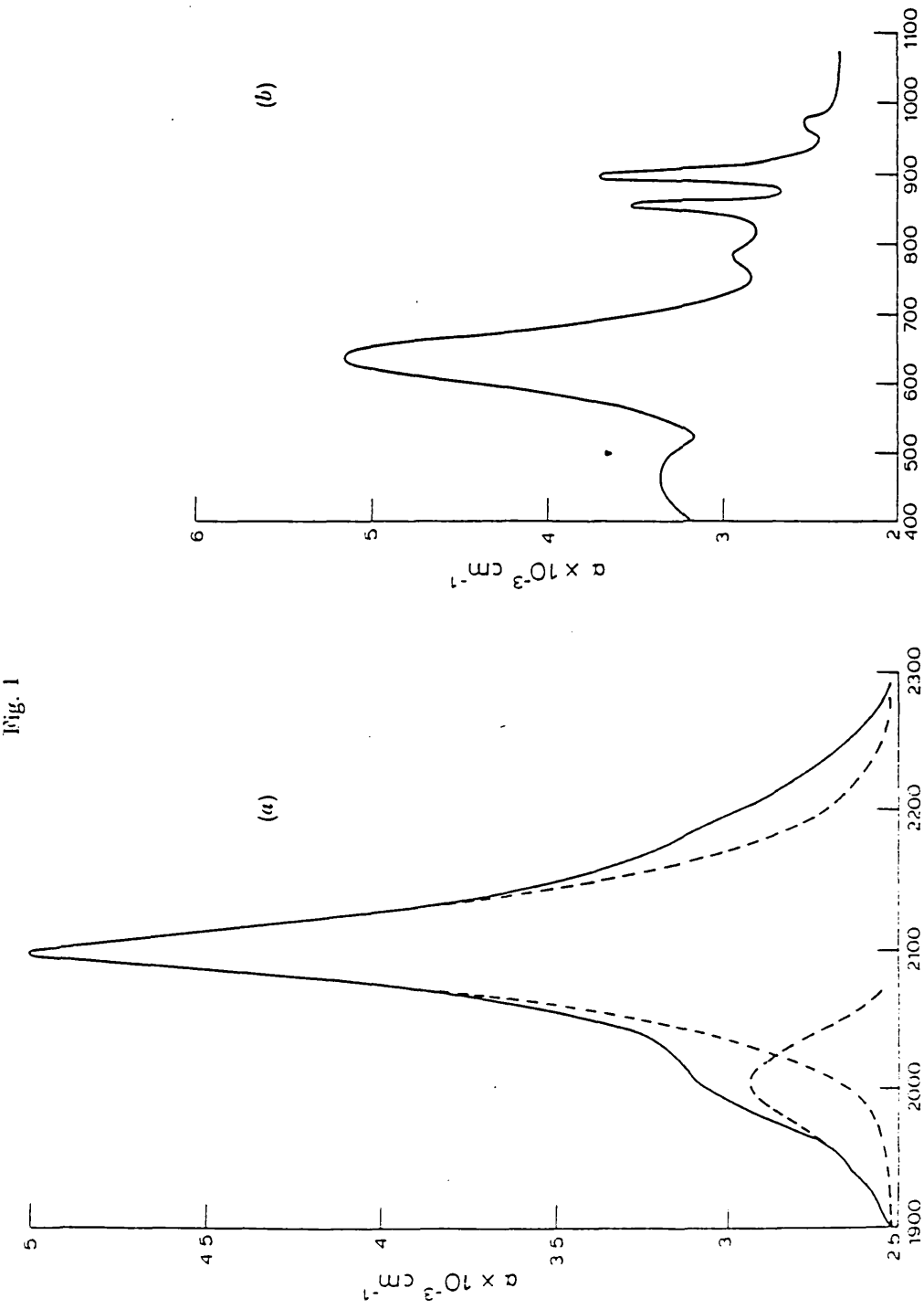

Fig. 1

Infra-red absorption spectra for sputtered films ; (*a*) stretch modes, (*b*) bend and wag modes.

As the sputtering rate decreases the hydrogen content increases, indicating that a larger proportion of the film originates from the silane ; in fact at 100 W the sputtering rate is approximately equal to the deposition rate from the gas and the film composition is virtually independent of the nature of the target. Under these conditions it appears that the polysilane form is strongly favoured in the film.

In the glow-discharge method of film deposition the plasma is produced with powers in the range 10–50 W with gas pressures between 10 and 1000 μm. Low substrate temperatures and higher pressures favour the polysilane groupings. As an approach to these conditions a series of films was prepared in the sputtering system using 50 W r.f. power (below the sputtering threshold for silicon) and 10% SiH_4 with a gas pressure of 10 μm or greater.

Fig. 2

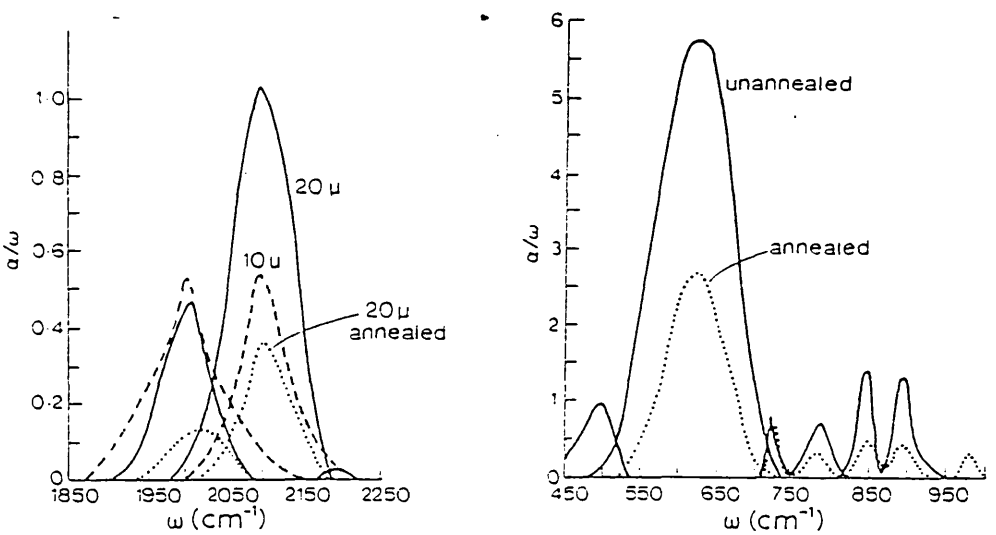

Infra-red absorption spectra for low-power, high-pressure films ; (*a*) stretch modes, (*b*) bend and wag modes.

In figs. 2 (*a*) and (*b*) are shown the spectra, plotted as α/ω against ω, for a film deposited on the earthed counter-electrode (anode) at 10 μm and 20 μm total gas pressure with $T_s = 250$°C. Also shown are the spectra resulting from annealing the 20 μm film at 285°C for 1 hour in a vacuum of 10^{-3} μm. It will be seen that the SiH_2 doublet at 850–900 cm^{-1} is reduced by annealing but remains a doublet. The SiH_3 peaks at 2200 and 500 cm^{-1} disappear after annealing. These results were compared with those obtained using identical conditions and a pressure of 10 μm but with a magnetron target, which considerably reduces electron bombardment of the growing film. No significant differences were found in the resulting spectra, the amount of hydrogen incorporated or its distribution between bonding states.

In figs. 3 (*a*) and (*b*) the spectra for a film deposited on the cathode electrode at $T_s = 25°C$ at a pressure of 10 μm are shown for the as-deposited film (solid line) and after annealing at 285°C for 1 hour (dotted line). The large peak at 975 cm^{-1} in the as-deposited film is not identified but, since it completely disappears on annealing, is assumed to be due to a gaseous silicon–hydrogen molecule. As found by Tsai and Fritzsche (1979), the principal form of bonding appears to be $\equiv$Si–H. The SiH_2 doublet of the anode films is replaced by a singlet at 875 cm^{-1}, indicating that the polysilane form is absent. SiH_3 groups appear to be completely absent.

Fig. 3

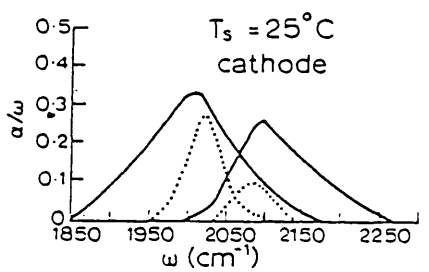

(*a*)

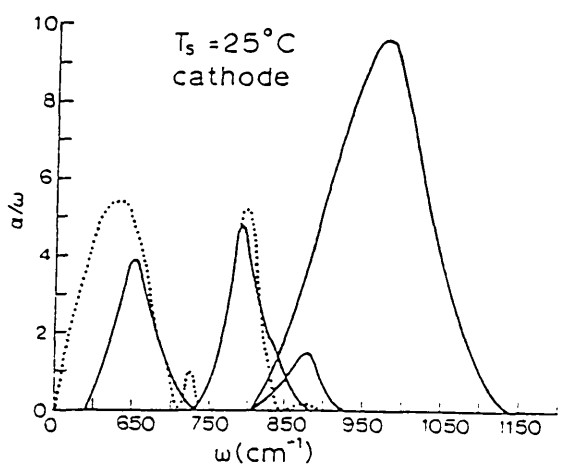

(*b*)

Infra-red absorption spectra for films deposited on cathode electrode ; (*a*) stretch modes, (*b*) bend and wag modes.

In figs. 4 (*a*) and (*b*) are shown the spectra for the case where the power was split equally between target and counter-electrode (30 W in each), with the substrate on the counter-electrode at a temperature of $T_s = 25°C$, with 10 μm gas pressure. It will be seen that the SiH peak at 2000 cm^{-1} still predominates

but that the SiH_2 peak is stronger than in the cathode case. The unidentified peak at 975 cm^{-1} is again present, but much weaker, and disappears on annealing. The SiH_2 bend mode is a singlet at 875 cm^{-1}. An SiH_3 peak is visible for both the stretch mode (2200 cm^{-1}) and the bend mode (500 cm^{-1}) in the as-deposited film and is still present, although reduced, after annealing.

Fig. 4

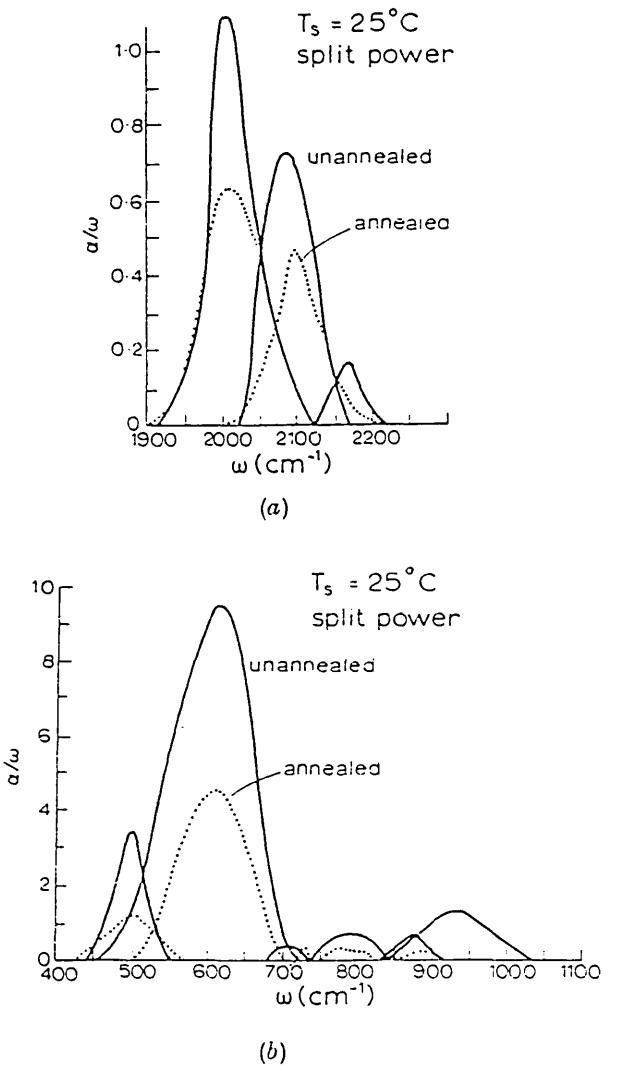

Infra-red absorption spectra for films deposited with split power (see text) ; (*a*) stretch modes, (*b*) bend and wag modes.

§ 4. Oscillator strengths

These results present an opportunity for estimating the oscillator strengths for the bending and wagging modes for the SiH_2 and SiH_3 groups.

Brodsky *et al.* (1977) (hereafter referred to as BCC) point out that the peak at 2100 cm^{-1} arises from both the SiH_2 stretch mode and the symmetric SiH_3 stretch mode whilst the peak at 2200 cm^{-1} corresponds to the asymmetric SiH_3 stretch mode. The films of fig. 2 show both a well-resolved peak at 2200 cm^{-1} and one at 500 cm^{-1}, which we believe to be due to the SiH_3 bend mode. BCC give, for the number of bonds in a stretch mode,

$$N = \frac{(1+2\epsilon_m)^2}{9\epsilon_m^2}\,\epsilon_m^{1/2}\,\frac{N_0}{\Gamma/\zeta}\int\frac{\alpha(\omega)}{\omega}\,d\omega, \tag{1}$$

where ϵ_m is the relative permittivity, N_0 is Avogadro's number, Γ/ζ is the oscillator strength per bond and the integral is the area under the peak. They quote $\Gamma/\zeta = 3{\cdot}5$ cm^2/m mol for the stretch mode in all groups. Applying this to the 2200 cm^{-1} peak of fig. 2 we find the number of SiH_3 bonds to be $7{\cdot}47 \times 10^{21}$ cm^{-3}. Using this with the area of the 500 cm^{-1} peak gives an oscillator strength per group for SiH_3 of 26·8 cm^2/m mol; this compares well with the average figure of 28 cm^2/m mol quoted by BCC for the bending mode. We choose an average figure of 27 cm^2/m mol.

Using the SiH_3 concentration deduced we may determine the concentration of SiH_2 bonds from the area under the 2100 cm^{-1} peak with the SiH_3 contribution subtracted. Using this with the area under the 975–900 cm^{-1} doublet we deduce a figure for the bending-mode oscillator strength per SiH_2 group of 7·08 cm^2/m mol which is close to the figure of 7 cm^2/m mol quoted by BCC.

Using these oscillator strengths, namely SiH = 3·5, $SiH_2 = 7$ and $SiH_3 = 27$ cm^2/m mol, we can obtain the concentration of these groups in our films from the 2000 cm^{-1}, 850–900 cm^{-1} and 500 cm^{-1} peaks respectively. The peak at 640 cm^{-1} is ascribed to the wagging mode of all three groupings. We assume that the total area, A_{640}, under the peak can be represented as the sum of the areas due to the three modes separately. Thus

$$A_{640} = \Gamma_1^{w}\frac{N_1}{B} + \Gamma_2^{w}\frac{N_2}{B} + \Gamma_3^{w}\frac{N_3}{B}, \tag{2}$$

where B is a constant given by

$$B = \frac{9\epsilon_m^{3/2}N_0}{(1+2\epsilon_m)},$$

and Γ_1^{w}, Γ_2^{w}, Γ_3^{w} are the oscillator strengths for SiH, SiH_2 and SiH_3 respectively. Using a linear-regression analysis with eqn. (2) on all the specimens described here we find $\Gamma_1 = 47$, $\Gamma_2 = 56$ and $\Gamma_3 = 198$ cm^2/m mol for the singly, doubly and trebly bonded groups respectively. However, BCC point out that, owing to uncertainty in the scaling of the permittivity to acount for local-field corrections, the estimates for hydrogen-bond concentration are unlikely to be accurate to better than a factor of 2. Thus the absolute figures derived above are subject to the same accuracy. Even allowing for this it would appear from the results that the contribution from each bond in the SiH_2 and SiH_3 groups is not equal to the contribution of a SiH bond alone.

Summarizing the above it is evident that deposition on the cathode favours Si–H bonding over the doubly bonded form. Since in normal sputtering the target is the cathode and deposition onto it from the silane is re-sputtered in the

direction of the substrate, it might be expected that there will be some increase in the ≡Si–H content of the films as the sputtering rate increases above threshold, as shown in the results of table 2.

§ 5. Electrical properties

The standard measurement adopted was of conductivity as a function of temperature in order to obtain the activation energy for conduction. Contacts used were Cr or 95% Au–5% Sb alloy for n-type films and Al for p-type films. Spear and Le Comber (1976) obtained doped films by glow-discharge deposition from mixtures of phosphine and silane for n-type and borane and silane for p-type. From their results the density of electrically active donors or acceptors can be obtained approximately from the measured activation energy. However, they found that 'intrinsic', undoped silicon films prepared in a glow discharge by their standard method with a substrate temperature of ~250°C gave defect-controlled conductivity with activation energies in the range 0·6–0·7 eV. In the present work, pure silicon films have been found to give activation energies in the range 0·7–0·8 eV. In table 3 we give the electrical results for the films of table 2.

Table 3. Electrical conduction parameters and deposition rates for films prepared with different powers.

Target	Power (W)	Total rate (μm/hour)	Sputter rate (μm/hour)	E_A (eV)	σ_D $(\Omega\ \mathrm{cm})^{-1}$	Approximate impurity/silicon ratio
n^+	250	0·54	0·4	0·61	6×10^{-8}	7×10^{-6}
	180	0·37	0·23	0·8	4×10^{-8}	$5·8\times10^{-6}$
	110	0·25	0·11	0·75	3×10^{-8}	$4·1\times10^{-6}$
p^+	250	0·62	0·48	0·55	1×10^{-6}	$2·8\times10^{-5}$
	190	0·56	0·42	0·7	1×10^{-8}	$2·3\times10^{-5}$
	100	0·36	0·22	0·7	5×10^{-7}	$2·17\times10^{-5}$

Only the 250 W specimens exhibit extrinsic conductivity. Confirmation that the density of states at the Fermi level was similar to that reported by Spear and Le Comber (1976) was obtained using the analysis proposed by Solomon, Dietl and Kaplan (1978). They account for the change in the dark activation energy for conduction, which is observed after the sample has been illuminated for a long period, in terms of surface band bending. This effect was also observed in our films and, using their model, we obtained a figure of $6\times10^{17}\ \mathrm{cm}^{-3}$ for the density of states at the Fermi level. Thus we would expect that a given density of electrically active impurities in our films would produce a similar activation energy and conductivity to those obtained by Spear and Le Comber (1976) for their glow-discharge films. Using Spear and Le Comber's results $E_A = 0·61$ eV for an n-type specimen corresponds to a ratio of active donors to silicon atoms of 3×10^{-7}. On this basis only 1 in 23 of the sputtered phosphorus atoms from the n^+ target are electrically active in the

film. For the p^+ film Spear and Le Comber's results show an initial compensation occurring as the p-type dopant is introduced so that converting from an activation energy to a dopant concentration is uncertain for lower dopant concentrations. To investigate this point further, films were prepared using a pure boron target with varying silane concentrations. At 5% silane, $T_s = 250°C$, pressure $= 0{\cdot}4\ \mu m$, a film containing 23% boron was obtained with an activation energy of 0·53 eV. This is virtually a Si–B alloy so that comparison with a doped film is questionable, but if it is assumed that some of the boron enters the silicon lattice substitutionally then, from Spear and Le Comber's results, the doping fraction would be 2×10^{-5}.

The general conclusion from this work is that, when the dopant is incorporated by sputtering from a doped target, it is mostly able to satisfy its valency in the deposited film and, as a result, is in the main not an electrically active substitutional dopant.

§ 6. Intrinsic films

Activation energies for the low-power, high-pressure films described earlier were found to lie in the range 0·73 to 0·86 eV. There was no correlation between these conductivities or activation energies and the amount of hydrogen incorporated or the form of bonding of the hydrogen. Whilst intuitively it would seem that singly bonded ≡Si–H should give the best electrical behaviour no evidence has yet been found to support such a view.

§ 7. Conclusions

Substitutional doping of α-silicon films by sputter-deposition from doped targets in the presence of silane is inefficient over the normal range of sputtering conditions. There is no evidence that this is associated with the predominance of the $=Si–H_2$ bonded form of hydrogen in the films. Since doping from the gaseous hydrides has been shown to be effective in both sputtering (Paul, Lewis, Connell and Moustakas 1976) and glow discharge (Spear and Le Comber 1976) depositions, it may be the case that the dopant atom must carry an H atom with it into the film in order to achieve an electrically active substitutional site.

Acknowledgments

It is a pleasure to acknowledge the valuable assistance of R. Chater of the Analytical Services Laboratory of Imperial College, who carried out the infra-red spectroscopy.

The support of a N.A.T.O. research grant is gratefully acknowlediged.

References

Brodsky, M. H., Cardona, M., and Cuomo, J. J., 1977, *Phys. Rev.* B, **16**, 3556.
Freeman, E. C., and Paul, W., 1978, *Phys. Rev.* B, **18**, 4288.
Knights, J. C., 1976, *Phil. Mag.*, **34**, 663.
Paul, W., Lewis, A. J., Connell, G. A. N., and Moustakas, T. D., 1976, *Solid St. Commun.*, **20**, 969.
Solomon, I., Dietl, T., and Kaplan, D., 1978, *J. Phys., Paris*, **39**, 1241.
Spear, W. E., 1977, *Adv. Phys.*, **26**, 312.
Spear, W. E., and Le Comber, P. G., 1976, *Phil. Mag.*, **33**, 935.
Tsai, C. C., and Fritzsche, H., 1979, *Sol. Energy Mater.*, **1**, 29.

APPENDIX 2

(a) "Hard Centres" (very localised centres)

The energy spacing ΔE between quantum levels to a characteristic spatial extent, λ, of the electronic wavefunction is given by $\Delta E \simeq (2/\lambda)^2$, where ΔE is in eV and λ is in Å. Because of the small extension of the wavefunction ($\lambda \simeq 2$Å) the level can accommodate only one electron and is a paramagnetic centre. The addition of another electron makes a bonding or antibonding level outside the gap (see fig.7·4 in ref.) because the Hubbard-type repulsion U is very large.

(b) "Soft Centres" (Electrons with a wavefunction spread on several atomic sites)

Each level can accommodate 0, 1 or 2 electrons because the Hubbard correlation energy U between the two electrons is small ($|U| < kT$). The states above the Fermi level, E_F, are empty, and the states below the Fermi level are populated by 2 electrons of opposite spin and are not magnetic, except for a very small region of about kT around E_F (see Fig. 7·5 in ref.).

(After I. Solomon, ref. 15 in Ch. 2)

APPENDIX 3

```
 1 DIML(70),TC(70),GC(70),T(70),R(70),RC(70),E(70),A(70)
 2 OPEN1,4
 5 PRINT"■"
 20 DATA.38,.382,.384,.386,.388,.39,.392,.394,.396,.398,.4,.405,.41,.415,.42,.42
5
 30 DATA.43,.435,.44,.445,.45,.455,.46,.465,.47,.475,.48,.485,.49,.495,.5
 40 DATA.51,.52,.53,.54,.55,.56,.57,.58,.59,.6,.62,.64,.66,.68,.7,.72,.74,.76,.7
8
 50 DATA.8,.82,.84,.86,.88,.9,.92,.94,.96,.98,1,1.025,1.05,1.075,1.1,1.125,1.15
 200 FORI=1TO67:TC(I)=1:NEXT
 290 FORI=1TO67:READL(I):NEXT
 293 FORI=1TO67:GC(I)=0:NEXT
 300 INPUT"FILM THICKNESS (MICRONS)";D
 390 I=1
 410 PRINT"LAMBDA("I")="L(I)
 415 GETA$:IFA$=""THEN415
 416 IFA$="U"THENI=I+1:PRINT:GOTO410
 417 IFA$="D"THENI=I-1:PRINT:GOTO410
 418 IFA$="P"THEN500
 420 PRINT"R("I")=0.085":R(I)=0.085
 430 PRINT"T("I")=":INPUT"■■■■■■■■";T(I)
 435 PRINT:PRINT:I=I+1
 440 GOTO410
 500 INPUT"■INDEX OF ALPHA";N1
 502 FORI=1TO68
 510 IFR(I)=0THEN560
 515 RC(I)=R(I)*TC(I)-GC(I)
 520 E(I)=1.239854/L(I)
 530 C=T(I)/(1-RC(I))/(1-RC(I))
 535 B=LOG((1+SQR(1+4*C*C*RC(I)*RC(I)))/2/C)
 536 A(I)=B/D
 540 A(I)=(A(I)/2/D*1E4)
 560 NEXTI
 590 PRINT
 595 PRINT#1,"":PRINT#1,""
 600 PRINT"E(EV)  ALPHA("N1") (AHF)↑"N1
 605 PRINT#1,"E(EV)          ALPHA("N1")          (AHF)"N1
 610 PRINT"_____ _____"
 615 PRINT#1,"-----          ----------          --------"
 620 FORI=1TO68
 625 IFR(I)=0THEN640
 627 Z=1.2399
 628 IFA(I)<0THENA(I)=-A(I):A=-1
 630 IFA=>0THENPRINTINT(E(I)*1E4)/1E4,INT(A(I)↑N1),INT((A(I)*Z/L(I))↑N1*100)/100
 632 IFA<0THENPRINTINT(E(I)*1E4)/1E4,INT(A(I)↑N1),INT((A(I)*Z/L(I))↑N1*10)/10" -
"
 635 IFA=>0THENPRINT#1,INT(E(I)*1E4)/1E4,INT(A(I)↑N1),INT((A(I)*Z/L(I))↑N1*10)/1
0
 637 IFA<0THENPRINT#1,INT(E(I)*1E4)/1E4,INT(A(I)↑N1),INT((A(I)*Z/L(I))↑N1*10)/10
" -"
 639 A=0
 640 NEXTI
 650 GETA$:IFA$=""THEN650
 660 IFA$="N"THENCLR:GOTO1
```

```
670 IFA$="P"THEN500
680 IFA$="E"THEN300
690 IFA$="D"THEN1000
695 IFA$="Z"THEN2000
700 END
1000 PRINT"FILM THICKNESS (MICRONS)"D
1001 PRINT#1,"FILM THICKNESS (MICRONS)"D
1002 PRINT"LAMBDA(MICRONS)     R        T"
1003 PRINT#1,  "LAMBDA(MICRONS)     R        T"
1005 PRINT"---------------     -        -
1006 PRINT#1,"---------------     -        -
1010 FORI=1TO145
1015 IFR(I)=0THEN1040
1020 PRINTL(I),R(I),T(I)
1030 PRINT#1,L(I),R(I),T(I)
1040 NEXTI
1050 GOTO500
2000 REM** WRITING DATA TO DISK**
2010 PRINT"DATA FILE NAMES";:INPUT FW$
2020 PRINT"DRIVE NO.";:INPUT DW$
2030 PRINT"WRITING DATA TO DISK"
2040 PRINT"FILENAME";FW$"DRIVE NO.";DW$
2044 GS=0
2045 FOR J=1 TO70
2046 IFE(J)<>0 THENGS=GS+1
2049 NEXT
2050 OPEN2,8,2,DW$+":"+FW$+",S,W"
2060 E=GS:PRINTE:PRINT#2,E;CHR$(13);
2065 PRINT" I GOT HERE"
2070 FORL=1 TO 70
2075 IFE(L)=0THEN2100
2080 E=E(L):PRINT#2,E;CHR$(13);
2090 E=A(L):PRINT#2,E;CHR$(13);
2100 NEXTL
2110 CLOSE2
```

REFERENCES

Chapter 1

1. W.E. Spear, P.G. LeComber, Solid State Commun., 17, p.1193 (1975).
2. B. Abeles, G.D. Cody, Y. Goldstein, T. Tiedje and C.R. Wronski, Thin Solid Films, 90, (4), p.441 (1982).
3. D.E. Carlson, IEEE Transaction on Electron Devices, vol. ED-24, (4), p.449 (1977).
4. J. Mort, S. Grammatica, J.C. Knights and R. Lujan, Solar Cells, 2, p.451 (1980).
5. Y. Nakayama, T. Natsuhara, N. Nagasawa and T. Kawamura, Japan J. Appl. Phys. 21, p.4604 (1982).
6. W.E. Spear, P.G. LeComber, A.J. Snell and R.A. Gibson, Thin Solid Films, 90,(4), p.359 (1982).
7. T. Baji, Y. Shimomoto, H. Matsumura, N. Koika, T. Akiyama, A. Sasano and T. Tsukada, Japan J. Appl. Phys., 21, Suppl. 21-1, p.269 (1981).
8. Y. Hamakawa (editor), Amorphous Semiconductor Technology and Devices (Japan 1982), OHM North Holland, Amsterdam, NL, 1981.
9. P.W. Anderson, Phys. Rev., 109, p.1492 (1958).
10. R.C. Chittick, J.H. Alexander and H.F. Sterling, J. Electrochem. Soc. 116, p.77 (1969).
11. P.G. LeComber, A. Madan and W.E. Spear, J. Non-Cryst. Solids, 11, p.219 (1972).
12. W.E. Spear, Adv. Phys. 23, p.811 (1977).
13. J.C. Knights, Phil. Mag. 34, p.663 (1976).
14. J.C.Anderson, Ki-Wan Kim and E. Seferiades, Phil. Mag. B, 43 (1), p.51 (1980).

15. D.A. Anderson and W. Paul, Phil. Mag. B. 44 (2), pp. 187-213 (1981).

16. D.A. Anderson and W. Paul, Phil. Mag. B., 45 (1), pp. 1-23 (1982).

17. D.A. Anderson, T.D. Moustakas and W. Paul, p.334. W.E. Spear (ed.), Proc. 7th International Conference on Amorphous and Liquid Semiconductors (CICL, Univ. of Edinburgh, 1977

18. T.D. Moustakas and W. Paul, Phys. Rev. B., 16, p.1564 (1977).

19. F.B. Ellis and R.C. Gordon, J. Appl. Phys.,p.5381 (1983).

20. J. Karicki, C.M. Ransom, W. Bauhofer, T.I. Chappell and B.A. Scott, J. Non-Cryst. Solids 66,pp.51-58 (1984).

21. G. Sasaki, S. Fujita and A. Sasaki, J. Appl. Phys. 53 (2), p.1013 (1982).

22. J. Magarino, D. Kaplan and A. Friederich, Phil. Mag. B, 45 (3), p.51 (1982).

23. R.F. Bunshah, U.S. Patent No. 3791852.

24. J.C. Anderson, U.K. Patent No. 8325495.

25. J.C. Anderson and S. Biswas, 5th International Conference, Ion and Plasma Assisted Techniques, Munich, May 1985.

REFERENCES

Chapter 2

1. N.F. Mott and E.A. Davis, p.15, Electronic Process in Non-Crystalline Materials, 2nd edition, Clarendon Press, Oxford (1979).
2. P.W. Anderson, Phys. Rev. 109, p.1492 (1958).
3. N.F. Mott, Phil. Mag., 22, p.7 (1970).
4. A. Madan, P.G. LeComber, W.E. Spear, J. Non-Cryst. Solids, 8-10,pp.727-738 (1976).
5. W.E. Spear, P.G. LeComber and A.J. Snell, Phil. Mag. B., 38, pp. 303-317 (1978).
6. M.H. Cohen, H. Fritzsche and S.R. Ovshinsky, Phys. Rev. Lett. 22, p.1065 (1969).
7. N.F. Mott, E.A. Davis and R.A. Street, Phil. Mag. B. 32, p.961 (1975).
8. N.F. Mott and E.A. Davis, p.219 in Ref. 1.
9. C.Tsang and R.A. Street, Phys. Rev.B. 19, p.3027 (1979).
10. W. Beyer, H. Mell and H. Overhof, p.328, W.E. Spear (ed.), Proc. 7th International Conference on Amorphous and Liquid Semiconductors. (CICL, Univ. of Edinburgh, 1977).
11. D.I. Jones, P.G. LeComber and W.E. Spear, Phil. Mag.B. 36, p.541 (1977).
12. W.E. Spear, Al-Ani Haifa and P.G. LeComber, Phil. Mag. B. 43 (5), p.781 (1981).
13. R.W. Griffith, J. Non-Cryst. Solids 24, p.413 (1977).
14. D.A. Anderson, W. Paul, Phil. Mag. B. 45 (1), pp. 1-23 (1982).

15. P. Nagels, Amorphous Semiconductors, ed. M.H. Brodsky (1979).

16. N.F. Mott, Chelsea Conference, 1984.

17. P.G. LeComber, D. Jones and W.E. Spear, Phil. Mag. B. 35, p.1173 (1977).

18. W.E. Spear and P.G. LeComber, J. Non-Cryst. Solids, 8-10, p.727 (1972).

19. W.E. Spear and D.S. Tannhauser, Phys. Rev. B. 7, p.831 (1973).

20. M.H. Brodsky, M. Cardona and J.J. Cuomo, Phys. Rev. B. 16, p.3556 (1977).

21. W. Shockley and W.T. Read, Phys. Rev., 87, p.835, 1952.

22. G.W. Taylor and J.G. Simmons, J. Non-Cryst. Solids, 8-10, pp.940-946 (1972).

23. J.G. Simmons, G.W. Taylor, J. Non-Cryst. Solids, 8-10, pp. 947-953 (1972).

24. J.G. Simmons, G.W. Taylor, J.Phys. C., Solid State Phys.6, p.3706 (1973).

25. W.E. Spear, Garmisch, p.1, 1974.

26. D.Carles, C. Vautier and C. Viger, Thin Solid Films 17, p.67 (1973).

27. A. Rose, Concepts in Photoconductivity and Allied Problems, Interscience, New York, 1963.

28. P.E. Vanier, A.E. Delahoy and R.W. Griffith, J. Appl. Phys. 52 (8), p.5235 (August 1981).

29. P.E. Vanier, R.W. Griffith, J. Appl. Phys. 53 (4), p.3099 (1982).

30. J.P.V. Drazin, Ph.D. Thesis, London, 1984.

REFERENCES

Chapter 3

1. D.G. Terr, J.Adhesion 8, p.289 (1977).
2. C. Weissmantel, K. Bewilogna, K Brever, D. Dietrich U. Ebersbach, H-J. Erler, R. Rau and G. Reisse, Thin Solid Films, 96, 31 (1982).
3. B. Lewis and J C. Anderson, Nucleation and Grwoth of Thin Films, New York, London, Academic Press, 1978.

REFERENCES

Chapter 4

1. R.A. Street and N.F. Mott, Phys. Rev. Lett. 39, p.1293 (1975).
2. M.H. Brodsky, R.S. Title, Phys. Rev. Lett. 23, p.581 (1969).
3. M.H. Brodsky, D. Kaplan, J. Non-Cryst. Solids 32, pp. 431-435 (1979).
4. W.E. Spear, P.G. LeComber, J. Non-Cryst. solids, 8-10, p.727 (1972).
5. W. Paul, A.J. Lewis, G.A.N. Connell and T.D. Moustakas, Solid State Commun. 20, p.969 (1976).
6. M.H. Brodsky, M. Cardona and J.J. Cuomo, Phys. Rev.B. 16 (8) (1977).
7. K. Zallama, P. Germain and S. Squelard, Phys. Rev.B. 23 (12), p.6648 (1981).
8. T.D. Moustakas, D.A. Anderson and W. Paul, Solid State Commun. 23, pp. 155-158 (1977).
9. P.G. LeComber, W.E. Spear, Topics in Applied Physics, Amorphous Semiconductors, ed. M.H. Brodsky, 1979.
10. (a) M. Cardona, Internal report, Max Planck Institut für Festkorperforschung, Stuttgart (1983).
11. (b) J.C. Knights, R.A. Street and G. Lucovksy, J. Non-Cryst. Solids, 35-36, p. 279 (1980).
12. (c) G. Lucovsky and W.B. Pollard, J. Vac. Sci. Tech., vol. A1 (2), p.313 (1983).
13. H. Shanks, C.J. Faing, L. Ley, M. Cardona, F.J. Demond and S. Kalbitzer, Phys. Stat. Solid (B), 100, p.43 (1980).
14. W. Paul, Solid State Commun. 34, p.283 (1980).

15. J. Tardy and R. Meandre, Phil. Mag.B. 49, p.73 (1984).

16. M.A. Paesler, D.A. Anderson, E.C. Freeman, G. Moddel and W. Paul, Phys. Rev. Lett. 41 (21), p.1492 (1978).

17. D.A. Anderson, T.D. Moustakas and W. Paul, Proc. 7th International Conference on Amorphous and Liquid Semiconductors, Edinburgh, 1977, p.334.

18. L. Ley, ch. 3, Hydrogenated Amorphous Silicon II, ed. J.D. Joannopoulos and G. Lucovsky, Springer-Verlag, 1984.

19. S. Luby, Thin Solid Films 8, p.333 (1971).

20. G.W. Anderson, J.E. Davey, J. Comas, N.S. Saks and W.H. Kucke, J. Appl. Phys. 45, p.4528 (1974).

21. D.E. Carlson, R.W. Smith, C.W. Magee and P.J. Zanzucchi, Phil. Mag. B. 45 (1), pp.51-68 (1982).

22. R.A. Street, D.K. Biegelsen, Solid State Commun. 33, p.1159 (1980).

23. T.S. Moss, Optical Properties of Semiconductors, Pub. Butterworths, 1961.

24. T. Travelos, Ph.D. Thesis, London, 1984.

25. E.A. Davis and N.F. Mott, Phil. Mag. 22 (1970).

26. C.C. Tsai, H. Fritzsche, Sol. Energy Mat. 1, p.11 (1979).

27. A. Matsuda, M. Matsumura, K. Nakagawa, T. Imura, H. Yamamoto, S. Yamasaki, H. Okushi, S. Iizima and K. Tanaka, Tetrahedrally Bonded Amorphous Semiconductors, ed. by R.A. Street, D.K. Biegelsen, J.C. Knights (Am. Inst. Phys., New York, 1981), p.192.

28. C.C. Tsai, H. Fritzsche, M.H. Tanielian, P.J. Gaczi, P.D. Persans and M.A. Vesaghi, see ref. 17, p.339.

29. N.F. Mott, E.A. Davis, p.205, Electronic Processes in Non-Crystalline Materials, second edition, Clarendon Press, Oxford, 1979.

30. S.C. Moss and J.F. Graczyk, Phys. Rev. Lett. 23, p.1167 (1969).

REFERENCES

Chapter 5

1. J.P.V. Drazin, Ph.D. Thesis, London (1984).
2. P. Nagles, Electronic Transport in Amorphous Semiconductors Chapter 5, in Book [107], ed. by Brodsky.
3. N.F. Mott, E.A. Davis, p.216, Electronic Process in Non-Crystalline Materials, 2nd edition, Clarendon Press, Oxford (1979).
4. W.E. Spear - Private communications.
5. T.D. Moustakas, D.A. Anderson and W. Paul, Solid State commun. 23, 155-158 (1977).
6. D.A. Anderson, T.D.Moustakas and W. Paul, p.334, W.E. Spear (ed.), Proceedings, 7th International Conference on Amorphous and Liquid Semiconductors (CICL, University of Edinburgh, 1977).
7. J.P.V. Drazin, Ph.D. Thesis, London, p.139 (1984).
8. I. Sakata, M. Yamanaka, Y. Mori and Y. Hayashi, Solar Energy Materials 10, pp. 121-138 (1984).
9. D.A. Anderson, W. Paul, Phil. Mag.B., vol. 44, no. 2, pp.187-213 (1981).
10. D.L. Staebler and C.R. Wronski, Appl. Phys. Lett. 31, p.292 (1977).
11. D.L. Staebler and C.R. Wronski, J. Appl. Phys. 51, p.3262 (1980).
12. I. Solomon, T. Dietl and D. Kaplan, J. de Phys. 39, p.1241 (1978).
13. M.J. Powell, B.C. Easton and D.H. Nicholls, J. Appl. Phys. 53, p.5068 (1982).

14. D.V. Lang, J.D. Cohen, J.P. Harbison and A.M. Sergant, Appl. Phys. Lett. 40, p.474 (1982).

15. P.E. Vanier, Appl. Phys. Lett. 41, p.986 (1982).

16. P. Irsigler, D. Wagner and D.J. Dunston, J. Non-Cryst. Solids 69, pp.207-211 (1985).

17. D.L. Staebler, C.R. Wronski, J. Appl. Phys. 51, p.3262 (1980).

18. M.H. Brodsky, M.A. Frisch, J.F. Ziegler and W.A. Lanford, Appl. Phys. Lett.30, p.561 (1977).

19. J.I. Pankove, D.E. Carlson, Appl. Phys. Lett. 31, p.450 (1977).

20. P. Zanzucchi, C.R. Wronski and D.E. Carlson, J. Appl. Phys. 48, p.5227 (1977).

21. W.E. Spear, P.G. LeComber, Phil. Mag.B. 33, p.935 (1976).

22. H. Steemers, W.E. Spear and P.G. LeComber, Phil. Mag.B. 47, p.683 (1983).

23. P.G. LeComber, W.E. Spear, Ch.9, see ref. 2.

24. D.A.Anderson, W.Paul
Phil. Mag.B. 45, pp.1-23 (1982).

25. J.C.Anderson, Ki-Wan Kim, E. Seferiades, Phil. Mag.B. 43, pp.51-60 (1980).

26. N. Mott, p.169, The Physics of Hydrogenated Amorphous Silicon II, Electronic and Vibrational Properties, ed. J.D. Joannopoulos and G. Lucovsky (1984).

REFERENCES

Chapter 6

1. M.A. Paesler, D.A. Anderson, E.C. Freeman, G. Moddel and W. Paul, Phys. Rev. Lett. 41 (21), p.1492 (1978).
2. C.C. Tsai, H. Fritzsche, M.H. Taanielian, P.J. Gaczi, P.D. Persans and M.A. Vesaghi, Proc. 7th International Conference Amorphous and Liquid Semiconductors, Edinburgh 1977, ed. W.E. Spear (Univ. of Edinburgh 1977), p.339.
3. J.C. Anderson, Ki-Wan Kim and E. Seferiades, Phil. Mag.B. 43 (1), pp.51-60 (1980).
4. D.A. Anderson, W. Paul, Phil. Mag.B. 45 (1), pp.1-23 (1982).
5. Z.S. Jan, R.H. Bube and J.C. Knights, J. Electronic Materials 8 (1), pp.47-56 (1979).